2020

Cluster phase space and variational subspace approaches to the quantum many-body problem

BOSTON UNIVERSITY

GRADUATE SCHOOL OF ARTS AND SCIENCES

Dissertation

CLUSTER PHASE SPACE AND VARIATIONAL SUBSPACE APPROACHES TO THE QUANTUM MANY-BODY PROBLEM

by

JONATHAN WURTZ

B.S., University of New Hampshire, 2014

Submitted in partial fulfillment of the

requirements for the degree of

Doctor of Philosophy

2020

Approved by

First Reader

Anatoli Polkovnikov, PhD
Professor of Physics

Second Reader

Chris R. Laumann, PhD
Assistant Professor of Physics

Third Reader

A. Liam Fitzpatrick, PhD
Assistant Professor of Physics

Do you guys just put the word "quantum" in front of everything?
. -Scott Lang (aka the Ant Man)

Acknowledgments

There are so many people to thank for making this work possible. My mother and father, of course, for raising me into who I am today, as well as my brothers Adam and Noah. My fiancé, Katherine, for being her awesome self around me. Of course, also our rabbit Phred for being the best cord nipper and de-stress device one could have. Also the multitude of undergraduate friends surrounding me: Patrick, Stephine, Tim, Ricky, Mikayla, Logan, and many more, for their support. Academically this work would not be possible without my year's cohort and especially collaborators and coworkers Shainen, Dries, Mohit, Pieter, Tamiro, Adam, Owen, and many more. Financially this work would not be possible without my funding sources from the AFOSR and the NSF, as well as Boston University for paying me as a TA. Procedurally, this work would not be possible without my thesis committee of profs. Polkovnikov, Laumann, Fitzpatrick, Klein, and Sushkov. Intellectually, this work would not be possible without my many excellent teachers and professors including Profs. Meridth, Mattingly, Boucher, Polkovnikov, Pi, Laumann, Chandran, and many more. Finally, I would like to give a particular thanks to my high school physics teacher Adam Edgar, who sparked my initial interest in physics.

With great thanks,

Jonathan Wurtz

CLUSTER PHASE SPACE AND VARIATIONAL SUBSPACE APPROACHES TO THE QUANTUM MANY-BODY PROBLEM

JONATHAN WURTZ

Boston University, Graduate School of Arts and Sciences, 2020

Major Professor: Anatoli Polkovnikov, PhD
Professor of Physics

ABSTRACT

Simulating the nonequilibrium behavior of interacting quantum systems is an important way to understand results of experimental quantum simulators, motivate new materials, and refine new quantum algorithms. However, this is a challenging task due to the exponential difficulty of such systems, which motivates dimensional reduction methods, such as semiclassical limits. This work extends semiclassical phase space methods to spin systems with no clear classical limit with the cluster truncated Wigner approximation (cTWA), and improves on Schrieffer-Wolff low energy effective dynamics with variational adiabatic generators. The cTWA was used to compute nonequilibrium dynamics in spin chains, finding behavior such as signatures of many body localization; rapid thermalization and preservation of fluctuations; effective thermodynamic classical behaviors; and signatures of quantum chaos and butterfly velocities, in 1d spin 1/2 chains. Variational Schrieffer-Wolff methods were used to find efficient non-perturbative dressings for the Hubbard model and find effective quasiparticle dynamics and nonthermal states in quantum chaotic spin chains. These methods are potentially

effective tools to separate essential quantum behavior from classical behavior, and can be used to diagnose quantum thermalization behavior in interacting quantum systems.

Contents

List of Figures

List of Abbreviations

AFM	.....	Antiferromagnetic
AGP	.....	Adiabatic gauge potential
DMRG	.....	Density matrix renormalization group
ETH	.....	Eigenstate thermalization hypothesis
FM	.....	Ferromagnetic
KAM	.....	Kolmogorov–Arnold–Moser
MBL	.....	Many body localization
MFI	.....	Mixed field Ising
MPS	.....	Matrix product state
OTOC	.....	Out of time order correlator
SB	.....	Schwinger Boson
SW	.....	Schrieffer Wolff
TFI	.....	Transverse field Ising
TSA	.....	Truncated spectrum approximation
TWA	.....	Truncated Wigner approximation
VLDE	.....	Velocity-dependent Lyapanov exponent
cTWA	.....	cluster truncated Wigner approximation
rTSA	.....	rotated truncated spectrum approximation
rcTWA	.....	rotated cluster truncated Wigner approximation

Chapter 1

Introduction

How is the microscopic quantum world connected to the macroscopic classical world? How does nonlinear classical mechanics and irreversible thermodynamics emerge from the laws of linear, reversible quantum mechanics? Can we use the small-scale behavior of quantum systems to our advantage in the macroscopic world to make new materials, systems, and algorithms? And can we construct efficient models of hard quantum systems to discover and motivate such new ideas? These are big questions which no one person can hope to answer.

This dissertation and the years of work therein represents a small push towards answering these and similar questions. This work has resulted in four papers on two main themes. The first theme is of **effective classical dynamics** of spin chains by reducing exact quantum dynamics into classical dynamics in a high-dimensional classical phase space. This can be used to probe both short time quantum (coherent) behavior as well as long time classical (thermodynamic) behavior. The second theme is of **projective subspace dynamics**, where instead of evolving an exact (exponentially complicated) wavefunction, one uses a smaller subbasis where only the relevent degrees of freedom are included. This can be used to evolve low-energy dynamics, as well as find quasiparticles and nonthermal states in otherwise strongly-interacting systems.

1.1 Outline of the dissertation

This dissertation is structured as follows. The rest of chapter 1 will detail some of the motivation for the work, some general philosophy, as well as some simple quantum mechanics background primer and notation.

Chapter 2 will go over the cluster truncated Wigner approximation (cTWA), which is one of the main products of this thesis work. It is mostly a reorganization of a previous paper (Wurtz et al., 2018) which was an introduction to the method. However, it has been edited in light of a more updated understanding, and new sections have been added, including a new discussion of general initial conditions, more detailed derivation of correlation functions, and more discussion on discrete initial conditions.

Chapter 3 demonstrates the cTWA on various models. This includes a reorganization of a previous paper (Wurtz and Polkovnikov, 2018) as section 3.2, some examples from (Wurtz et al., 2018), and some interesting results on out of time order correlators and Lyapanov exponents in section 3.4.

Chapter 4 expands the cTWA to more general phase spaces and demonstrates its ability to reproduce dynamics exactly on a particular model. While this generalization has much potential, as of now it is an undeveloped avenue to study.

Chapter 5 introduces and demonstrates the idea of variational Schrieffer-Wolff transformations and adiabatic dressing. This is a mixture of two recent papers (Wurtz et al., 2020) and (Wurtz and Polkovnikov, 2020).

Chapter 6 gives some concluding remarks and discussion for future avenues of study.

1.2 Motivation and background

One of the fundamental difficulties of computing time dynamics of quantum systems is the exponential complexity of such simulations: they scale multiplicitively with system size, eg as $\mathcal{D} \sim e^{\gamma L}$ for system size L and geometric prefactor γ. For example, for qubits (which are the quantum version of a binary bit) the number of variables scales as 2^L.

In opposition, classical systems scale additively with system size: For example, adding an additional particle only requires adding a new position $\vec{x}$ and momentum $\vec{p}$, so that complexity $\mathcal{D} \sim \gamma' L$ for geometric prefactor γ' (eg $2DN$ for N particles in D dimensions).

However, these two scalings run into an incongruence: each classical degree of freedom is (technically and physically) some sort of limiting case of an underlying quantum system. For example, when particles are very far apart so that a position-momentum variance of $\Delta x \Delta p \gg \hbar$, quantum effects are not relevent. Similarly, when a quantum spin S is very large (eg the onsite Hilbert space $\mathcal{D} = 2S$ is large), this is equivalent to taking a a classical limit and behaving as a classical top (Polkovnikov, 2010).

Thus, a central question to chapter 2, 3, and 4 is asked: **can one can find a set of effective degrees of freedom for quantum systems which acts like an effective classical limit?** Where there is a well-defined classical limit, such as large spin or individual particles, the procedure for finding effective degrees of freedom is clear: they are simply the position and momentum, or total angular momentum, of each constituent particle.

For systems without such a well-defined classical limit, the procedure is much less clear. For example, a collection of shortrange-interacting spin 1/2, which is the system most studied in this thesis, does not admit a large spin expansion

$(1/2 \ll \infty)$ and heuristically quantum fluctuations play a large role in dynamics. However, most spin systems are **thermal** (D'Alessio et al., 2016), which means that quenches "out of equilibrium" generally settle to some long-time steady state value where observables don't change and time correlation functions become independent of the time offset. A thermal or weakly out-of-equilibrium system is normally characterized by an extensive number of values: for example, particle and energy density, effective temperatures, and density currents. This would imply that for such thermal systems with exponential complexity, there should exist some effective description of dynamics when the system is close to thermal: the effective degrees of freedom are simply the extensive macroscopic thermal quantities like energy density and particle current.

However, exactly what these thermal degrees of freedom are is not a'priori clear. Of course there may be some obvious degrees of freedom such as local particle or energy density. But, there may be others which are nontrivial sums of local or quasi-local operators. Furthermore, there may be a separation of scales: microscopic quantum behavior, which occurs at short time and length scales, may modify the macroscopic effective classical behavior. A reasonable classical limit should describe the correct macroscopic thermal behavior, which requires a correct simulation of the microscopic quantum behavior, and its effects on the macroscopic degrees of freedom.

One way to hopefully capture most thermal and quantum behavior is to simply include many many degrees of freedom, with the hope that a subset of them forms the macroscopic thermal degrees of freedom as well as the relevant microscopic quantum degrees of freedom. If one expands the number of degrees of freedom, one should hopefully include more of the relevant degrees of freedom and thus approach a classical limit with only a polynomial number of variables. One way

of doing this is the cluster Truncated Wigner approximation, which is introduced in chapter 2, demonstrated in chapter 3, and expanded on in chapter 4.

An alternate way of intelligently choosing degrees of freedom is Schrieffer-Wolff block diagonalization and adiabatic dressing methods, detailed in chapter 5. Here, instead of choosing some set of observables and operators as effective degrees of freedom, one chooses from a small sub-basis of the full Hilbert space to compute effective wave function evolution. Then, the degrees of freedom are that of the wavefunction within this reduced subspace, which might be exponentially large in system size but still exponentially smaller then evolving the exact wave function. This works for a particular subset of initial conditions which have large overlap with the subspace, and is demonstrated for ground state excitation behavior for strongly interacting models, as long as they are "close" to some "non-interacting" limit.

These two methods, the cTWA and adiabatic dressing, are two improved ways to find an effective description of quantum chaotic systems. The hope is that these ideas can be used to verify experiments, characterize materials, and potentially develop new quantum algorithms with thermodynamics in mind.

1.3 Some general philosophy

Before going into the many details about the particular methods and results of this dissertaion work, I would like to take a moment to reflect on the general philosophy and aspects of doing theoretical many-body quantum mechanics. It is often an attractive option to reference popular science viewpoints of quantum mechanics. Quantum is "spooky", "incomprehensible", or "weird", as if there

is some mysterious underlying element which is never fully understood. Terms like "superposition", "entanglement" and "Schrödinger's cat" get tossed around with some air of mystery without being used in proper context. Maybe quantum mechanics is some strange otherworldly thing that our mere mortal minds cannot ever fully comprehend! Such discussion is ultimately unproductive. Instead, I would like to offer up a few of my general mentalities which I believe allow a consistent and grounded study of the subject.

Shut up and calculate

The base rules of quantum mechanics are very simple, and ultimately reduce to linear algebra. Time evolution reduces to taking a bunch of matrix-vector products and carefully resumming; equilibrium thermodynamics reduces to exponentiating matrices; low-energy properties reduces to computing the eigensystem of some matrix; Computing expectation values is just taking vector inner products; and so forth. The hardness comes from dealing with the massive exponential complexity of quantum systems, matching theory to experemental systems, and interpreting results to gain meaningful insight. While the rules are simple, this complexity requires resorting to many approximations, truncations, and sneaky math, a hard enough task without thinking about the meaning of the wavefunction and so forth.

Thermodynamics and typicality

A lot of intuition about many-body quantum systems comes from the Eigenstate Thermalization Hypothesis (ETH) (D'Alessio et al., 2016). In a nutshell, it is a statement of equivalent ensembles for quantum systems. For classical systems, one has several equivalent thermodynamic ensembles. One is the canonical ensemble $\mathcal{P} \sim \exp(-\beta H)$, which has a distribution of states over energy, and another is the micro-canonical ensemble $P \sim \delta(E - H)$ which is sharply peaked at one particular

energy. In the thermodynamic limit, these two ensembles are equivalent. ETH then states the same for quantum systems: a high-energy eigenstate, or a set of eigenstates within some small energy band, has the same expectation values as a quantum canonical ensemble at the same energy. Using this perspective, near thermodynamic equilibrium this means that the particular fine structure of a wave function is not necessarily as important, and one might expect more classical longrange behavior to dominate. This means that strict wavefunction interpretations aren't necessarily the only way to do things, and instead one can use phase space and other semiclassical methods as an effective description of near-equilibrium properties, as is done in this work.

Symmetry and basis agnosticism

Symmetry is one of the deepest aspects of physics, using the general principle that underlying physics should be invariant under particular transformations, say rotation of a coordinate system. With this in mind, any numerics or theory that one writes down should also have these symmetries in mind. If there is some preferential basis when there shouldn't be, for example, that is a hint that one should reinspect the theory. This allows one to more efficiently construct theories, as well as build numerics in more generic ways. For example, never needing to explicitly specify a Z basis means that a code might not have unexpected behavior when trying to change a basis.

Focus on the physical

When constructing theories and looking for results, I always try to ask how it is related to experimental and physical systems: Is the data output measurable in an experiment? How difficult might it be to implement? Because of this, I have mainly focused on two objects: *observable expectation values*, which mea-

sure average values of quantities in a system; if these are extensive (say, total Z magnetization) then fluctuations are not as important. The other object of focus is *time correlation functions*, which measure response of the system to perturbations or out of equilibrium behavior. At low energies, these objects also probe quasiparticle response (Sachdev, 2011), while at finite temperature they probe hydrodynamic response (Landau and Lifshitz, 2013).

The life of a numerical experimentalist

As a final point, I would like to offer a little bit of my mentality when doing numerics. As a programmer, I wish to make efficient, generalized code which is robust and repeatable. However, as a scientist, I wish to spend as much time as possible doing science and getting results, and as little time as possible programming. With these two wishes in opposition, I offer my personal answer. With a well-scoped problem (in my case, creating an implementation of the cluster truncated Wigner method), take some time making a general code with clean and simple APIs. For example, this could be inputting particular wavefunction initial conditions, Hamiltonians, geometries, and so forth, and outputting observable data, for my cTWA phase space methods. Once the base code is tested and robust, never really touch it again: this is now your experimental apparatus or worktable. Instead, one can make auxiliary scripts where you can play with different models, look at different outputs, and generally do science, on the worktable you built. But generally, always try to separate *coding* from *science*.

Similarly, building code in a general sense allows for much more scaling: for example, a calculation which might be tractable on a piece of paper for, say, two sites may be impossible any more. Numeric tools which are agnostic to particular examples allow one to scale to much more difficult problems. For example,

computing variational adiabatic gauge potentials in chapter 5 requires operators with tens of thousands of terms, which is handled in seconds on a desktop but is literally impossible by hand.

1.4 A quantum mechanics primer

Although an understanding of quantum mechanics is necessary to read this thesis, some overarching concepts and notation will be discussed here. For more details on various subjects, I recommend the textbooks (Griffiths, 2005; Sakurai and Napolitano, 2017) as well as the new lecture notes by Polkovnikov.

Linear algebra

At its base, quantum mechanics is a mathematical formalism to predict phenomena. Of course, from this comes the rich phenomenology of quantum physics, but comes from some simple mathematical rules.

Linear algebra forms the basis of the mathematics for the rules of quantum mechanics. Wavefunctions $|\psi\rangle$ (the "state") of a system, are complex vectors in some Hilbert space, which is a vector space. These Hilbert spaces normally come in one of two types. The first type is an infinite dimensional Hilbert space, like that used for Bosons or particles moving around in some volume of space. Here, there is some infinite set of discrete states each describing a particular state of the particle; for example, the first excited state of the harmonic oscillator, or the ground state of a particle trapped in a box. Such systems are not really used in this work.

The other type of Hilbert space is a finite dimensional Hilbert space, which is used for objects like spins or Fermions. Here, the total number of different states is enumerable. For example, a spin 1/2 object (also called a qubit) has two

different states $|\uparrow\rangle$ and $|\downarrow\rangle$ corresponding to pointing up or down in, say, the Z direction. Note that there are many equivalent bases (for example, pointing left or right in the X direction) to choose from. In qubit language $|\uparrow\rangle \Leftrightarrow$ Logical 1, while $|\downarrow\rangle \Leftrightarrow$ Logical 0. Then for two qubits there are $2 \times 2 = 4$ states, for 3 there are $2 \times 2 \times 2 = 8$, for 4 there are 16, and so forth.

This work will extensively use these finite dimensional Hilbert spaces. Note that there is nothing stopping a combination of these two Hilbert spaces; for example, the wavefunction of a spin 1/2 particle in some volume of space will include both a continuous part (its position wavefunction) and discrete part (its spin wavefunction).

There are two common objects: operators, and wavefunctions. for a Hilbert space with finite dimension $\mathcal{D}$, wavefunctions can be represented in some basis $\{|i\rangle\}$ as a vector of $\mathcal{D}$ numbers

$$|\psi\rangle = \sum_i |i\rangle c_i \Leftrightarrow \{c_i\}, \tag{1.1}$$

with the additional normalization condition $\sum_i |c_i|^2 = 1$. Operators $\hat{X}$ act on wavefunctions as to change them; given a particular basis they are simply some $\mathcal{D} \times \mathcal{D}$ matrix

$$|\psi'\rangle = \hat{X}|\psi\rangle \quad \Leftrightarrow \quad c_i' = \sum_j X_{ij} c_j \quad \text{with} \quad X_{ij} = \langle i|\hat{X}|j\rangle. \tag{1.2}$$

This means that the abstract operations of wavefunctions and operators in some Hilbert space is replaced with the concrete linear algebra concept of finite-dimensional matrix multiplications. Thus, all numerical effort boils down to linear algebra concepts such as matrix multiplications, eigensystems, singular value decompositions, and so forth.

Time dynamics

One is generally interested in quench time dynamics of wave functions, observables and correlation functions. A quench corresponds to starting the system in the ground state of some simple system H_0, and then suddenly turning on the Hamiltonian H to see how the wavefunction changes in time. In lieu of constructing a Hamiltonian H_0 and its ground state, one may instead just start from some simple initial wave function $|\psi_0\rangle$, such as a product state between sites.

$$\langle\psi_0|X(t)|\psi\rangle \quad ; \quad \langle\psi|X(t)Y(t')|\psi_0\rangle. \tag{1.3}$$

Left is an *observable expectation value*, while right is a *time correlation function*. $X(t)$ defines the operator X at time t, time-evolved by a Hamiltonian $H(t)$ or equivalently rotated by some unitary $U(t)$

$$X(t) = U^\dagger(t)XU \quad ; \quad U^\dagger = \mathcal{T}\exp\left(i\int_0^t dt' H(t')\right). \tag{1.4}$$

$\mathcal{T}$ denotes a time-ordered exponenential of the Hamiltonian, which is necessary if the Hamiltonian does not commute at different times. In this dissertation, units are chosen such that

$$\hbar = 1.$$

Instead of directly computing a unitary via exponentiation, one may integrate operators in time

$$\partial_t X(t) = i[H(t), X(t)]. \tag{1.5}$$

An alternative to this Heisenberg picture of operator evolution is the Schrödinger picture of state evolution, where

$$i\partial_t|\psi(t)\rangle = H|\psi(t)\rangle \quad \text{with} \quad |\psi(0)\rangle = |\psi_0\rangle \quad ; \quad X(t) = \langle\psi(t)|X|\psi(t)\rangle. \tag{1.6}$$

Thus, instead of evolving the operator (Heisenberg) one can instead evolve the state, which is computationally cheaper ($\mathcal{D}$ vs $\mathcal{D}^2$).

Another application of Schrödinger evolution is time correlation functions, which measure response in the system from an excitation at an earlier time. If this is computed for the ground state, then this measures quasiparticle response (Sachdev, 2011). Given local operators X, Y, the correlation function is written as

$$C_{XY}(t,t') = \langle\psi|X(t)Y(t')|\psi\rangle. \tag{1.7}$$

Such correlation functions can be computed in the Schrödinger picture by evolving two wavefunctions, which can be seen by explicitly writing the unitary rotation and liberal use of parenthesis

$$C_{XY}(t,t') = \Big(\langle\psi|U^\dagger(t)\Big)X\Big(U(t)U^\dagger(t')Y\big(U(t')|\psi\rangle\big)\Big) \tag{1.8}$$

First, evolve $\langle\psi|$ to time t (left parenthesis). then evolve $|\psi\rangle$ to time t', act on it with Y, then evolve from time t' to t. Then, compute the overlap with the bra and kets of the two wavefunctions with the operator X.

Spin 1/2

This work almost exclusively uses systems of spin 1/2 particles with Hilbert space dimension $\mathcal{D} = 2$. The full operator space is defined by the three Pauli matrices plus the identity

$$\sigma_x = \begin{bmatrix} 0 & 1 \\ 1 & 0 \end{bmatrix}, \quad \sigma_y = \begin{bmatrix} 0 & -i \\ i & 0 \end{bmatrix}, \quad \sigma_z = \begin{bmatrix} 1 & 0 \\ 0 & -1 \end{bmatrix}, \quad \mathbb{1} = \begin{bmatrix} 1 & 0 \\ 0 & 1 \end{bmatrix}. \tag{1.9}$$

Note that the alternate representation of spin matrices are normalized by a factor of $2S = \sigma$ for spin 1/2. Because the identity trivially commutes to everything and only adds a phase to dynamics, one may always exclude it. These Pauli matrices obey the $SU(2)$ algebra with a structure function $f_{ijk} = 2\epsilon_{ijk}$, the antisymmetric tensor defining the cross product (eg $\epsilon_{xyz} = 1 = -\epsilon_{yxz}$)

$$[\sigma_i, \sigma_j] = 2i\epsilon_{ijk}\sigma_k. \tag{1.10}$$

The Hilbert space of many spin 1/2 is a tensor product of the Hilbert space of each individual spin 1/2. This has a dimension as 2^L, where L is the total number of spins. These spins can be indexed by basis vectors, normally taken to be σ_z eigenstates

$$\mathcal{D} = \bigotimes_i^L \mathcal{D}^i_{\frac{1}{2}} \quad ; \quad |\psi\rangle = |\uparrow\rangle \otimes |\uparrow\rangle \otimes \cdots \otimes |\downarrow\rangle \in \mathcal{D}. \tag{1.11}$$

$|\uparrow\rangle$ is the $+1$ eigenstate of σ_z and contra for $|\downarrow\rangle$. $|+\rangle$ is the $+1$ eigenstate of σ_x and contra for $|-\rangle$. $|\leftarrow\rangle$ is the $+1$ eigenstate of σ_y and contra for $|\rightarrow\rangle$. Because such tensor product Hilbert spaces are used everywhere in this work, the tensor product symbol will from now on be implicit. For example, the wave function above may be equivalently written as $|\psi\rangle = |\uparrow\uparrow \ldots \downarrow\rangle$. The notation σ^i_α can be read as the αth Pauli operator acting on the ith site in the system (where the total system size is implicit). For example, $\sigma^1_x\sigma^3_x$ acting on 5 sites should formally be written as $\mathbb{1} \otimes \sigma_x \otimes \mathbb{1} \otimes \sigma_x \otimes \mathbb{1} \otimes \mathbb{1}$ which of course is extremely cumbersome. Another convenient shorthand is to write that same operator as `1X1X11`.

Physical and model spin 1/2 Hamiltonians

Hamiltonians are generally simple models written as a sum of a polynomial number of products of Pauli strings, motivated by, for example, cold atom quantum simulators (Bloch et al., 2012). These systems are **local**, in that the terms act on at most only maybe 3 sites. A term such as `1X1111Y` is **longrange** (in that it acts on distant spins) but local, while a term such as `1XXZY11ZY1` is **nonlocal** (in that it acts on many spins). Such local Hamiltonians are written as

$$H = \sum_{i\alpha} B^i_\alpha \sigma^i_\alpha + \sum_{ij\alpha\beta} J^{ij}_{\alpha\beta} \sigma^i_\alpha \sigma^j_\beta + \dots . \tag{1.12}$$

B^i_α denote on-site magnetic fields, while $J^{ij}_{\alpha\beta}$ denote interactions or hopping between the ith and jth site. Elipsis represent 3 and larger body terms, which are more nonlocal and are subleading in strength.

Observables are similarly local and normally shortrange; for example $\mathcal{O} = \sum_i \sigma^i_z$ measuring the total Z magnetization of the system, or $\mathcal{O} = \sigma^2_x$, measuring the X magnetization on the second site of the system.

There are many other aspects of quantum mechanics and this section only covers the very basics of bases, operators, time evolution of quenches, and correlation functions. To say this section is incomplete is a massive understatement: there is much more to say from various types of approximations and ansatz; different kinds of systems, such as electrons; equilibrium and ground state properties; quantum algorithms and much more. As a starter I recommend the textbooks of (Griffiths, 2005; Sachdev, 2011; Shankar, 1994; Sakurai and Napolitano, 2017), which were my introductory textbooks, as well as (Nielsen and Chuang, 2011) which has been a touchstone of my quantum information intuition.

Chapter 2

The cluster truncated Wigner approximation: methods

As discussed in chapter 1, there is a fundamental difference between classical and quantum dynamics. Quantum dynamics is linear and requires a number of degrees of freedom exponential in the system size. Classical dynamics is nonlinear but only requires a number of degrees of freedom polynomial (normally linear) in the system size. However, one may expect that when looking at the large scales and long times of a quantum system, it looks effectively like a classical system: a "classical limit". In this classical limit, only a polynomial number of degrees of freedom are required to accurately simulate dynamics. However, the procedure for finding the classical limit is not necessarily clear: one must capture the relevant degrees of freedom while discarding the irrelevant ones in an intelligent way.

The cluster truncated Wigner approximation (cTWA) is an implementation of this idea. One may systematically expand a phase space by including more and more nonlocal and quantum degrees of freedom, hopefully capturing both macro and microscopic behavior. The specifics of the method are detailed in section 2.1 below, but the general idea will be presented here. Given a quantum system of spins with a reasonably small on-site Hilbert space dimension, one can write a phase space based on all operators local to some set of spins. For example, for 32 spins with 4 clusters of 8 spin 1/2, there are $4 \times (4^8 - 1) = 262,140$

independent operators (excluding the identity) and thus a phase space of the same dimension. Within these 262k variables, hopefully some combination of some subset of them include the most relevant degrees of freedom. This is because these degrees of freedom should be local, and an operator with a span of more then 8 sites is really not so. Thus, by expanding the cluster size one should approach the classical result. This comes with the expense of the phase space being very large – exponential in the cluster size. With some numerical tricks, it is reasonable to compute dynamics for up to size ~ 16 clusters. In fact, with further optimization, any system size amenable to exact dynamics may also be a reasonable cluster size, as after numerical trickery the complexity scales as 2^N instead of 4^N!

2.1 General Overview

The method for the cluster Truncated Wigner approximation (cTWA) is as follows. Suppose a system of interacting spins $\frac{1}{2}$ described by a Hamiltonian of the form

$$H = \sum_{ij} J_{ab}^{ij} \sigma_a^i \sigma_b^j + \sum_j B_a^j \sigma_a^j, \tag{2.1}$$

where $a, b \in x, y, z$ denote the indices of Pauli matrices and i, j denote different spins on the lattice. The couplings J_{ab}^{ij} can be short range, long range, and any lattice dimension, and both J_{ab}^{ij} and B_a^j can generally be time-dependent. It is a simple modification to include higher-spin objects and more nonlocal terms. Most examples in this work are on 1d time-independent chains.

The cTWA has to several steps, as illustrated in Fig. 2·1. The first step is the definition of some phase space coordinate system. This also requires some mapping of quantum operators to functions in phase space: the so-called Weyl symbol.

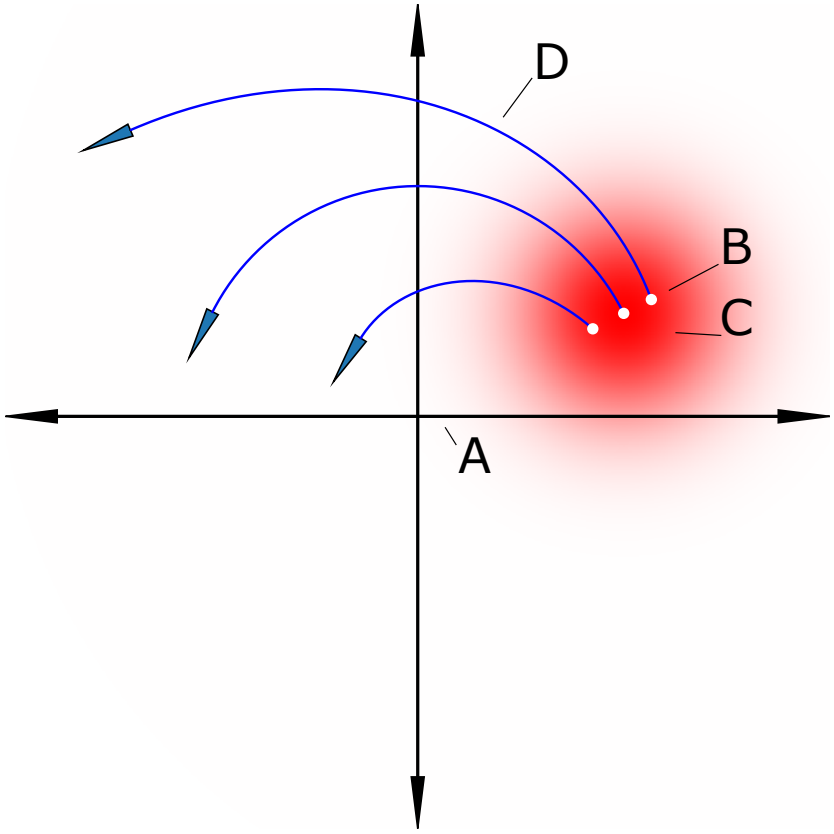

Figure 2·1: Visual example of CTWA evolution in phase space. The coordinate system (A) (Black lines) parameterizes a phase space for points $\{x\}$ and functions $O(\{x\})$ mapped from operators O. Points in phase space (B) (white dots) are selected from a probability distribution (C) (red blob) and evolved independently according to mean field classical equations of motion (D) (blue traces). As evolution is nonlinear, nearby points diverge in time. Observables are found by averaging over all sampled points.

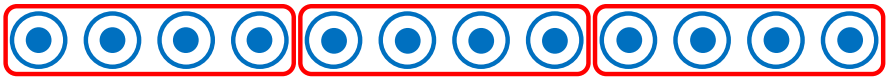

Figure 2·2: Example of clustering of spins. Blue circles are physical spins $\frac{1}{2}$, while red rectangles are the clusters. Hamiltonian dynamics within each cluster is exact, while interactions between clusters are treated approximately.

To this regard, this is done by first finding some set of operators $\{X_\alpha\}$ which are trace orthogonal and form a closed group with structure constants $f_{\alpha\beta\gamma}$

$$\mathrm{Tr}\big[X_\alpha X_\beta\big] = D\delta_{\alpha\beta} \quad , \quad [X_\alpha, X_\beta] = f_{\alpha\beta\gamma} X_\gamma. \tag{2.2}$$

One such example of a closed group is the set of all Pauli matrices on each spin site, eg $\{\sigma_x^0, \sigma_y^0, \sigma_z^0, \sigma_x^1, \sigma_y^1, \sigma_z^1, \dots\}$. These operators obviously satisfy the requirements of Eq. (2.2): Pauli matrices are trace-orthogonal, commute on different sites, and form an SU(2) group on the same site. A more general set of operators would be all those local to a cluster of spins, eg like that of Fig. 2·2. One such set of operators of this form could be all sets of products of Pauli operators acting on different sites, as is outlined in Eq. (2.23) for a 2-site clustering.

This basis of pauli strings is useful because it has transparent physical interpretation. However for sampling and numerical purposes it is more convenient to use the basis of rank 1 matrices Y_{nm}, $n = 0, 1 \dots D-1$, $m = 1, 2 \dots n$, defined as

$$m = n \quad Y_{nn} = |n\rangle\langle n|, \tag{2.3}$$

$$m < n \quad Y^{(+)}_{nm} = \frac{1}{\sqrt{2}}(|n\rangle\langle m| + |m\rangle\langle n|), \tag{2.4}$$

$$Y^{(-)}_{nm} = \frac{i}{\sqrt{2}}(|n\rangle\langle m| - |m\rangle\langle n|), \tag{2.5}$$

where $|n\rangle$ is the n-th state in the standard product basis of spins polarized in the z-direction. We use the convention that $|0\rangle = |\uparrow\uparrow \dots \uparrow\rangle$, $|1\rangle = |\downarrow\uparrow \dots \uparrow\rangle$, ...

These operators are explicitly Hermitian clearly forming a complete operator basis. The structure constants for these operators are easy to find from the commutation relations, e.g.

$$[Y^{(+)}_{nm}, Y^{(-)}_{pq}] = \frac{i}{\sqrt{2}} \left(\delta_{mp} Y^{(+)}_{nq} + \delta_{np} Y^{(+)}_{mq} - \delta_{nq} Y^{(+)}_{mp} - \delta_{mq} Y^{(+)}_{np} \right). \tag{2.6}$$

This operator basis has the convenience that one is no longer restricted to spin 1/2 systems: instead, for a general Hilbert space dimension D generated by some clustering scheme, one can simply and efficiently define the $D^2 - 1$ basis operators. Note that the index α for $\{X_\alpha\}$ becomes a compound index $\alpha = (\pm, n, m, i')$, including the indexing of the Y operators, as well as the cluster index i' (i' is used to denote cluster indexing, while i is used to denote physical spin indexing).

Next, identify basis operators $\{X_\alpha\}$ to classical phase space variables $\{x_\alpha\}$ satisfying canonical Poisson bracket relations defined through the structure constants $f_{\alpha\beta\gamma}$

$$X_\alpha \to x_\alpha - \frac{i}{2} x_\beta f_{\alpha\beta\gamma} \frac{\partial}{\partial x_\gamma}; \quad \{x_\alpha, x_\beta\} = -f_{\alpha\beta\gamma} x_\gamma. \tag{2.7}$$

These Poisson brackets are obtained from a standard rule $i[A, B] \to \{A(\{x\}), B(\{x\})\}$, where A, B are functions in on phase space variables $\{x\}$. This mapping definesthe Weyl symbol for writing functions in phase space. Note that operators must always be chosen to be as linear as possible, with some subtleties for time correlators to be discussed later.

A general operator O can be written as a sum of basis operators, so that the the function over phase space ends up looking like a dot product. Importantly, the derivative $\partial/\partial x_\gamma$ acts with respect to the *coordinate* $\{x\}$ and not the operator prefactor o_α

$$O = \sum_\alpha o_\alpha X_\alpha \quad \Rightarrow \quad O(\{x\}) = \sum_\alpha x_\alpha o_\alpha. \tag{2.8}$$

A point in phase space $\{x\}$ can equivalently be written as an operator

$$\{x\} \quad \rightarrow \quad \rho(x) = \bigotimes_{i'} \Big(\sum_\alpha x_\alpha^{i'} X_\alpha \Big) \tag{2.9}$$

where the product is over all clusters i', and the sum is over all operators within each cluster with respect to the phase space point now compositely indexed by operator α and cluster i. This is especially transparent if the basis is the Y operators; then, the point $\{x\}$ is the real and imaginary components of the operator $\rho(x)$ in the chosen Hilbert space basis.

Operators such as the Hamiltonian and observables can be mapped to equivalent functions of phase space by first representing them in the basis of $\{X_\alpha\}$, then writing the operators in the Bopp representation of Eq. (2.7). Note that this means that terms which were originally products of two operators such as eg $\sigma_z^0 \sigma_z^1$ may be mapped to linear operators within a cluster

$$H = \sum_j B_a^j \sigma_a^j + \sum_{ij} J_{ab}^{ij} \sigma_a^i \sigma_b^j + \dots \tag{2.10}$$

$$= \sum_{i'} \tilde{B}_\alpha^{i'} X_\alpha^{i'} + \sum_{i'j'} \tilde{J}_{\alpha\beta}^{i'j'} X_\alpha^{i'} X_\beta^{j'} + \dots \tag{2.11}$$

$$\Downarrow$$

$$H(\{x\}) = \sum_{i'} \tilde{B}_\alpha^{i'} x_\alpha^{i'} + \sum_{i'j'} \tilde{J}_{\alpha\beta}^{i'j'} x_\alpha^{i'} x_\beta^{j'} + \dots \tag{2.12}$$

where ellipsis represent higher order terms which represent interactions between three or more clusters. This can be similarly done for observables. Formally, this is computing the Weyl symbol (Polkovnikov, 2010) of operators as functions in a phase space.

Expectation values of observables are defined by a trace of the density function with the observable. The trace is equivalent to an integral over phase space with respect to the **Wigner function** $W(\{x\})$, which is the Weyl symbol of the density function ρ

$$\mathrm{Tr}\big[\rho\mathcal{O}\big] = \int dx W(x)O(x). \tag{2.13}$$

The exact Wigner function is motivated by Schwinger Bosons (see section 2.6) but in general is highly negative, as it is the equivalent of a Fock state of a single Boson in a very large number of sites. Instead, we write the Wigner function as a Gaussian, motivated from coherent states:

$$\begin{aligned} W(\{x\}) &= \frac{1}{Z}\exp\left[(x_\alpha - \rho_\alpha)\Sigma_{\alpha\beta}(x_\beta - \rho_\beta)\right], \\ \mathrm{Tr}\big[\rho X_\beta\big] &= \int \prod_\alpha dx_\alpha\, x_\beta\, W(\{x\}), \\ \mathrm{Tr}\big[\rho(X_\beta X_\gamma + X_\gamma X_\beta)\big] &= 2\int \prod_\alpha dx_\alpha\, x_\beta x_\gamma W(\{x\}). \end{aligned} \tag{2.14}$$

The mean ρ_α and variance $\Sigma_{\alpha\beta}$ are choosen to match the equivalent quantum expectation value and symmetric correlation function. While this choice for the Wigner function looks a little ad-hoc, there are several reasons justifying such a choice (beyond the fact that it is easy to sample):

Standard TWA, which is formally controlled by $\hbar$ or $1/S$ in the spin models with large S corresponding to the classical limit, is only accurate to the order $\hbar^2$ or $1/S^2$ (see Ref. (Polkovnikov, 2010)). For this reason one can approximate the Wigner function to the same order without the loss of accuracy. For pure spin states, e.g. states polarized along the z-axis, higher order cumulants are sup-

pressed[1] by powers of $1/S$ and so it is only necessary to correctly describe first two cumulants: the mean and the variance. Any mixed state can be represented as a statistical mixture of pure states, so the associated Wigner function can be approximated as a sum of Gaussian distributions with non-negative weights. Interestingly in Ref. (Davidson and Polkovnikov, 2015) it was observed numerically that in the $SU(3)$ case the Gaussian Wigner function results in a slightly better approximation to dynamics than the exact Wigner function.

Fixing second moments of the Wigner Function ensures that cTWA is asymptotically exact at short times up to the order $\mathcal{O}(t^2)$, which is the same accuracy as normal TWA. Similarly, the mean-field approximation, which sets all fluctuations to zero, is only accurate to the linear order in time. This can be seen by Taylor expanding the evolution of some operator O. In linear order the response will be determined by the initial expectation value of the commutator $\langle\psi_0|[O,H]|\psi_0\rangle$, which is by construction is linear in cluster variables for any product state $|\psi_0\rangle$. In the next t^2 order, the response will involve expectations values of the higher order commutators like $\langle\psi_0|[[O,H],H]|\psi_0\rangle$. It is straightforward to check that such double commutators will involve only linear or quadratic terms in the cluster operators, which are again guaranteed to be exactly reproduced by the Gaussian Wigner function. We point in this respect that absence of fluctuations in initial conditions in dynamic mean-field approximations generally leads to the mistake in the expectation value of the double commutator and hence leads only to accuracy up to the linear order in t. Therefore initial quantum fluctuations encoded in the width of the Wigner function guarantee the correct short time dynamics. Beyond the order t^2 there are generally quantum jump contributions to the dynamics,

[1]For standard $SU(2)$ spins this fact trivially follows that in the classical limit the polarized spin is represented by the non-fluctuating δ-function distribution and fluctuations are quantum coming from non-commutativity of spin components. Similar arguments can be applied to higher-dimensional spins.

which go beyond TWA (Polkovnikov, 2010), and so going beyond the Gaussian approximation of the Wigner function will generally not improve the accuracy of cTWA, at least at short times.

The Gaussian is well-defined

One important question is if this Gaussian is well defined, eg the correlation matrix $\Sigma_{\alpha\beta}$ is positive-definite. If some of the eigenvalues are negative, that means that the probability *increases* further away from the mean, instead of decreases, and so the gaussian is no longer normalizable.

Let us show that this is never the case by beginning with a simple case and then proving the general case. First, suppose some (finite) Hilbert space, a complete (exponentially large) set of operators $\{X_\alpha\}$ and a wave function $|\psi\rangle$. Because the operator basis is complete, we have freedom to choose it arbitrarily[2]. Let us choose an orthogonal Hilbert space basis generated by $\{|\psi\rangle = |0\rangle, |1\rangle, \ldots |\mathcal{D}-1\rangle\}$, where the zeroth element is the (potentially highly entangled) wavefunction. Let us choose the trace-orthogonal operator basis as the $Y^{\pm}_{ab}$. It is simple to show that in this basis, there is only one non-zero expectation value, and the values $\{y\}$ are uncorrelated:

$$A_\alpha = \langle 0|(|a\rangle\langle b| \pm |b\rangle\langle a|)|0\rangle = \delta_{\alpha 0} \tag{2.15}$$

$$C_{\alpha\beta} = \langle 0|(|a\rangle\langle b| \pm |b\rangle\langle a|)(|c\rangle\langle d| \pm |d\rangle\langle c|)|0\rangle - \delta_{\alpha 0}\delta_{\beta 0} \tag{2.16}$$

$$= \delta_{0a}\delta_{bc}\delta_{d0} \pm \delta_{0a}\delta_{bd}\delta_{c0} \pm \delta_{0b}\delta_{ac}\delta_{d0} + \delta_{0b}\delta_{ad}\delta_{c0} - \delta_{\alpha 0}\delta_{\beta 0} \tag{2.17}$$

[2]The eigenvalues of the correlation matrix are basis independent and thus we can choose as simple a basis as possible.

Although this construction is a bit obtuse, it is then a simple exercise to show that this generates a matrix with at most one non-zero element per column (delta functions) where one of the indices must be 0 (the δ_{*0}). For a more in-depth version of this, see section 2.3. Similarly, the values in this matrix must be GEQ 0 as there is only a single negative component. This means that **for a complete set of operators, the correlation matrix is always positive-definite.**

If the set of operators forms a smaller subgroup (for example, that of clusters), the above observation implies that the correlation matrix is positive for any subset of operators. For example, suppose a subset $\{Y_a\} \subset \{X_\alpha\}$ and a general wave function $|\psi\rangle$. Each operator can be constructed of the larger set via some matrix U: $Y_a = U_{a\alpha} X_\alpha$. Thus, the correlation matrix for $\{y\}$ is simply that of $\{x\}$ projected to the subspace: $C_{ab} = U_{a\alpha} C_{\alpha\beta} U^\dagger_{b\beta}$. This projection preserves the positivity of eigenvalues (as the sum of positive numbers are also positive). Another way of seeing it is to draw numbers $\{x\}$ from the full correlation matrix, then ignoring any numbers which are not part of the subset. This means that **for any closed group of operators and general state $|\psi\rangle$, the correlation matrix is always positive-definite**

With this result in hand, it is a true claim that for any initial wave function, even ones with very large entanglement between sites, any well-defined phase space basis has a well defined Gaussian Wigner function, in that the correlation matrix is postive definite.

Time Dynamics

Time dynamics in phase space is induced from the Heisenberg equation of motion for the density operator

$$i\partial_t \rho = \big[\rho, H\big] \quad \Rightarrow \quad \partial_t W(x) = \big\{W(x), H(x)\big\} \tag{2.18}$$

where $\{*,*\}$ represents the Moyal bracket (Hillery et al., 1984) inheriting the group structure of the quantum operators. Note that this is the truncation of the truncated Wigner approximation. In standard Bosonic TWA, the Weyl symbol of a commutator will generally have many other terms which are both higher-order in $\hbar$ and higher-order in the power of derivatives. However, it is not clear what the higher-order corrections for the cTWA are.

The Moyal bracket has the property that phase space volume is conserved, which means that dynamics can be computed by the method of characteristics. Instead of evolving the function $W(x,t)$, instead one can sample points in the phase space $\{x\}$ and evolve each independently

$$\partial_t x_\alpha = f_{\alpha\beta\gamma} \frac{\partial H(x)}{\partial x_\beta} x_\gamma. \tag{2.19}$$

Using the equivalent definition of a point in phase space represented by an operator (equation (2.9)), the time evolution may be equivalently be written as dynamics of operators under the Heisenberg equation of motion

$$i\partial_t \rho(x) = \big[\rho(x), H(x)\big] \tag{2.20}$$

subject to the constraint that $\rho(x)$ must remain a product state between clusters. This is the same as projective evolution of operators, which has compelling relations to other time variational methods such as TDVP and matrix product state evolution. The fact that these time dynamics can be recast in this way means that if the cluster size becomes the system size, dynamics become exact.

Expectation values of observables in time can be computed by averaging over

the indepenently sampled and evolved points in phase space

$$\langle \mathcal{O}(t) \rangle \approx \int dx W(x) O\big(x(t)\big) = \overline{\mathrm{Tr}\big[\rho(x,t)\mathcal{O}\big]} \tag{2.21}$$

where the second equation is equivalent due to the trace-orthogonality of the operator basis. The fact that expectation values and time evolution can be represented by constrained projective time evolution of operators means that one in fact never has to deal with using the phase space coordinate system $\{x\}$ and structure functions $f_{\alpha\beta\gamma}$, instead only using operators, which is computationally much simpler. The numerical implementation of this method uses heavy use of this fact, and underlying everything is simply the projective evolution of product state operators $\rho(x)$.

Example: cluster TWA for four coupled spins.

Let us illustrate how one can apply cTWA to a simple system of four coupled spins shown in Fig. 2·3, which is described by the Hamiltonian

$$H = J \sum_{j=1}^{3} \sigma_z^j \sigma_z^{j+1} + h_x \sum_{j=1}^{4} \sigma_x^j. \tag{2.22}$$

In this example one can consider clusters of size one, two, and four. The size one cluster leads to standard TWA for spins (Polkovnikov, 2010), while the size four cluster leads to exact representation of dynamics by the cTWA. Size two clusters should be still approximate but lead to an improved accuracy of the method compared to the standard TWA, and will be detailed here, going through the steps highlighting how they are implemented in this example.

1. This model system is split into two size two clusters, $1' \equiv L$ and $2' \equiv R$. The Hilbert space dimension of the cluster is $D = 4$ and the dimension

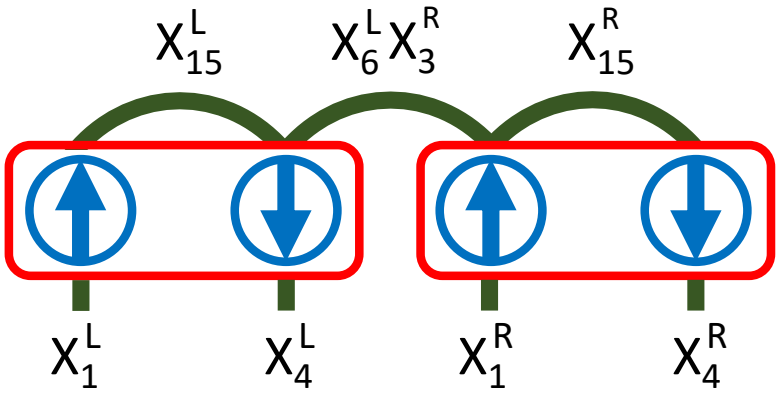

Figure 2·3: Representation of the 4-spin Ising example. Blue circles and arrows represent the physical spins in the initial Neel state, while red rectangles show the clusters labeled by $i' = L, R$. Green arches represent the nearest-neighbor $\sigma_z^{(j)}\sigma_z^{(j+1)}$ couplings, with the relevant representation through the cluster operators $X_\alpha^{L,R}$. Bottom lines represent the on-site $\sigma_x^{(j)}$ fields in terms of the cluster operators. In this way the original Hamiltonian (2.22) exactly maps to the two-cluster Hamiltonian (2.25)

of the operator basis spanning $SU(4)$ algebra plus identity is $D^2 = 16$. A possible and convenient choice for the operator basis in the first cluster (and similarly in the second cluster) is:

$$\begin{array}{lll} X_0 = I^{(1)} \otimes I^{(2)} & & \\ X_1 = \sigma_x^{(1)} \otimes I^{(2)}, & X_2 = \sigma_y^{(1)} \otimes I^{(2)}, & X_3 = \sigma_z^{(1)} \otimes I^{(2)} \\ X_4 = I^{(1)} \otimes \sigma_x^{(2)}, & X_5 = I^{(1)} \otimes \sigma_y^{(2)}, & X_6 = I^{(1)} \otimes \sigma_z^{(2)} \\ X_7 = \sigma_x^{(1)} \otimes \sigma_x^{(2)}, & X_8 = \sigma_x^{(1)} \otimes \sigma_y^{(2)}, & X_9 = \sigma_x^{(1)} \otimes \sigma_z^{(2)} \\ X_{10} = \sigma_y^{(1)} \otimes \sigma_x^{(2)}, & X_{11} = \sigma_y^{(1)} \otimes \sigma_y^{(2)}, & X_{12} = \sigma_y^{(1)} \otimes \sigma_z^{(2)} \\ X_{13} = \sigma_z^{(1)} \otimes \sigma_x^{(2)}, & X_{14} = \sigma_z^{(1)} \otimes \sigma_y^{(2)}, & X_{15} = \sigma_z^{(1)} \otimes \sigma_z^{(2)}, \end{array} \tag{2.23}$$

where superscripts 1 and 2 refer to the first and the second site of the cluster. It is easy to check that these basis operators satisfy the required normalization conditions.

2. The structure constants are easy to get from the commutation relations of

the Pauli matrices. There are in total 20 independent structure constants in this operator basis. Let us explicitly show a few of them:

$$\begin{aligned} [X_1, X_2] &= 2iX_3 \Rightarrow f_{1,2,3} = 2, \\ [X_7, X_{10}] &= 2iX_3 \Rightarrow f_{7,10,3} = 2. \end{aligned} \tag{2.24}$$

3. In terms of the cluster operators the Hamiltonian (2.22) reads

$$H = J\left(X_{15}^L + X_{15}^R + X_6^L X_3^R\right) + h_x\left(X_1^L + X_4^L + X_1^R + X_4^R\right). \tag{2.25}$$

Note that this Hamiltonian contains only a single nonlinear coupling between the operators X_6^L and X_3^R. When written in terms of Pauli matrices (single site clusters) the Hamiltonian has three non-linear couplings.

4. Identify fifteen phase space variables per each cluster $x_1^{L,R} \ldots x_{15}^{L,R}$ satisfying the Poisson bracket relations with the structure constants determined above.

5. Define the classical Hamiltonian $H(\{x\})$:

$$H(\{x\}) = J\left(x_{15}^L + x_{15}^R + x_6^L x_3^R\right) + h_x\left(x_1^L + x_4^L + x_1^R + x_4^R\right). \tag{2.26}$$

6. Consider an initial product state

$$|\psi_0\rangle = |\uparrow\downarrow\uparrow\downarrow\rangle,$$

which is an eigenstate of the Hamiltonian with $h_x = 0$. Then this setup can be regarded as a quench from this initial state. The Gaussian Wigner function for this state factorizes into a product of left and right Wigner functions W_L and W_R. For the left cluster (and similar for the right cluster) the nonzero expectation values have only the following three operators

$$\langle\psi_0|X_3^L|\psi_0\rangle = 1,\ \langle\psi_0|X_6^L|\psi_0\rangle = -1,\ \langle\psi_0|X_{15}^L|\psi_0\rangle = -1. \tag{2.27}$$

There are 24 non-zero symmetric correlation functions excluding the identity for the left cluster (and similar for the right cluster):

$$\begin{aligned}
&\left\langle\psi_0\right|\left(X_\alpha^L\right)^2\left|\psi_0\right\rangle = 1, \quad \alpha \in \{1,\ldots,15\} \\
&\frac{1}{2}\langle\psi_0|\{X_\alpha^L, X_\beta^L\}_+|\psi_0\rangle = 1 \\
&\qquad (\alpha,\beta) \in \left[(4,13)\quad (5,14)\quad (6,15)\quad (7,11)\right] \\
&\frac{1}{2}\langle\psi_0|\{X_\alpha^L, X_\beta^L\}_+|\psi_0\rangle = -1 \\
&\qquad (\alpha,\beta) \in \left[(1,9)\quad (2,12)\quad (3,6)\quad (3,15)\quad (8,10)\right],
\end{aligned} \tag{2.28}$$

where $\{A,B\}_+$ stands for anti-commutator. The fact that

$$\langle\psi_0|X_8^2|\psi_0\rangle = \langle\psi_0|X_{10}^2|\psi_0\rangle = -\frac{1}{2}\langle\psi_0|\{X_8, X_{10}\}_+|\psi_0\rangle = 1$$

implies that the phase space variables x_8 and x_{10} should be perfectly anti-correlated. After finding the connected correlators, the associated Gaussian Wigner functions W_L and W_R read

$$\begin{aligned}
W_L = \frac{1}{Z}&\delta(x_3-1)\delta(x_6+1)\delta(x_{15}+1)\delta(x_4-x_{13})\delta(x_5-x_{14}) \\
&\times \delta(x_1+x_9)\delta(x_2+x_{12})\delta(x_7-x_{11})\delta(x_8+x_{10}) \\
&\times \exp\left[-\frac{\sum_{\alpha\in\{1,2,4,5,7,8\}} x_\alpha^2}{2}\right],
\end{aligned} \tag{2.29}$$

where Z is the normalization constant. The δ-functions can be understood as limiting cases of Gaussians and thus are allowed in our ansatz. We see

that each initial condition must draw 12 uncorrelated numbers (6 per each cluster).

7. Now we need to solve the system of classical equations of motion (2.19) for our phase space variables with the initial conditions $x_\alpha^{L,R}(t=0)$ randomly sampled from the left and right Wigner functions (2.29). There are overall thirty equations: fifteen for left variables and fifteen for right variables (the variables $x_0^{L,R}$ corresponding to identity operators are obviously conserved in time). Let us explicitly show a few of them:

$$\begin{aligned} \partial_t x_4^L &= J x_3^R x_5^L + J x_{14}^L \\ \partial_t x_3^L &= -h x_2^L \\ \partial_t x_{12}^L &= -h x_{11}^L + h x_{15}^L - J x_1^L. \end{aligned} \tag{2.30}$$

8. Finding expectation values of observables is done by averaging the corresponding Weyl symbols computed on time-dependent phase space points over the initial conditions. For example:

$$\begin{aligned} \langle \sigma_z^1(t)\sigma_z^2(t)\rangle = \langle X_{15}^L(t)\rangle &\approx \overline{x_{15}^L(t)}, \\ \langle \sigma_z^2(t)\sigma_z^3(t)\rangle = \langle X_6^L(t) X_3^R(t)\rangle &\approx \overline{x_6^L(t) x_3^R(t)}, \\ \langle \sigma_z^1(t)\rangle = \langle X_3^L(t)\rangle &\approx \overline{x_3^L(t)}. \end{aligned} \tag{2.31}$$

In Fig. 2·4 we show the results of simulations using the cluster TWA. For comparison we also show the single cluster (conventional) TWA and exact results. For simulations we choose specific parameters: $J = \frac{1}{8},\ h_x = 1$.

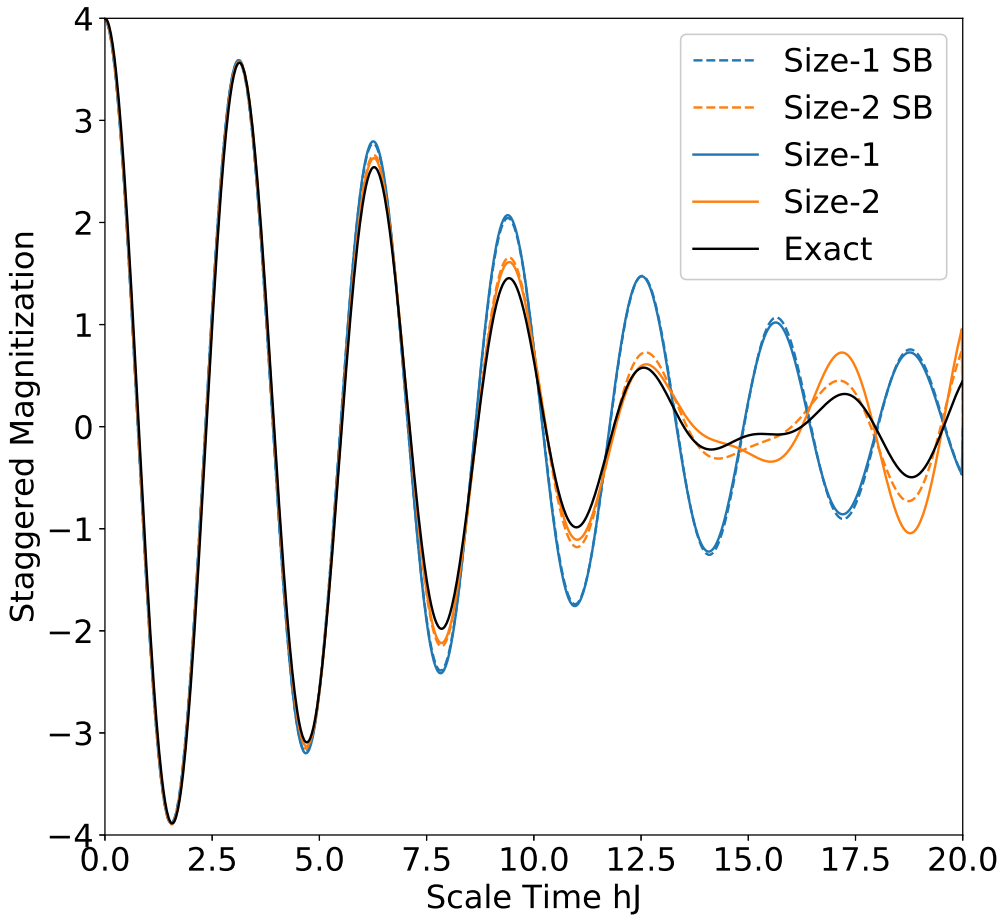

Figure 2·4: Dynamics of the staggered magnetization in the 4-spin Transverse Ising example. Solid black represents the exact result, while the solid (dashed) colored lines are the results of the Operator (Schwinger Boson) CTWA. The staggered magnetization is represented by $\overline{x_3^L + x_3^R - x_6^L - x_6^R}$. CTWA dynamics approach exact results with increasing cluster size.

2.2 Symmetric and anti-symmetric correlation functions

Another important part of the cTWA, which highlights many of the subtleties of the method, is computing symmetric and anti-symmetric time correlation functions. The start of this analysis comes from defining the time evolution of points in phase space via a canonical transformation $M(x,t)$

$$\vec{x}(t) = \overline{M}(x,t)\vec{x}. \tag{2.32}$$

If evolution is linear (eg no inter-cluster interactions) then M has no dependence on the initial point x and is simply a rotation, with dynamics being exact. Then expectation values of observables may be written as

$$\begin{aligned}\langle O\rangle &= \int dx W(x)O(x) = \sum_i \int dx W(x)x_i(t)O_i \\ &= \sum_{ij}\int dx W(x)x_j M_{ij}(t)O_i = \sum_j \int dx W(x)x_j O_j(t).\end{aligned} \tag{2.33}$$

The mapping $M_{ij}(t)O_i$ corresponds to translations of a lattice over discrete phase space, as described by (Gibbons et al., 2004), and is equivalent to a Heisenberg picture of evolution, where observables are evolved in time instead of operators. In this case, the Heisenberg and Schrödinger pictures are equivalent and the cTWA dynamics are exact.

Next, we wish to compute **time correlation functions**. Using the Bopp representation of two operators A and B we find

$$\langle A(t)B(t')\rangle = \int dx W(x)\Big[x_\alpha(t)\big(A_\alpha + A_\beta f_{\alpha\beta\gamma}\frac{\partial}{\partial x_\gamma(t)}\big)\Big]\Big[x_\epsilon(t')B_\epsilon\Big] \tag{2.34}$$

$$= \int dx W(x) x_\alpha(t)x_\epsilon(t')A_\alpha B_\epsilon + x_\alpha(t)A_\beta B_\epsilon f_{\alpha\beta\gamma}\frac{\partial x_\epsilon(t')}{\partial x_\gamma(t)}. \tag{2.35}$$

The structure function $f_{\alpha\beta\gamma}$ is antisymmetric. This means that the symmetric correlation function $\{A, B\}_+ = AB + BA$ and antisymmetric correlation functions $[A, B] = AB - BA$ become

$$\langle\{A(t), B(t')\}_+\rangle = 2\int dx W(x)A\big(x(t)\big)B\big(x(t')\big) \tag{2.36}$$

$$\langle[A(t), B(t')]\rangle = \int dx W(x)x_\alpha(t)A_\beta B_\epsilon f_{\alpha\beta\gamma}\frac{\partial x_\epsilon(t')}{\partial x_\gamma(t)}. \tag{2.37}$$

Observe that the antisymmetric response looks like some response to perturbations: the derivative can be seen as how the phase space point $x(t')$ changes with respect to an infinitesimal change at an earlier time t. The derivative per point in phase space can be computed by co-evolving two points infinitesimally separated by some distance ϵ_γ, then subtracting the two and dividing by $|\epsilon|$.

If the evolution is linear, as discussed above, then the derivative is also linear. This means that time dynamics of the antisymmetric commutator are also exact, as can be seen by setting $t = 0$

$$\langle[A(0), B(t')]\rangle = \int dx W(x)x_\alpha(0)A_\beta B_\epsilon f_{\alpha\beta\gamma}M_{\epsilon\gamma}(t) \tag{2.38}$$

$$= \int dx W(x)x_\alpha(0)A_\beta B_\gamma(t)f_{\alpha\beta\gamma}. \tag{2.39}$$

Once again this emphasizes the equivalence of Schrödinger and Heisenberg

pictures for linear evolution.

2.3 Dimensional reduction

One of the powerful things about Gaussian Wigner functions is the fact there are a lot of symmetries in the sampling. The phase space per cluster is of dimension $\mathcal{D}^2$, eg 4^N, one for each of the operators. Intriguingly, for a Gaussian Wigner and pure initial state, the complexity of the system can be reduced from this D^2 to $2D$. To see this let us define a Hermitian matrix y consisting of elements y_{nn} on diagonal , $y_{mn} = 1/\sqrt{2}(y_{mn}^{(+)} - iy_{mn}^{(-)})$ on the upper triangular and $y_{nm} = 1/\sqrt{2}(y_{mn}^{(+)} + iy_{mn}^{(-)})$ on the lower triangular. Suppose WLOG that the initial condition is a pure state $|\psi\rangle = |0\rangle$. From Eq. (2.14) it follows that the only nonzero matrix elements of y are $y_{00} = 1$, y_{0n} and y_{n0}:

$$y = \begin{pmatrix} 1 & \frac{\delta_1 - i\sigma_1}{2} & \frac{\delta_2 - i\sigma_2}{2} & \dots & \frac{\delta_D - i\sigma_D}{2} \\ \frac{\delta_1 + i\sigma_1}{2} & 0 & 0 & \dots & 0 \\ \frac{\delta_2 + i\sigma_2}{2} & 0 & 0 & \dots & 0 \\ \vdots & \vdots & \vdots & \ddots & \vdots \\ \frac{\delta_D + i\sigma_D}{2} & 0 & 0 & \dots & 0 \end{pmatrix} \tag{2.40}$$

with δ and σ being drawn from a Gaussian of variance 1 and mean 0.

This matrix has only 2 non-zero eigenvalues $\lambda_\pm$, allowing us to express it as

$$y = \lambda_+ |\psi_+\rangle\langle\psi_+| + \lambda_- |\psi_-\rangle\langle\psi_-|, \tag{2.41}$$

where $|\psi_\pm\rangle$ are the eigenvectors of y corresponding to the two non-zero eigenvalues $\lambda_\pm$, which can be obtained from the characteristic polynomial:

$$f(\lambda) = (-\lambda)^{D-2} \left((1-\lambda)(-\lambda) - \frac{1}{4} \sum_{i=1}^{D-1} (\delta_i^2 + \sigma_i^2) \right). \tag{2.42}$$

Then the only two non-zero eigenvalues are

$$\lambda_\pm = \frac{1}{2} \pm \frac{1}{2}\sqrt{1 + \sum_{i=1}^{D-1}(\delta_i^2 + \sigma_i^2)}. \tag{2.43}$$

The eigenvalues can be interpreted as quasi-probabilities, since $\lambda_+ + \lambda_- = 1$. Note that one the eigenvalues is exponentially large and positive while the other is always negative. Alternatively one can think of them as the components of an auxiliary spin 1/2 degree of freedom per cluster. Note that the eigenvalue only depends on the sum of all the δ_i and σ_i. Given that they are Gaussian i.i.d. variables, the eigenvalues converge to

$$\lambda_\pm \approx \frac{1}{2} \pm \frac{1}{2}\sqrt{2D-1} \approx \frac{1}{2} \pm \sqrt{\frac{D}{2}}, \tag{2.44}$$

in the large D limit. Fluctuations in the eigenvalues from realization to realization are subleading and of order $O(D^{1/4})$. The eigenvectors on the other hand become,

$$\begin{aligned} \langle 0|\psi_\pm\rangle &= \sqrt{\frac{\lambda_\pm^2}{\lambda_\pm^2 + 1/2}}, \\ \langle i|\psi_\pm\rangle &= \sqrt{\frac{\lambda_\pm^2}{\lambda_\pm^2 + 1/2}}\frac{\delta_i + i\sigma_i}{2\lambda_\pm} \quad \forall\, i > 0. \end{aligned} \tag{2.45}$$

For sufficiently large clusters this behaves as

$$\begin{aligned} \langle 0|\psi_\pm\rangle &\approx 1, \\ \langle i|\psi_\pm\rangle &\approx \pm\frac{\delta_i + i\sigma_i}{\sqrt{2D}} \quad \forall\, i > 0. \end{aligned} \tag{2.46}$$

Both eigenvectors of y are therefore the initial state $|0\rangle$ supplemented by exponentially small noise in cluster size. This is the primary reason why cTWA doesn't suffer from any problematic noise accumulation. Indeed, from (2.40) it might have appeared that cTWA is adding an exponential amount of noise to the initial

conditions. However, the above analysis shows that it actually results in exponentially large eigenvalues with exponential suppression of the fluctuations in each of the eigenvectors. It can be shown using the equations of motion (2.19) that these eigenvalues are conserved in time, and thus the noise remains confined at *all* times.

We can use conservation of $\lambda_\pm$ to further reduce the number of equations of motion for the phase space variables from naive $\mathcal{O}(ND^2)$, where N is the number of clusters to $\mathcal{O}(ND)$. This is because Heisenberg evolution (even if projected to product states) conserves the eigenspectrum of the evolved operator. Because there are only two non-zero eigenvalues, it suffices to only evolve those eigenvectors. For example, if we have two clusters denoted by L and R and a Hamiltonian:

$$H = H_L + H_R + JV_LV_R$$

then equations of motion for the variables y_{nm} are equivalent to equations of motion for the states $|\psi_\pm\rangle$ with each cluster. Thus

$$\begin{aligned} i\partial_t|\psi_\pm^L(t)\rangle = H_L|\psi_\pm^L(t)\rangle + JV_L|\psi_\pm^L(t)\rangle\times \\ \times\left(\lambda_+^{(R)}\langle\psi_+^R(t)|V_R|\psi_+^R(t)\rangle + \lambda_-^{(R)}\langle\psi_-^R(t)|V_R|\psi_-^R(t)\rangle\right), \end{aligned} \quad (2.47)$$

and similarly for the right two eigenvectors. At the end of the evolution the phase space variables $y_{nm}(t)$ for each for the clusters are obtained from the state vectors $|\psi_\pm^{(L,R)}\rangle$ according to Eq. (2.41).

2.4 General initial conditions

For states which are unentangled between clusters, it suffices to compute the Gaussian Wigner function for the all-up state $|\psi\rangle = |0\rangle$, as is done in section

2.3. This is because any other state which is unentangled between clusters may generally be done via a unitary coordinate rotation $x_\alpha \to U_{\alpha\beta}x_\beta$. Sometimes it is easier to to do instead a local (intra-cluster) Hamiltonian evolution, where cTWA is exact. For example, for the state $|\downarrow\uparrow\uparrow\rangle$ we can sample a point from the Wigner function corresponding to the state $|0\rangle = |\uparrow\uparrow\uparrow\rangle$, then evolve the Hamiltonian $H = \sigma_x^0$ for time $t = \pi$. It is easy to prove that this way of sampling the initial conditions is equivalent to sampling from the Gaussian Wigner function corresponding to the state $|\downarrow\uparrow\uparrow\rangle$. In this way, product state initial states can be readily generated. E.g. for the Neel state one can first sample the state $|0\rangle$ and then apply the Hamiltonian $H = \sum_{i \text{ even}} \sigma_x^i$ for time $t = \pi/2$. The Wigner function for a random state is produced in a similar fashion by applying the Hamiltonian $H = \sum_i h_x^i\sigma_x^i + h_y^i\sigma_y^i + h_z^i\sigma_z^i$ for $t = \pi$ with magnetic fields $\vec{h}$ chosen from an appropriate distribution.

For general states which do have entanglement between clusters, the Gaussian Wigner function becomes a bit more tricky. This is because there now exist correlations between clusters, and thus the Wigner function no longer factorizes between clusters. As is discussed above, in the entangled case it is possible in general to compute a gaussian Wigner function; however, it may no longer reproduce all observables at $t = 0$, as observables may not factorize at a Gaussian level. One example of such a state is a W state, defined as a superposition of a single up state: $|\psi\rangle = |\uparrow\downarrow\downarrow\rangle + |\uparrow\downarrow\uparrow\rangle + |\uparrow\uparrow\downarrow\rangle$. This state is a primitive for a tripartite entanglement state, and for 3 size-1 clusters the cTWA does not reproduce all expectation values. For example

$$\langle Z_0Z_1Z_2\rangle \neq \frac{1}{3}\Big(\langle Z_0\rangle\langle Z_1Z_2\rangle + \langle Z_1\rangle\langle Z_0Z_2\rangle + \langle Z_2\rangle\langle Z_0Z_1\rangle\Big). \tag{2.48}$$

Here, the observables were factorized at a Gaussian level, which is what the

cTWA would reproduce. The exact expectation value is $\langle Z_0 Z_1 Z_2 \rangle = -1$. At the Gaussian level, $\langle Z_i \rangle = -\frac{1}{3}$ and $\langle Z_i Z_j \rangle = -\frac{1}{3}$. Thus the CTWA expectation value would be $1/9 \neq -1$.

For Bell states, however, this Gaussian factorization is possible. A Bell state is defined as a W state for two spins, eg $|\psi\rangle = |10\rangle + |01\rangle$. More generally, if entanglement is such that it is captured at the Gaussian level between clusters (eg $|1111\rangle + |0000\rangle$ between two size-2 clusters), this factorization is still possible because observables are no larger then quadratic.

Dimensional reduction for general initial conditions

A final comment on general initial conditions is a point of care for dimensional reduction. The reduction from 4^N to 2^N degrees of freedom came from a special form of the wavefunction being unentangled between clusters. However, for entangled wavefunctions this is no longer the case: generically one still needs all 4^N variables, as all eigenvalues of the reduced density matrix are nonzero.

2.5 Discrete vs. continuous Wigner functions

Alternate Wigner functions exist, as described by eg (Wootters, 1987). Under Wootter's formalism, the Wigner function is discrete, choosing from only certain values of initial conditions. While the Wigner function may be different, all of the different parts of the cTWA remain the same: time dynamics are still of points in phase space, except that the initial points are chosen from some small discrete number of places instead of from some continuum.

The phase space is written in terms of phase point operators A, in analogy to the phase point operators of continuous phase space:

$$
\begin{aligned}
A_0 &= 1 + \sigma_x + \sigma_y + \sigma_z, \\
A_1 &= 1 + \sigma_x - \sigma_y - \sigma_z, \\
A_2 &= 1 - \sigma_x + \sigma_y - \sigma_z, \\
A_3 &= 1 - \sigma_x - \sigma_y + \sigma_z.
\end{aligned} \tag{2.49}
$$

These phase point operators have all the same properties as the complete basis of operators $\{\hat{X}_\alpha\}$ and in fact can be used as a phase space coordinate system $\{x_0, \ldots, x_3\}$ The Weyl symbol of operators is now a discrete vector of points, analagous to the coefficents o_α for operator $\mathcal{O}$.

$$
\big(\mathcal{O}\big)_W = \mathrm{Tr}\big[A_\alpha \mathcal{O}\big] = \big(O_0, O_1, O_2, O_3\big). \tag{2.50}
$$

Similarly, the discrete Wigner function, which is the Weyl symbol of the density function, can be interpreted as the probability of choosing one of four points. For example, the Z up state may be written as

$$
\big(|\uparrow\rangle\langle\uparrow|\big)_W = \big(1/2, 0, 0, 1/2\big). \tag{2.51}
$$

Thus, one would sample evenly from two points in phase space, if one interprets the value $1/2$ as a probability. For a coordinate system corresponding to (x, y, z) one would choose uniformly between $\vec{x} = (1, 1, 1)$ and $\vec{x} = (-1, -1, 1)$. These points could then be evolved according to standard phase space evolution as above.

This discrete Wigner function runs into several problems. First, for states which are not stabilizer states (Mari and Eisert, 2012) such as Z-up there will generally be a negative component to this Wigner function. This means that it is generally more complicated to sample for more general initial conditions.

However, this negativity highlights an even worse problem: basis dependence. The choice of phase point operators is not unique; for example, one may choose an alternate set of phase point operators

$$\begin{aligned} A_0 &= 1 + \sigma_x - \sigma_y + \sigma_z, \\ A_1 &= 1 + \sigma_x + \sigma_y - \sigma_z, \\ A_2 &= 1 - \sigma_x - \sigma_y - \sigma_z, \\ A_3 &= 1 - \sigma_x + \sigma_y + \sigma_z, \end{aligned} \tag{2.52}$$

which has the same Wigner function, except now the initial point in phase space is chosen to be either $x = (-1, 1, 1)$ or $x = (1, -1, 1)$, as opposed to the previous choice with $x = (1, 1, 1)$ or $x = (-1, -1, 1)$. These choices induce false correlations into the system; the X and Y initial points are spuriously equal to each other. For example, if one chooses a 2-site Hamiltonian

$$H = \sigma_x^L \left(\sigma_x^R + \sigma_y^R\right) \tag{2.53}$$

then the first choice of phase point operators will cause the left site to see an effective X-field of 2 (as they add), while the second choice sees no effective on-site field (as they are opposite and cancel). **This means that different choices of phase point operator basis gives different time dynamics**– a big no-no.

2.6 Schwinger Bosons

An alternate choice of phase space parameterization is one of **Schwinger Bosons** (SB). This representation has the advantage of having of order 2^N degrees of freedom per cluster, as opposed to 4^N for the operator cTWA case. Another

advantage is its relation to existing Bosonic phase space methods; in fact, operator cTWA is just an additional extension of SB cTWA.

Schwinger Bosons are a way of treating quantum corrections for large spin dynamics. In a similar way as the Truncated Wigner approximation having an error time scale going as $\hbar$, so does the SB have error time scale going as $1/S$, the total spin of a site. This can be clearly seen when writing the phase space representation of a spin S. The operators S_x, S_y, S_z may be written as

$$S_x = \begin{bmatrix} a_0^\dagger & a_1^\dagger \end{bmatrix} \begin{bmatrix} 0 & 1 \\ 1 & 0 \end{bmatrix} \begin{bmatrix} a_0 \\ a_1 \end{bmatrix}, \tag{2.54}$$

$$S_y = \begin{bmatrix} a_0^\dagger & a_1^\dagger \end{bmatrix} \begin{bmatrix} 0 & -i \\ i & 0 \end{bmatrix} \begin{bmatrix} a_0 \\ a_1 \end{bmatrix}, \tag{2.55}$$

$$S_z = \begin{bmatrix} a_0^\dagger & a_1^\dagger \end{bmatrix} \begin{bmatrix} 1 & 0 \\ 0 & -1 \end{bmatrix} \begin{bmatrix} a_0 \\ a_1 \end{bmatrix}, \tag{2.56}$$

where the matrix product is implied. It is a simple exercise to check that the $SU(2)$ commutation relations of the spin operators are preserved by this representation; the commutator of two bosonic bilinear operators is another bilinear operator. The total spin of the site sets the total number of bosons $N_b = 2S$ and so large spin means large numbers of bosons, which is one of the classical limits of the TWA. The Weyl symbol of operator S, which is induced from the Weyl symbol of the underlying bosonic operators, can be found to be

$$S \to \vec{S} - \frac{i}{2}\big[\vec{S} \times \vec{\nabla}\big] - \frac{1}{8}\big[\vec{\nabla} + (\vec{S}\vec{\nabla})\vec{\nabla} - \frac{1}{2}\vec{S}\nabla^2\big] \tag{2.57}$$

(See (Polkovnikov, 2010) equation 88). With a large number of bosons, a Fock state (fixed boson number) can be confidently replaced with a coherent state with variable number of bosons. This would be the same as having a slightly fluctuating total spin. The Wigner function of such a coherent state is a Gaussian

and uniquely positive, and in the large Boson limit (large spin limit) the phase space dynamics approach the exact result.

Generalization of SB cTWA: larger Hilbert spaces

The fundamental generalization comes from representing larger Hilbert space operators in terms of Schwinger Bosons. Suppose some complete set of operators $\{X_\alpha\}$ which forms the operator basis for operator cTWA. Then, one may write the SB representation of that operator in terms of bosonic raising and lowering operators $a_i^\dagger$, a_j

$$X_\alpha \quad \Leftrightarrow \quad \sum_{ij} a_i^\dagger X_{ij}^\alpha a_j \tag{2.58}$$

Where now the index i runs over the Hilbert space of all of the clusters, and X_{ij} is the matrix representation of X_α in the basis chosen by indexing i. This is a generalization of Eq. (2.54), and is the same if the Hilbert space dimension is 2 where pauli matrices form a complete set of operators. The raising and lowering operators $a^\dagger$, a now represent adding or removing a boson from one of $\mathcal{D}$ sites, where $\mathcal{D}$ is the Hilbert space dimension of the cluster. As opposed to the large-spin SU(2) case, there is instead a single boson, whose "position" wave function can be interpreted as the many-body spin wave function of the system.

Now, the Hamiltonian and observables may be written in terms of these SBs. In the same way as for the operator cTWA, first recast operators into the basis $\{X_\alpha\}$, then re-write them in terms of bilinears

$$H = \sum_{i'} \tilde{B}^{i'}_{\alpha} X^{i'}_{\alpha} + \sum_{i'j'} \tilde{J}^{i'j'}_{\alpha\beta} X^{i'}_{\alpha} X^{j'}_{\beta} + \sum_{i'j'k'} \tilde{J}^{i'j'k'}_{\alpha\beta\delta} X^{i'}_{\alpha} X^{j'}_{\beta} X^{k'}_{\delta} + \dots \tag{2.59}$$

$$\Downarrow$$

$$H(a^\dagger, a) = \big(B^{i'}_{\alpha} X^{\alpha i'}_{ab}\big) a^\dagger_{ai'} a_{bi'} + \big(J^{i'j'}_{\alpha\beta} X^{\alpha i'}_{ab} X^{\beta j'}_{cd}\big) a^\dagger_{ai'} a_{bi'} a^\dagger_{cj'} a_{dj'} + \dots \tag{2.60}$$

$$\Downarrow$$

$$H(a^*, a) = \big(B^{i'}_{\alpha} X^{\alpha i'}_{ab}\big) a^*_{ai'} a_{bi'} + \big(J^{i'j'}_{\alpha\beta} X^{\alpha i'}_{ab} X^{\beta j'}_{cd}\big) a^*_{ai'} a_{bi'} a^*_{cj'} a_{dj'} + \dots \tag{2.61}$$

The first step transforms the Hamiltonian to SB representation, while the second step computes the Weyl symbol. Importantly, for traceless operators X, the Weyl symbol has no quantum corrections so one can simply "remove the hats" from operators. This can be seen by writing the Bopp representation to compute the Weyl symbol:

$$\Big(X_\alpha\Big)_W = \Big(a^*_i - \frac{i}{2}\frac{\partial}{\partial a_i}\Big) X_{ij} a_j = a^*_i X_{ij} a_j - \frac{i}{2}\delta_{ij} X_{ij} \tag{2.62}$$

with $\delta_{ij} X_{ij} = \mathrm{Tr}\big[X_{ij}\big] = 0$.

Time evolution of the Wigner function W(x) is computed using the TWA: the Weyl symbol of the commutator for Heisenberg evolution is truncated at first order

$$i\partial_t \rho = [H, \rho] \quad \Rightarrow \quad \partial_t W(a^*, a) = \big([H, \rho]\big)_W = H(a^*, a) \sin(\Lambda) W(a^*, a) \approx \big\{H, W\big\} \tag{2.63}$$

where Λ is the Moyal bracket which inherits the group structure of the commutator. As in the operator cTWA case, the time dynamics of the Wigner function may be solved via the method of characteristics, independently evolving many

individual points in phase space, then re-summing to compute expectation values of observables. In this case, the time evolution of a point $\vec{a}$ is defined by the Gross-Pitaevskii equations of motion

$$i\frac{\partial a_{a,i'}}{\partial t} = \frac{\partial H_w}{\partial a^*_{a,i'}}. \tag{2.64}$$

Observe that for a bilinear (eg strictly local) Hamiltonian, this equation looks the same as Schrödinger equation evolution of wave functions

$$i\frac{\partial a_a}{\partial t} = \frac{\partial}{\partial a^*_a}\Big(H_{ij}a^*_i a_j\Big) = H_{aj}a_j \quad \Leftrightarrow \quad i\partial_t|\psi\rangle = H|\psi\rangle. \tag{2.65}$$

This means that, in analogy to time evolution of points in operator phase space being product state operators between clusters, time evolution is that of **wavefunctions** constrained to be product states between clusters. Thus, Gross-Pitaevskii equations of motion may be equivalently be written as

$$i\partial_t|\psi\rangle = H|\psi \quad \text{subject to the constraint} \quad |\psi(t)\rangle = \bigotimes_{i'}|\psi_i(t)\rangle. \tag{2.66}$$

Gaussian Wigner functions for SB

The last part of the recipe is computing the Wigner function for these SBs. Without loss of generality, let us find the initial condition for the spin-polarized state for a system of N qubits: the wavefunction of this state is $(1, 0, 0, \ldots, 0)$ in the logical basis and thus there is one boson in the zeroth mode, and vacuum fluctuations on all other modes. Any other state can be found via an appropriate basis rotation. The "official" Wigner function of this distribution is the Wigner function of a Fock state product vacuum state

$$W(\vec{a}) \approx L_1(4|a_0|^2) \prod_i e^{-2|a_i|^2}. \tag{2.67}$$

This "official" Wigner function has two complications. One, it is not positive-definite, which means that one gains the sign problem for an extensive number of clusters, and there is the general ambiguity of negative probabilities. The second complication is that there are are size $\frac{1}{2}$ vacuum fluctuations on all $\mathcal{D}-1$ modes. The variance of expectation values of observables in phase space goes as the counting error; for example, for the Z magnitization per site , the observable is $Z_{ab} = \text{DIAG}[\pm 1, \pm 1, \cdots \pm 1]$ and thus variance of the function goes as $\frac{1}{2}\sqrt{\mathcal{D}-1}$, growing exponentially in cluster size. This requires the number of sampled phase points to also be exponential in cluster size, which is unfeasible.

Instead, let us take the approach of (Davidson and Polkovnikov, 2015) and similar to cTWA of above. Here, we approximate the Wigner function as a multivariate Gaussian of some width centered around some mean-field point. This means no matter the width of the Gaussian, one always reproduces all single-site observables. The width of the Gaussian distribution is given by matching the variance of operators in phase space to the symmetric quantum correlator, eg the quantum variance. In the limit of this width going to zero, we regain mean field evolution. This is exactly the same method for matching as cTWA. The Wigner function and constraints becomes:

$$W(\mu) = \frac{1}{\sqrt{|\sigma|}} e^{(\vec{\mu}-\vec{\mu}_0)^* \sigma (\vec{\mu}-\vec{\mu}_0)} \tag{2.68}$$

$$\langle X_i \rangle = \int d\mu W(\vec{\mu}) \mu_a^* \mu_b X_{ab}^i \quad ; \quad \langle \{X^i, Y^j\} \rangle = \int d\mu W(\vec{\mu}) \mu_a^* \mu_b \mu_c^* \mu_d X_{ab}^i Y_{cd}^j \tag{2.69}$$

For the Z-polarized state, the variance is diagonal, with a width of:

$$\Delta = \frac{-1+\sqrt{1+\mathcal{D}}}{\mathcal{D}} \quad ; \quad \vec{\mu}_0 = (1, 0, \ldots, 0) \tag{2.70}$$

This means that fluctuations (of the coefficients of the wavefunction) are exponentially suppressed in the system size. This makes sense conceptually from the perspective of counting error; for a local observable, there are order $\mathcal{D}$ uncorrelated terms, which means the variance will grow as $\sqrt{\mathcal{D}}$. In order to make the phase space variance one, one would then naturally have each variables' fluctuations correspondingly smaller, as is the case above.

It should be noted that it is impossible to match all moments of the distribution with a Gaussian. For example the Z-polarized state will always have the phase space variance of a Z expectation value, even though quantum mechanically one reads (+) with certainty. Furthermore, the normalization of the effective wavefunction, eg expectation value of the identity, now grows exponentially in the cluster size due to the fluctuations, as $\approx 1 + \mathcal{D}^{1/4}$. However, if we restrict ourselves to traceless observables (eg spin matrices), this has no impact on dynamics, as the identity trivially commutes with the Hamiltonian.

Example, revisited: SB cTWA for four coupled spins

The same example system as shown above can also be done under wavefunction (Schwinger Boson) cTWA.

1. First, define the 15+1 basis operators for each of the two clusters in the same fashion as the operator cluster TWA example. Define these operators as 15 4x4 matrices $X_\alpha \to T_\alpha^{ab} a_a^\dagger a_b$ with complex coordinates for (L/R) of $((a, a^*)\ /\ (b, b^*))$. For example, the operators:

$$X_4^L = I^{(1)} \otimes \sigma_x^{(2)} \;\; \rightarrow \;\; \begin{bmatrix} a_0^\dagger \\ a_1^\dagger \\ a_2^\dagger \\ a_3^\dagger \end{bmatrix}^T \begin{bmatrix} 0 & 1 & 0 & 0 \\ 1 & 0 & 0 & 0 \\ 0 & 0 & 0 & 1 \\ 0 & 0 & 1 & 0 \end{bmatrix} \begin{bmatrix} a_0 \\ a_1 \\ a_2 \\ a_3 \end{bmatrix}, \tag{2.71}$$

$$X_8^L = \sigma_x^{(1)} \otimes \sigma_y^{(2)} \;\; \rightarrow \;\; \begin{bmatrix} a_0^\dagger \\ a_1^\dagger \\ a_2^\dagger \\ a_3^\dagger \end{bmatrix}^T \begin{bmatrix} 0 & 0 & 0 & -i \\ 0 & 0 & i & 0 \\ 0 & -i & 0 & 0 \\ i & 0 & 0 & 0 \end{bmatrix} \begin{bmatrix} a_0 \\ a_1 \\ a_2 \\ a_3 \end{bmatrix}.$$

The classical Hamiltonian H_W becomes

$$H_W(a,b) = (a_i^* a_j + b_i^* b_j)\big(JT_{15}^{ij} + h_x T_3^{ij} + h_x T_4^{ij}\big) + J\, a_i^* a_j b_k^* b_l\, T_6^{ij} T_3^{kl}. \tag{2.72}$$

2. Draw initial conditions for $(\vec{a}, \vec{b})$. For the state $|\uparrow\downarrow\uparrow\downarrow\rangle$ the initial condition is $|\uparrow\downarrow\rangle$ per cluster corresponds to $a_1, b_1 = \sqrt{1+\delta_0}$ and a_q, b_q with $q = 0, 2, 3$ random numbers drawn from the Gaussian probability distribution (2.68) with zero mean and the variance $\delta_0 = \frac{\sqrt{1+2^2}-1}{2^2} \approx 0.30902$. Note that because the initial state here is $|\uparrow\downarrow\rangle$ and not $|\uparrow\uparrow\rangle$, it is the Schwinger bosons a_1, b_1 and not a_0, b_0, which are special. Similarly for $|\downarrow\uparrow\rangle$ ($|\downarrow\downarrow\rangle$) states the bosons a_2, b_2 (a_3, b_3) will be special.

3. Evolve each point $(\vec{a}(t), \vec{b}(t))$ via Gross-Pitaevskii equations (2.64), which explicitly read:

$$\begin{aligned} i\frac{\partial}{\partial t}\begin{bmatrix} a_0 \\ a_1 \\ a_2 \\ a_3 \end{bmatrix} &= \begin{bmatrix} J & h & h & 0 \\ h & -J & 0 & h \\ h & 0 & -J & h \\ 0 & h & h & J \end{bmatrix} \begin{bmatrix} a_0 \\ a_1 \\ a_2 \\ a_3 \end{bmatrix} \\ &+ J(|b_0|^2 + |b_1|^2 - |b_2|^2 - |b_3|^2) \begin{bmatrix} a_0 \\ -a_1 \\ a_2 \\ -a_3 \end{bmatrix} \end{aligned} \tag{2.73}$$

and similarly for the b-bosons.

4. One can compute expectation values of observables by averaging the corresponding Weyl symbols computed on time-dependent phase space points over the initial conditions. For example:

$$\begin{aligned} \langle \sigma_z^1(t)\sigma_z^2(t)\rangle &\approx \overline{a_a^* a_b} T_{15}^{ab}, \\ \langle \sigma_z^2(t)\sigma_z^3(t)\rangle &\approx \overline{a_a^* a_b b_x^* b_y} T_6^{ab} T_3^{xy}, \\ \langle \sigma_z^1(t)\rangle &\approx \overline{a_a^* a_b} T_3^{ab}. \end{aligned} \tag{2.74}$$

The results of the simulations of the Schwinger boson cTWA are shown in Fig. (2·4) using dashed lines. They are almost indistinguishable from the operator cTWA results.

Chapter 3

The cluster truncated Wigner approximation: models

This chapter will detail several models for which the cTWA is applied. This will include 1d many body localization (MBL), which shows long-time quantum behavior; diffusion and high-temperature thermal dynamics, which combines both short-time quantum and long-time hydrodynamic behavior; 1d Ising models, which demonstrates rapid decay to thermal equilibrium; and a study of Loschmidt echoes and out of time order correlation functions (OTOC), which is a measure of quantum and classical chaos.

3.1 1d many body localization

One system with which to demonstrate the cTWA is the 1d Heisenberg model with evenly distributed disorder in the z-component of the magnetic field and periodic boundary conditions

$$H = J \sum_{\langle ij \rangle} \left(\sigma_x^i \sigma_x^j + \sigma_y^i \sigma_y^j + \sigma_z^i \sigma_z^j \right) + h_z \sum_{i=1}^{N} \delta^i \sigma_z^i, \tag{3.1}$$

where $\delta^i \in [-1, 1]$. It is well known phenomenologically that this model undergoes a transition to the Many Body Localized (MBL) phase (Luitz et al., 2015) above some critical disorder strength $h_z \approx 3.5$. This phase is characterized, amongst other things, by a "memory" of initial conditions which persists indefinitely, as

well as a logarithmic growth of entanglement in time after a quench (Abanin et al., 2019). A natural order parameter to measure the transition to MBL is the staggered z-magnetization M_z (Luitz et al., 2015; Leviatan et al., 2017), which is maximal at $t = 0$ for a Neel initial state $|\psi_0\rangle$:

$$|\psi(0)\rangle = |\ldots\uparrow\downarrow\uparrow\downarrow\uparrow\downarrow\ldots\rangle \quad ; \quad M_z = \sum_{i=1}^{N}(-1)^i\sigma_z^i. \tag{3.2}$$

If the system thermalizes then this order parameter decays to zero, while in the MBL non-thermal regime it decays to some non-zero value.

Because averaging over disorder and quantum fluctuations are commuting operations one can simultaneously update initial conditions according to the Wigner function and the disorder realization of the Hamiltonian. This allows one to improve numerical convergence of the results and parallelize computations if necessary.

Fig. 3·1 plots the normalized staggered magnetization

$$m_z = \frac{1}{N}\langle\psi(t)|M_z|\psi(t)\rangle,$$

for the initial Neel state and different strengths of disorder. The left two plots show the results of the operator cTWA and the right plots show wave function (Schwinger Boson) cTWA. Both methods clearly lead to nearly identical curves. On the top two plots we show results for a relatively small system size $N = 16$, which allows for comparison with exact diagonalization. The bottom plots show cTWA results for a larger system size $N = 64$.

At short times, cTWA reproduces very well exact quantum dynamics. Accuracy of cTWA clearly improves with the cluster size. cTWA works well both at low disorder and at high disorder, but it clearly fails to reproduce localization at

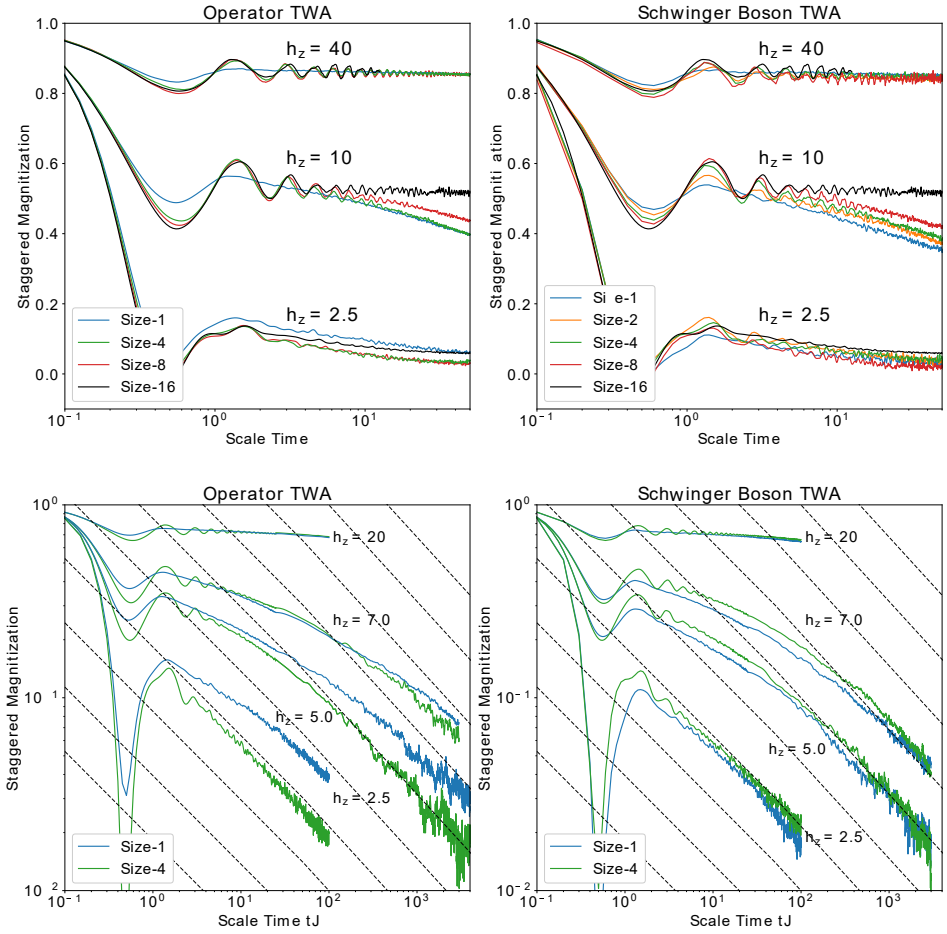

Figure 3·1: Dynamics of the staggered magnetization in the 1d Disordered Heisenberg Chain. TOP: Comparison of exact dynamics vs operator cTWA (left) and Schwinger Boson cTWA (Right) for varying cluster sizes and a 16-site Heisenberg chain (see text for details). BOTTOM: long time decay of the staggered magnetization within the cluster cTWA (Left) and Schwinger Boson cTWA (Right) for a 64-site 1d Heisenberg chain. Straight lines show $1/\sqrt{t}$ diffusive asymptotes of the decay.

intermediate values of disorder. This is consistent with earlier work (Oganesyan et al., 2009; Acevedo et al., 2017) observing that classical disordered spin chains in the thermodynamic limit eventually show ergodic diffusive behavior. These numerical results (bottom plots) indeed indicate that irrespective of the cluster size long time dynamics with cTWA approximation is always diffusive. Nevertheless cTWA indicates a presence of the MBL regime showing a longer and longer localized prethermalization plateaus with the increasing cluster size.

This example illustrates limitations of cTWA to correctly capture long time non-ergodic behavior. We believe that this is not a fundamental limitation though and even in this case cTWA can be improved by choosing a better operator basis, for example using not cluster operators constructed from Pauli matrices but from so called l-bits (Kulshreshtha et al., 2018), which also form a complete operator basis or using the basis of the matrix product operators. (Pirvu et al., 2010). These ideas will be further discussed in chapter 4.

Exponential timescales

When analyzing this imbalance behavior for different disorder strengths, it was found that the long-time behavior is universal. At very long times, the staggered magnetization (or equivalently ZZ correlation function) decays as $\sim t^{-1/2}$, consistent with diffusion with a very large diffusion exponent (see section 3.2 for more details on diffusion). However, at earlier times for larger disorder strength, the imbalance may persist close to one, eg some "nonthermal" state. It was found that by rescaling the time $t \to \lambda t$ for some scaling λ as a function of disorder Δ, one can match the long-time behavior at lower disorder to the longer time behavior at higher disorder. This scaling is best seen in Fig. 3·2 Left, where the scaling λ is computed for various values of disorder to make the time traces best overlap.

This universality means that the long-time dynamics for very large disorder can be implicitly computed by using the equivalent dynamics at shorter times.

Because at any disorder the imbalance eventually decays diffusively as $\sim t^{-1/2}$, the time scale to reach some small value is analogous to computing a diffusion constant for the system; at long times the imbalance goes as $\mathcal{I}(t) = (Dt)^{-1/2}$ (See section 3.2 for details on diffusion). Thus, one may compute the diffusion constant by computing the time it takes to decay to, say, 0.1:

$$D = \frac{100}{t_{0.1}}. \tag{3.3}$$

As is shown in Fig. 3·2, this timescale is exponentially large in the disorder strength, and thus the diffusion exponent is exponentially small. This is an indicator of glassy classical dynamics.

More important is the behavior of the diffusion exponent as a function of cluster size. As discussed in section 3.2, the diffusion constant converging as a function of cluster size is an indicator that the quantum thermal behavior is well described by the analogous classical dynamics. However, as can be clearly seen from Fig. 3·2 right, as the cluster size increases, so too does the decay time scale and thus the diffusion constant becomes smaller (by orders of magnitude at large disorder). This indicates that the effective classical dynamics has not converged, and in fact is consistent with a strict MBL phase where past some critical disorder strength the diffusion constant is exactly zero.

3.2 1d diffusion: XXZ and spin ladders

Thermalization of quantum systems has recently become a focus of active research both theoretical and experimental (Kaufman et al., 2016; Neill et al., 2016; Gogolin and Eisert, 2016; Borgonovi et al., 2016). It has been realized that quan-

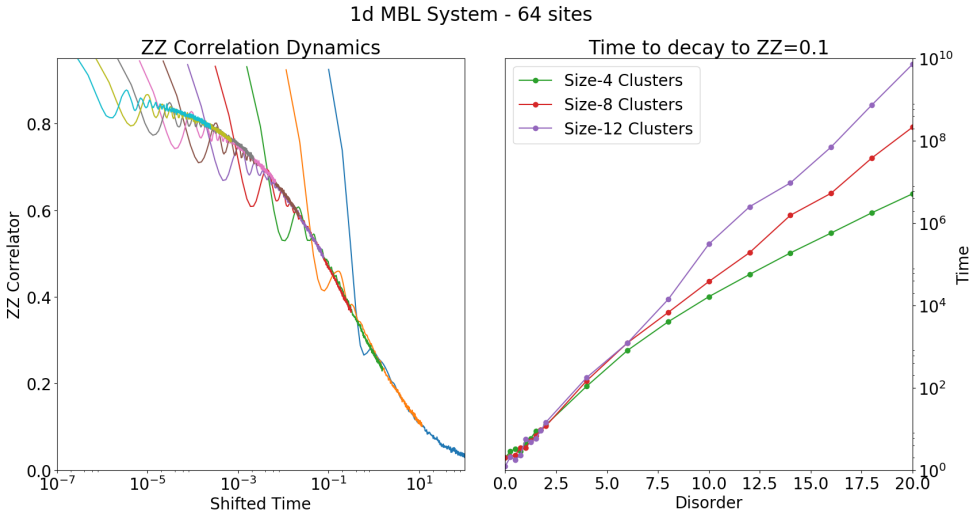

Figure 3·2: Exponential timescales for a 1d MBL system. LEFT: Imbalance dynamics for size-4 clusters and 64 sites, and disorder strength ranging from 2 to 20, with times of each disorder scaled to match $t \to \lambda t$. Clearly, the long-time decay is universal, as is indicated by the overlap of different observable traces shifted by some λ. Right computes the time scale for the imbalance to reach 0.1. For small disorder, this is computed exactly, while for large disorder it is extrapolated based on the universal long-time behavior.

tum chaos and emerging relaxation to equilibrium is encoded in the structure of many-body eigenstates of generic quantum Hamiltonians (Santos and Rigol, 2010; Polkovnikov et al., 2011; D'Alessio et al., 2016). Despite this progress most theoretical studies of quantum thermalization is either confined to small systems amenable to exact diagonalization (Mukerjee et al., 2006; Steinigeweg et al., 2014; Agarwal et al., 2015; Richter et al., 2018) or to more phenomenological hydrodynamic and kinetic approaches (Moeckel and Kehrein, 2008; Lux et al., 2014; Ljubotina et al., 2017; De Nardis et al., 2019).

Microscopically, hydrodynamic coefficients can be expressed through appropriate non-equal time correlation functions. In equilibrium there are various thermodynamic relations between transport and response coefficients such as fluctuation-dissipation relation (Landau and Lifshitz, 2013), drift-diffusion Einstein and Onsager relations (Onsager, 1931) and others. These thermodynamic identities imply that a proper formalism describing thermalization should not only explain relaxation of various observables to their thermal values but also proper asymptotic behavior of non-equal time correlation functions and the dynamic structure factor $S(k, \omega)$.

Using phase space methods as discussed in previous chapters, we study $S(k, \omega)$ for spin 1/2 next-nearest-neighbor XXZ chains and XY ladders at infinite temperature. In particular, we correctly recover both its high and low frequency asymptotics: low frequencies corresponding to hydrodynamic diffusive relaxation, while high frequencies describe short time coherent quantum excitations. These methods smoothly interpolate between the two asymptotic regimes. While high frequency behavior can be obtained using exact diagonalization in relatively small systems, the correct description of low frequencies for such interacting thermal models requires access to system sizes which are beyond the range of existing

methods. We also show that noise in initial conditions is crucial for correctly predicting the structure factor and the spin diffusion constant: cluster mean field dynamics, obtained from cTWA by suppressing noise, leads to incorrect predictions for subextensive cluster sizes.

To demonstrate how the method works we choose a particular next-nearest neighbor spin-1/2 XXZ model with periodic boundary conditions, which conserves the total Z magnetization but has no extensive symmetries.

$$H = \sum_{i}^{N} \sigma_x^i \sigma_x^{i+1} + \sigma_y^i \sigma_y^{i+1} + \Delta \sigma_z^i \sigma_z^{i+1} + \gamma \sum_{i}^{N} \sigma_x^i \sigma_x^{i+2} + \sigma_y^i \sigma_y^{i+2} + \Delta \sigma_z^i \sigma_z^{i+2}. \quad (3.4)$$

Here, σ represent Pauli matrices. We choose parameters $\Delta = 2$ and $\gamma = 1/2$; for $\gamma = 0$ the model is integrable but still exhibits diffusive behavior (Prosen, 2011b; Karrasch et al., 2014; De Nardis et al., 2018).

In Fig. 3·3 we show the two-time spin-spin correlations $\mathrm{Tr}\left[\sigma_\alpha^i(t)\sigma_\alpha^i(t')\right]/\mathcal{D}$ for $\alpha \in \{x, y, z\}$ as a function of t at different t', initialized in the randomly polarized Z states at $t = 0$. In Fig. 3·3A we use a system size $N = 16$ allowing us to benchmark cTWA with simple exact results: it is clear that dynamics are almost indistinguishable. This behavior persists at all offsets t' as shown in Fig. 3·3B, and is symmetric about $|t - t'|$ as is expected. The mean-field result (colored dashed lines) does not generally reproduce the correlator, emphasizing that the initial noise is critical for the formalism. This time translation invariance is highly nontrivial, as traditional TWA methods usually break down at long times due to divergent ultra-violet noise in the system leading to spurious long time vacuum heating (Blakie et al., 2008). On the contrary, within cTWA quantum noise introduced by the initial Wigner function has a correct scaling with increasing cluster size (See chapter 2 for more details), and persists as a function of time:

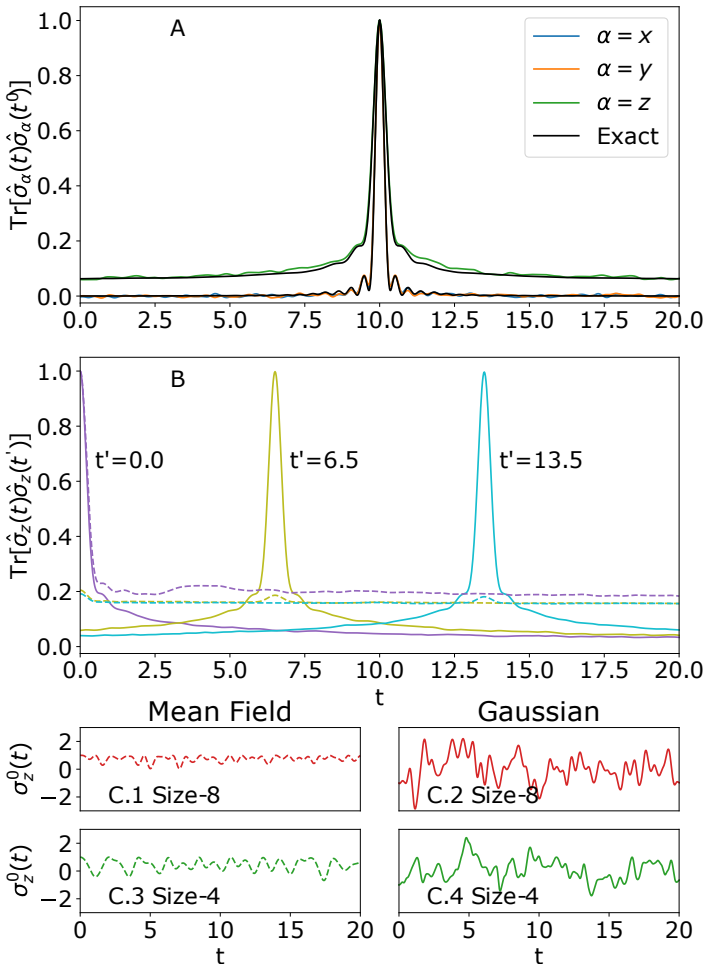

Figure 3·3: Non-equal time spin-spin correlation functions of the next-nearest neighbor XXZ chain of eq. 3.4 at infinite temperature. **(A)** Correlation function for $t' = 10$, compared to exact results. $(L, N) = (8, 16)$ **(B)** Correlation function for $(L, N) = (8, 64)$, which shows that the correlation function is well captured for offsets t'. Mean field (dashed) does not capture correctly, emphasizing importance of fluctuations. **(C)** Time traces of individual points in phase space for a typical (dashed) mean-field and (solid) Gaussian initial conditions. Fluctuations persist at all times for Gaussian, but are exponentially small in the cluster size for the mean-field case. Cluster and system sizes are $(L, N) = (8, 64)$.

each point in phase space is generically non-stationary, as is seen in Figs. 3·3 C.2 and 3·3 C.4. This, too, is nontrivial, as initial conditions inject an amount of noise exponential in the cluster size L: each point is on average a distance $2^{L/2}$ from the mean. This is matched by the exponential size of the phase space $\sim 4^L$. For mean-field the noise is only from thermal fluctuations; in particular it is equal to zero for each initial spin configuration. In turn in generic ergodic systems such meanfield trajectories lead to relaxation of local observables to near constant (thermal) values with exponentially small fluctuations (D'Alessio et al., 2016) (see Fig. 3·3C.1,3).

We point that while the $\sigma_x\sigma_x$ and $\sigma_y\sigma_y$ time correlations decay to zero, the $\sigma_z\sigma_z$ correlation functions decay to a non-zero constant scaling as the inverse system size: $\mathrm{Tr}\left[\sigma_z^i(t)\sigma_z^i(t')\right]/\mathcal{D} \to 1/N$ for $|t-t'| \to \infty$. This result follows from conservation of the total z magnetization: for a typical random initial state the magnetization scales as $\sqrt{N}$ such that the average magnetization per spin is $1/\sqrt{N}$. Within mean field different clusters cannot exchange Z-magnetization thus the spin-spin correlation spuriously relaxes to a higher constant $1/L$ instead of $1/N$, as is seen in Fig. 3·3B.

Diffusion of conserved quantities at $\beta = 0$ can be found using the symmetric correlator (Steinigeweg and Brenig, 2011; Luitz and Lev, 2017; Bar Lev et al., 2015), where instead of the particle number we use the (conserved) Z-magnetization

$$C_{ij}(t) = \frac{1}{\mathcal{D}}\mathrm{Tr}[\sigma_z^i(t)\sigma_z^j(0)]. \tag{3.5}$$

For diffusive systems this correlator should be well approximated by a Gaussian whose width grows in time as $\sqrt{Dt}$, where D is the diffusion constant. Therefore a natural way of extracting the diffusion constant is by computing the width of

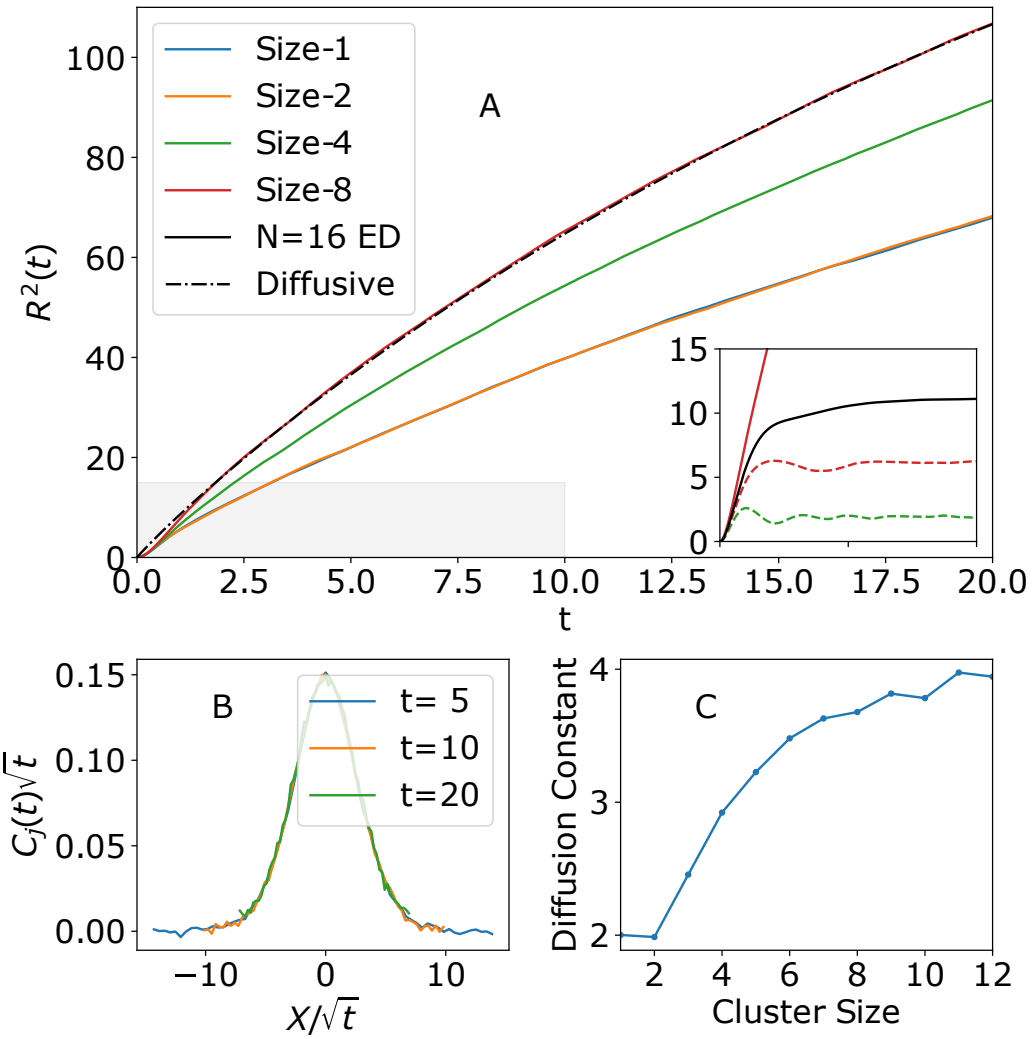

Figure 3·4: Diffusive Dynamics for next-nearest neighbor XXZ chain of eq. 3.4 at infinite temperature. **(A)** shows the conformal width of the correlation function defined by Eq. (3.6); Black dashed line is a single-parameter fit for classical diffusion of equation (3.7). Gray box and inset shows comparison of exact results for $N = 16$ (solid black line) with cTWA (red solid line) and mean field (dashed lines) simulations for a larger system $N = 64$. **(B)** shows scaled values of C_{ij} for size-8 clusters, averaged over offsets, which takes the form of a Gaussian. **(C)** is a fit of the diffusion constant as a function of cluster size for $N \approx 64$.

this correlation as a function of time

$$R^2(t) \;=\; \frac{\sum_{ij} \frac{N^2}{\pi^2} \sin^2\left(\frac{\pi}{N}(i-j)\right) C_{ij}(t)}{\sum_{ij} C_{ij}(t)} \tag{3.6}$$

and fitting it to the solution of the classical diffusion equation (See Appendix A.2 for derivation)

$$R^2(t) = \frac{N^2}{2\pi^2}\left(1 - e^{-4Dt\pi^2/N^2}\right). \tag{3.7}$$

Note that in finite periodic chains systems we find it more convenient to use this conformal distance between spins; in the limit $N \to \infty$ it recovers the typical Gaussian width as e.g. used in Ref. (Bar Lev et al., 2015).

In Fig. 3·4A we show results of numerical simulations of $R^2(t)$ for different cluster sizes and the total system size $N = 64$. Except for short times all the curves are well fit by the diffusion prediction (3.7) although with a cluster dependent diffusion constant, which saturates with increasing cluster size (Fig. 3·4C) to the asymptotic value $D \approx 3.75$. The inset shows the result of exact evolution for a smaller system size $N = 16$ (cTWA for the same system size will be nearly identical c.f. Fig. 3·3). It is clear that the system size $N = 16$ is insufficient to see diffusive behavior in this system. The panel (3·4B) shows the correlation function $C_{ij}(t)$ rescaled by $\sqrt{t}$ with a very good collapse to the expected Gaussian profile.

For size-1 clusters the Gaussian profile is expected, as the dynamics of the system is then identical to that of a classical spin chain, which is known to exhibit diffusive behavior over a wide range of parameters (Oganesyan et al., 2009; Das et al., 2018). However, for larger cluster sizes the emergent diffusive profile is somewhat non-trivial, as the classical phase space is much larger than the naive one, encoding many "quantum" correlations. Moreover, dependence of the

diffusion constant on the cluster size L (fig 3·4C) indicates that it is strongly renormalized by the underlying quantum fluctuations. As in Fig. 3·3 we see that the mean field dynamics (dashed lines in the insert of fig 3·4A) is not adequate for correctly capturing long-time diffusive behavior even for relatively large cluster sizes.

Having analyzed the diffusive spreading of correlations we now move on studying the dynamic structure factor $S(k,\omega)$ and its momentum average $S(\omega)$, containing more complete information about non-equal time spin-spin correlations:

$$\begin{aligned} S(k,\omega) &= \sum_{ij} \int_{-\infty}^{\infty} dt e^{i\omega t + ik(i-j)} C_{ij}(t), \qquad (3.8) \\ S(\omega) &= \frac{1}{N}\sum_{k} S(k,\omega) = \frac{2\pi}{N}\sum_{i} \int_{-\infty}^{\infty} dt e^{i\omega t} C_{ii}(t) \\ &= \frac{2\pi}{\mathcal{D}} \sum_{mm'} |\langle m'|\sigma_z|m\rangle|^2 \delta(\omega - E_m + E'_m). \end{aligned}$$

In finite size quantum systems (Sachdev, 2011) $S(\omega)$ strictly speaking consists of isolated δ-function peaks corresponding to discrete energy levels. However, as the number of states exponentially increases with the system size $S(\omega)$ effectively becomes continuous if we introduce a tiny damping factor into the time integral. We also comment that $S(k=0,\omega=0)$ diverges due to conservation of the total spin σ_z, but this divergence does not play a role at finite frequencies.

Figure 3·5A shows the time correlations at the same site, which, after short time quantum behavior, decays diffusively as $1/\sqrt{t}$ before saturating at $1/N$. Figure 3·5B shows $S(\omega)$, which is the Fourier transform of 3·5A. It shows that at high frequencies the structure factor $S(\omega)$ agrees well with exact diagonalization predictions; the exponential decay as seen here is expected on general grounds (D'Alessio et al., 2016). However, the simple exact diagonalization calculation

fails to capture the small frequency diffusive asymptote of the structure factor $S(\omega) \propto 1/\sqrt{\omega}$ (Luitz and Bar Lev, 2016) due to small system sizes: there is a saturation for $S(\omega < t_c^{-1}) = t_c^{1/2}$, where $t_c \sim N^2$ is the Thouless time (Edwards and Thouless, 1972). Conversely cTWA clearly reproduces this asymptote because one can access much larger system sizes. At intermediate frequencies, there is a smooth link between the quantum and classical behaviors, allowing for a correct behavior at all ω. Figures 3·5C.1-6 show the dynamic structure factor $S(k, \omega)$ for the first few wavenumbers k. Small k represent long length scales where hydrodynamic behavior should dominate. As wavelength increases, diffusive behavior becomes sensitive to the finite system size, seen as the low-frequency asymptote in both quantum and effective classical dynamics (C.4-6). However, for larger frequencies the cTWA remains sensitive to smaller length scale effects, with a generic exponential decay in frequency diverging from the $1/\omega^2$ of classical hydrodynamics. Non-generic behavior in this regime should be well-captured simply by ED or equivalently intra-cluster dynamics.

The integrable XXZ model

A similar model which shows diffusion despite being integrable is the XXZ model (Gaudin, 2014), which is described by equation 3.4 for $\gamma = 0$ and $|\Delta| > 1$. The various behaviors of this model have been well studied. Particularly: for $\Delta = 0$ it is the XY model, with a mapping to free fermions. for $|\Delta| < 1$ the model is ballistic, and at $\Delta = 1$ it is the Heisenberg model, with super-diffusive behavior (Ljubotina et al., 2017) with exponent $t^{-2/3}$. For $|\Delta| > 1$ the model is diffusive.

This diffusive behavior has been well-studied, especially within three contexts: boundary wall quenches, (Ljubotina et al., 2017; Karrasch et al., 2014), non-equilibrium steady states (Prosen, 2011a; Prosen, 2011b), and more recently from

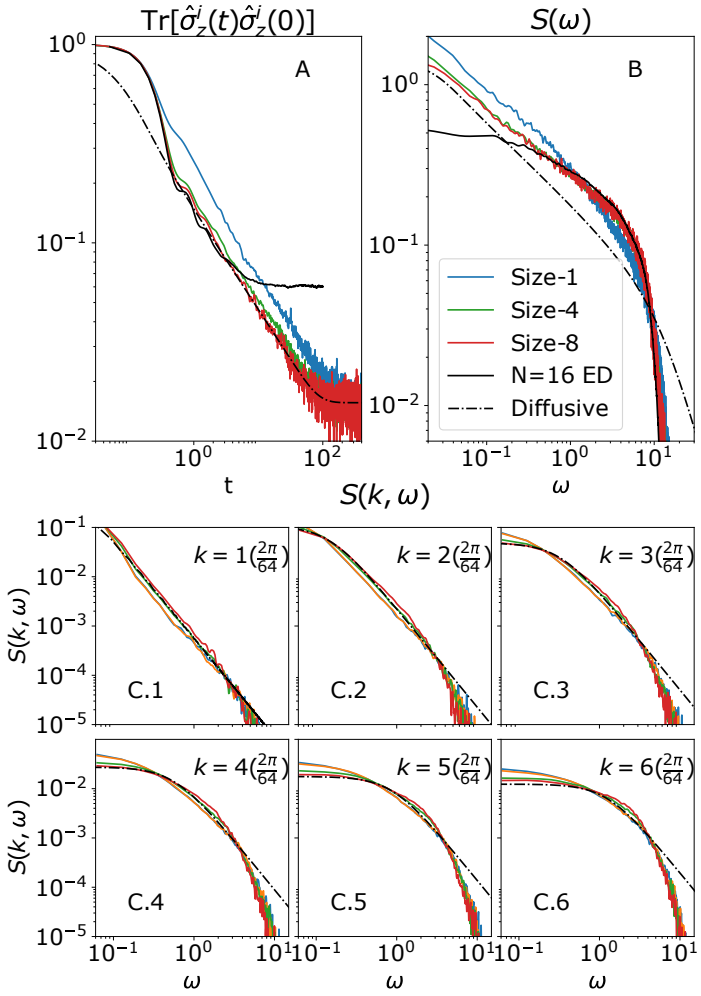

Figure 3·5: Dynamic Structure Factors of the Next-Nearest Neighbor XXZ chain of eq. 3.4 at infinite temperature. **(A)** Log-log version of Fig. 3·3A showing diffusive decay. **(B)** Momentum-averaged structure factor $S(\omega)$, which is the Fourier Transform of **(A)**. **(C.1-6)** Dynamic structure factor $S(k,\omega)$ for the first few k. The system size is $N = 64$; dashed black lines are for classical diffusion for $D = 3.75$

generalized hydrodynamics (GHD) (De Nardis et al., 2019; Gopalakrishnan et al., 2019). However, the diffusion constant derived from $S(k,\omega)$ does not necessarily need to match that of a quench: the former averages over equilibrium, while the latter studies particular special initial states. It is relatively simple to study both approaches within the cTWA.

Diffusion from $S(k,\omega)$: In Fig. 3·6 we plot the results of simulations on the 64-site XXZ chain derived from $S(k,\omega)$ and see behavior as expected. For $\Delta < 1$ the model is ballistic: fitting to diffusion does not make sense, although at late times the method will always show diffusive behavior. This is flagged by a non-convergence in cluster size: especially clear for $\Delta = 0$, where the "diffusion constant" fit diverges linearly with cluster size. However, for larger Δ the diffusion constant does relatively converge with cluster size; for $\Delta = 2$ we find $D \approx 1.2$, an increase of about 1.5 from "classical" size-1 clusters. We find that the diffusion constant scales as Δ^{-1} at large Δ. This finding is consistent with earlier work (Steinigeweg and Brenig, 2011) but potentially inconsistent with more recent work which predicts $D = 1/3\pi$ for $\Delta \to \infty$ (Gopalakrishnan and Vasseur, 2019) using GHD methods.

Diffusion from a Boundary wall: Instead of an infinite temperature state, we study the $\langle S_z(t)\rangle$ dynamics of a boundary quench from an initial pure state $|\psi\rangle = |\uparrow \ldots \uparrow\uparrow\downarrow\downarrow \ldots \downarrow\rangle$. Results are shown in Fig. 3·7. For $\Delta = 2$ we find rapid convergence with cluster size to $D \approx 0.56$, consistent with these previous works (Karrasch et al., 2014). For $\Delta < 1$ the "diffusion constant" diverges to a much larger (but still finite) value, consistent with non-diffusive behavior. This diffusive and non-diffusive behavior can be seen in the second two panels. We find

that the diffusion constant scales as $\Delta^{-1.5}$ at large Δ. As expected, the two derived diffusion constants differ– by a factor of ~ 2.1. This is not unexpected; the diffusion constant computed from $S(k,\omega)$ is averaging over an ensemble of typical infinite-temperature states, while the other evolves a single low-energy state. This suggests a temperature dependence of the diffusion constant. Unfortunately, results are inconclusive at the interesting $\Delta = 1$ point.

As emphasized previously, the power of cTWA lies in calculating the dynamic structure factors $S(k,\omega)$ at high temperatures. This is shown in Fig. 3·8 at a range of Δ. For $\Delta = 0$ (top left plot) there are clear indicators of ballistic behavior indicated by the linear dispersion relation, consistent with exact results for the XY model (not shown). For larger Δ the model becomes diffusive, with a more generic looking dynamic structure factor. However, this structure factor is fit very well by that of classical diffusion (black dashed) in this regime. In general, non-generic features will be confidently be reproduced for large frequencies and wavenumbers, representing small-scale coherent effects well captured by intra-cluster dynamics.

3.3 1d Ising model

This section presents the cTWA method as applied to the Ising model in a transverse and longitudinal field, which is known to have a quantum chaotic regime. Here, we consider the setup similar to that of (Leviatan et al., 2017) where we initially polarize a single spin in the up state and follow time decay of the magnetization. However, unlike Leviatan, we consider two setups of the "remaining" bath spins where i) they are prepared in a pure polarized state and ii) they are

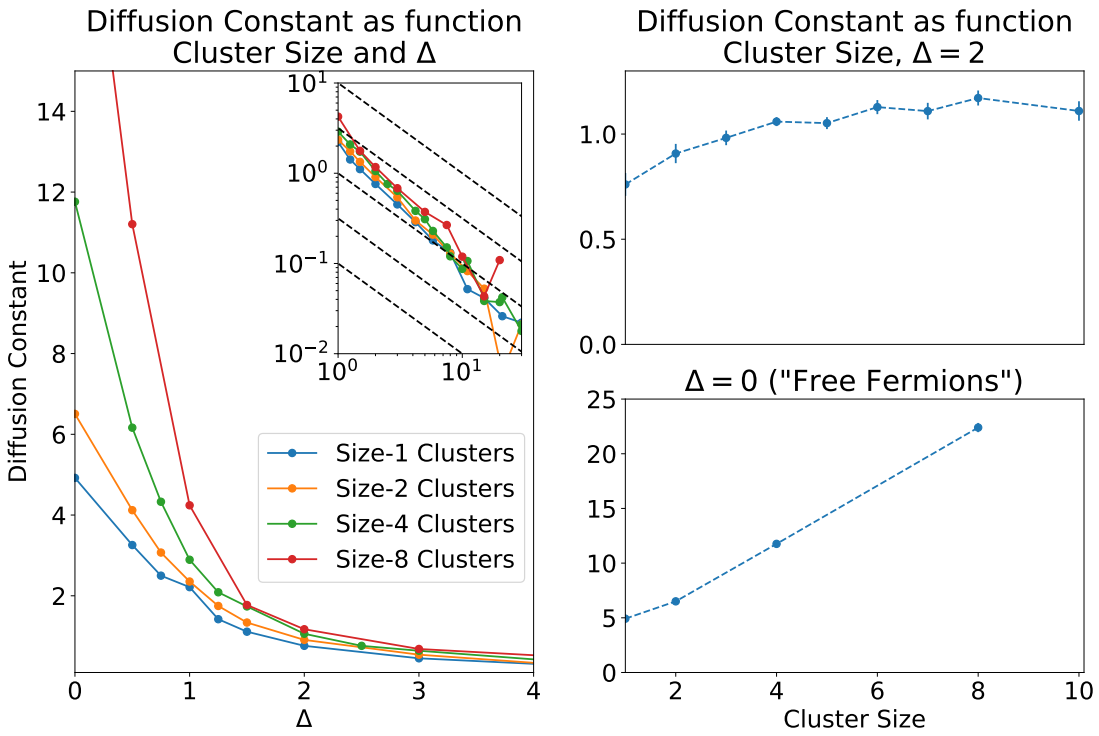

Figure 3·6: Diffusion Constant for the XXZ Model as derived from $S(k, \omega)$. Left: Diffusion Constant as function of anisotropy Δ and cluster size. Inset is log-log of the same, showing $1/\Delta$ consistent with previous results (Steinigeweg and Brenig, 2011). Clearly for $\Delta < 1$ the diffusion constant does not converge, as expected for ballistic behavior (Bottom right), while for $\Delta = 2$ it converges to about 1.5× its "classical" value (Top right).

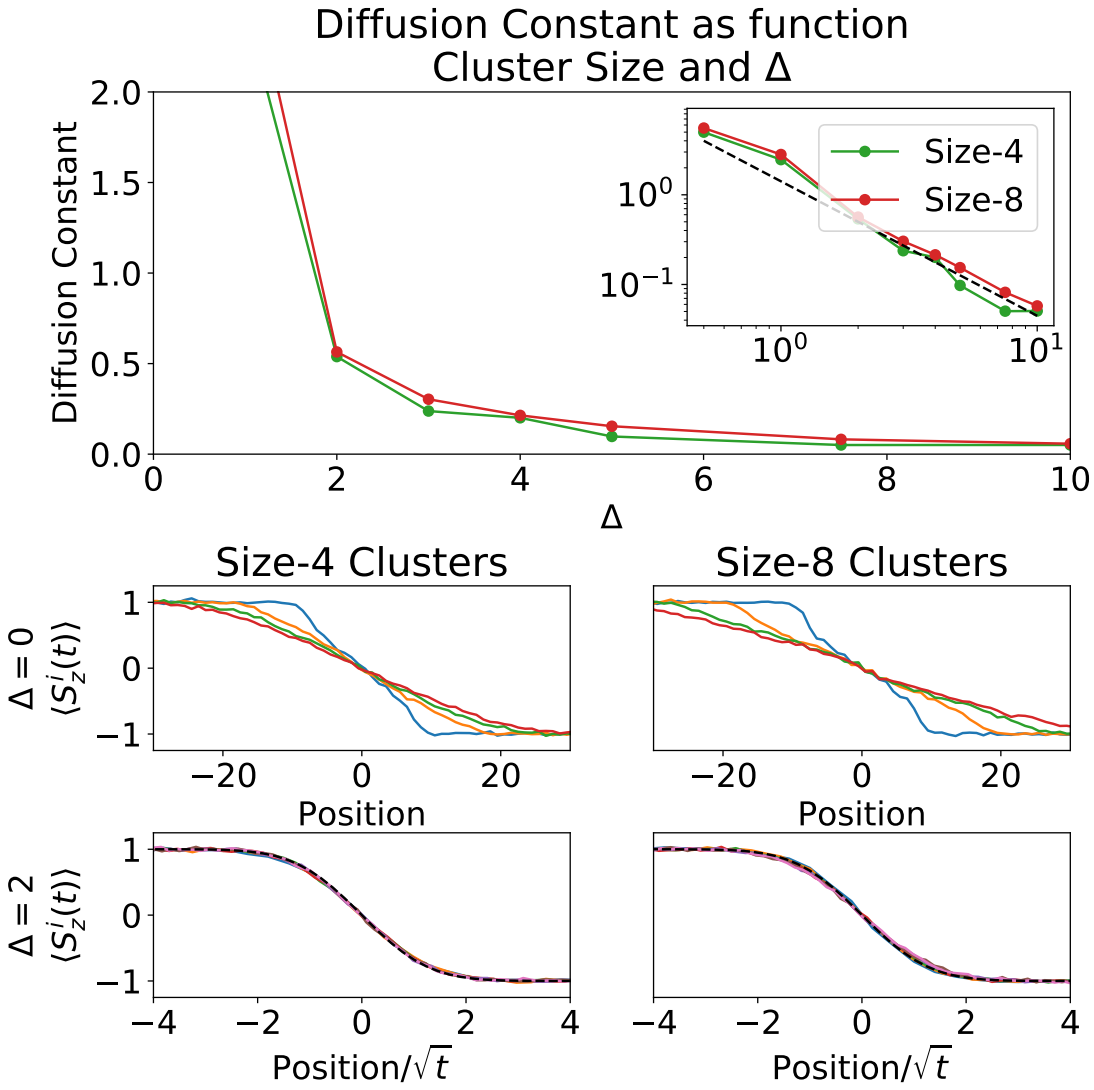

Figure 3·7: Diffusion Constant for the XXZ Model as derived from Boundary Wall initial condition. TOP: Diffusion constant as function of Δ. For $\Delta < 1$ the diffusion constant diverges, consistent with being non-diffusive. Inset is log-log of the same data; dashed line is of $\Delta^{-1.5}$.
MIDDLE: Spin profile for $\Delta = 0$, showing ballistic growth improving with cluster size. Lines are for times $[2.5, 5, 7.5, 10]$.
BOTTOM: Spin profile for $\Delta = 2$, renormalized by $\sqrt{t}$ showing diffusive collapse. Dashed line is classical profile for $D = 0.52$.

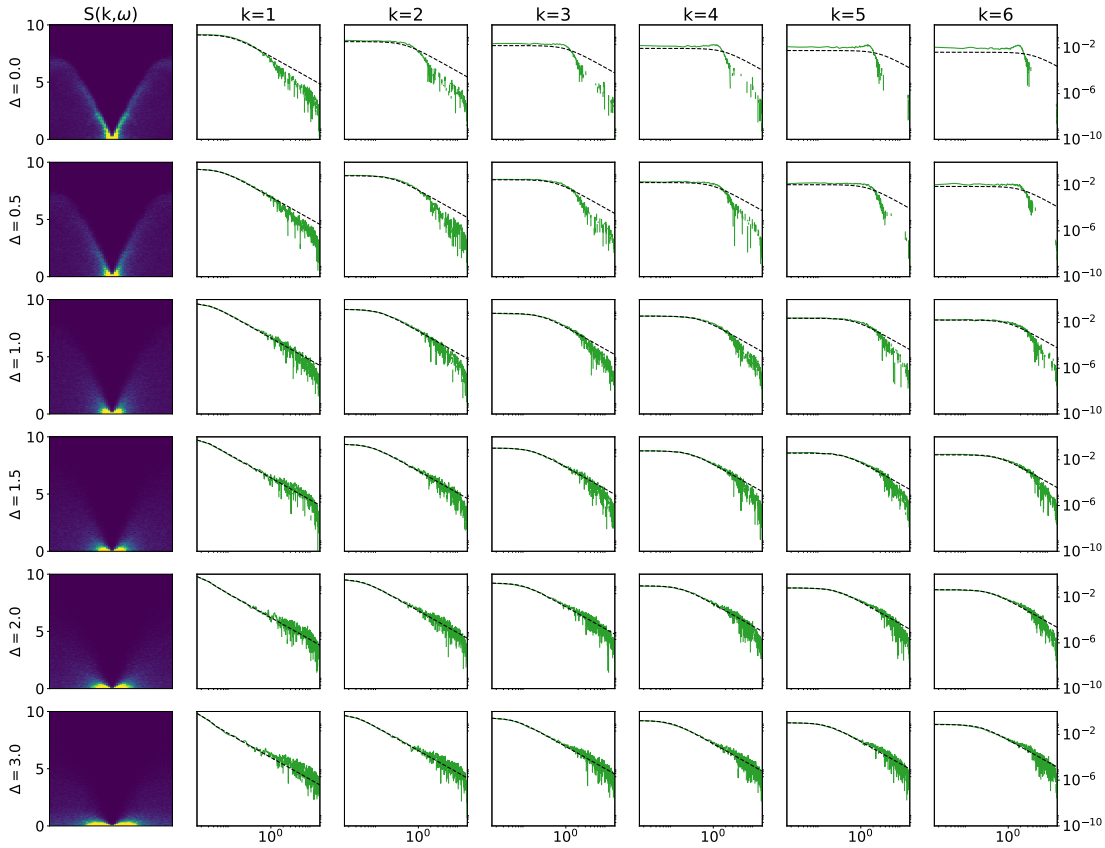

Figure 3·8: $S(k, \omega)$ **for a range of** Δ **for the XXZ Model and 64 sites.** Vertical is for various Δ (labeled on left). Left subplots are the full dynamical structure factor. Line plots are the first 6 momentum modes and size-4 clusters; Dashed lines are for classical diffusion with best-fit value from Fig. 3·6.

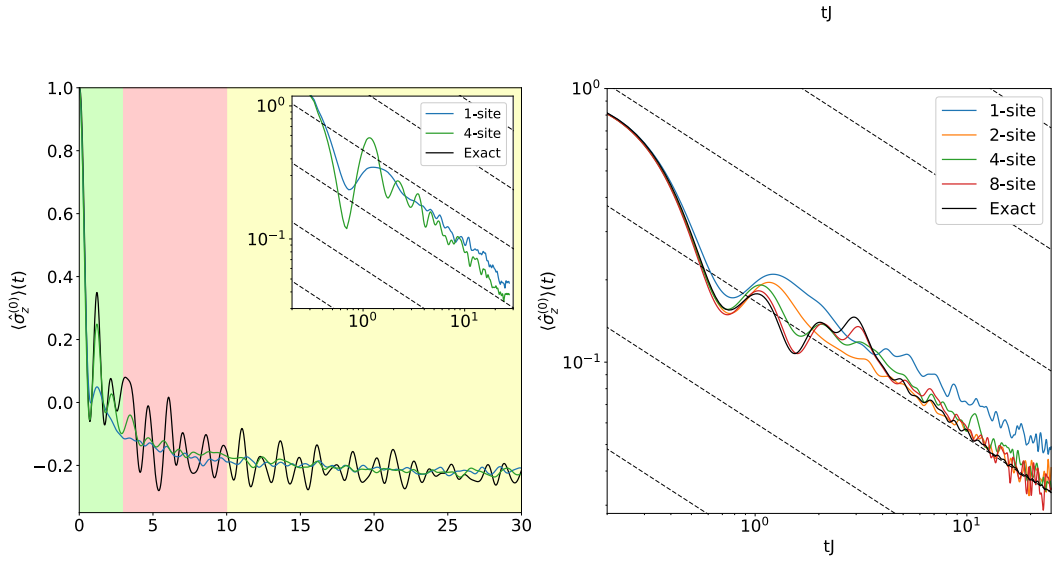

Figure 3·9: Magnetization decay in a spin chain. Time dependence of $\langle\sigma_z^0(t)\rangle$ of the initially polarized spin coupled to other spins forming a "bath". Left plot corresponds to the initial pure state $|\uparrow\downarrow\ldots\downarrow\rangle$.The right plot corresponds to the mixed, infinite temperature, state of the bath, where all spins except one are prepared in a random initial state. The system size is $N = 20$ for the pure state and $N = 16$ for the mixed state; the Hamiltonian of the system is given by Eq. (3.9). The inset in the left plot shows $\langle\sigma_z^0(t)\rangle - 1/N\sum_j\langle\sigma_z^j\rangle$. Both setups show initial coherent oscillations of the magnetization followed by long-time diffusive relaxation to the thermal state. The accuracy of the cTWA clearly improves with the cluster size. Dashed lines are $1/\sqrt{t}$ diffusive asymptotes.

prepared in a mixed state. We consider the Hamiltonian

$$H = \sum_{i=0}^{20} \sigma_x^i \sigma_x^{i+1} + 0.8090\sigma_x^i - 0.9045\sigma_z^i \tag{3.9}$$

with periodic boundary conditions. This set of couplings is known to lead to the chaotic Hamiltonian satisfying the eigenstate thermalization hypothesis (Kim et al., 2014). To benchmark our cTWA results we compare them to exact quantum dynamics for a system of 20 spins. For the pure state initial condition we choose $|\psi\rangle = |\uparrow\downarrow\downarrow\ldots\downarrow\rangle$, i.e. all spins except the first one are polarized along the

$-z$ direction. For the mixed state initial condition we uniformly sample all the bath spins from the Bloch sphere keeping always the first spin polarized along the positive z-axis. The latter setup is identical to the one studied in (Leviatan et al., 2017).

In Fig. 3·9 we show time dependence of the z-magnetization of the initially z-polarized spin for the pure state of the bath (top) and the mixed state of the bath (bottom). For the pure initial state the cTWA reproduces short-time coherent oscillations, as well as long-time diffusive decay and thermodynamic equilibrium. The only thing cTWA misses are the intermediate time oscillations of the magnetization; this mistake decreases for larger clusters. The agreement of cTWA with exact dynamics is even better for the mixed initial state of the bath.

While the accuracy of cTWA at short times can be generally expected as in standard TWA approximations, correctly capturing the long time dynamics is highly nontrivial as TWA often leads to an uncontrolled error (Polkovnikov, 2010). Intuitively this feature of cTWA is not that surprising as cluster variables correctly capture short-distance quantum correlations, while the long time/long distance dynamics is generally expected to be classical. At least for thermalizing, nonintegrable, systems cTWA is expected to predict accurately both short time and long time results with the increasing cluster size as seen in the figure (see also Ref. (Davidson et al., 2017), where similar long time accuracy of the fermionic TWA was observed).

Short time dynamics. Like the traditional TWA (see Ref. (Polkovnikov, 2010) for details) cTWA is asymptotically exact at short times, up to the order $\mathcal{O}(t^2)$. This is guaranteed by the short time perturbation theory for all observables. Specifically any short time response of an observable O can be Taylor expanded in time and can be captured under the Gaussian Wigner function. Similarly,

one may heuristically argue that dynamics are exact until entanglement between clusters, which is treated approximately, become relevant.

Long time dynamics. In cTWA we generically deal with classical nonlinear and hence chaotic systems. For linear systems cTWA is guaranteed to be exact at all times and the case of nonlinear integrable systems goes beyond the scope of this paper and requires a special attention. Then the long time steady state is expected to be described by the thermal equilibrium:

$$\langle O(t)\rangle_{t\to\infty} \to = Z^{-1}\int d\vec{x} e^{-\beta H_W(\{x\})} O_W(\{x\}), \tag{3.10}$$

where β is the temperature set by the initial energy of the system. At least for high temperatures this Gibbs distribution is equivalent to the quantum thermal distribution $\langle O\rangle = \mathrm{Tr}[Oe^{-\beta(E)H}]$. Moreover the long time approach to the thermal equilibrium, is usually described within the classical hydrodynamic framework and thus is compatible with cTWA. While we do not have more mathematically rigorous arguments of asymptotic equivalence of thermal classical (in terms of cluster variables) and quantum distributions, we observed that in all ergodic regimes as we increase the cluster size cTWA correctly predicts long time behavior of chaotic quantum systems.

Intermediate time dynamics. cTWA may miss intermediate time dynamics of the system, as illustrated in Fig. 3·9. The mistake is usually can be controlled by increasing the cluster size. For sufficiently large clusters the system might enter the classical hydrodynamic regime before the mistake due to the truncation of quantum dynamics kicks in. Then the cTWA becomes essentially exact at all times like it e.g. happens for the 8-site cTWA in the bottom plot of Fig. 3·9. This usually happens at high temperatures and away from integrability. Close to the ground state the coherent quantum dynamics is expected to persist for very long

times and as a result one needs to use very large clusters to capture dynamics correctly at long times.

3.4 Loschmidt Echoes and OTOC

The Loschmidt echo and out of time order correlators (OTOC) are tools of diagnosing quantum chaos in thermal systems (Sekino and Susskind, 2008; Jacquod and Petitjean, 2009). Generally speaking, they diagnose how small perturbations (say, to initial conditions) spread through the system in time. Given two operators X and Y, the OTOC is defined as

$$C(t) = \langle [X(t), Y(0)]^2 \rangle. \tag{3.11}$$

Observe that this requires evolution both forwards and backwards in time due to the commutator being squared, hence the name. With operator time evolution as a unitary rotation $U(t)$ such that $X(t) = U^\dagger(t)XU(t)$, there are terms such as

$$\langle \left[U^\dagger(t)XU(t)\right] Y \left[U^\dagger(t)XU(t)\right] Y \rangle \tag{3.12}$$

From left to right, the wavefunction would be evolved forwards in time, acted on by X, then evolved backwards to compute the expectation value with Y. This looks similar to seeing how two close-by trajectories diverge in time, a relation which will be made more explicit below.

Because the OTOC measures response to perturbations, it has been used as a tool for diagnosing chaos in quantum systems (Larkin and Ovchinnikov, 1969). It is well understood that a quantum system with a well-defined chaotic classical limit exhibit exponential growth of the OTOC (Sekino and Susskind, 2008), similar to that of the exponential sensitivity to perturbations for classically chaotic

systems.

It is then a natural question to ask how such quantum chaos extends to classical chaos when such semiclassical limits in phase space are not as clear. Inspired by recent work on OTOC applied to fermionic phase space (Schmitt et al., 2019) and computing butterfly velocities in classical 1d classical spin chains (Das et al., 2018), in this section we apply similar methods to cluster phase space.

Suppose some phase space given some group of operators and equivalent phase space. The first step towards computing OTOC is replacing commutators with Poisson brackets via their Weyl symbol:

$$\big(i[A,B]\big)_W = \{A(x), B(x)\} = f_{\alpha\beta\gamma} x_\gamma \frac{\partial A(x)}{\partial x_\alpha} \frac{\partial B(x)}{\partial x_\beta} \quad \text{for} \quad A(x) = \big(A\big)_W. \tag{3.13}$$

One might be expected to naively replace the square brackets under quantum OTOC with curley brackets for classical OTOC, but **this is only approximate**. This is clear to see if we compute the Weyl symbol of two basis operators:

$$\begin{aligned} [X_\alpha, X_\beta]^2 = \big(f_{\alpha\beta\gamma} X_\gamma\big)^2 = f_{\alpha\beta\gamma} f_{\alpha\beta\mu} X_\gamma X_\mu = f_{\alpha\beta\gamma} f_{\alpha\beta\mu} \Gamma_{\gamma\mu\nu} X_\nu \text{for} \\ \Gamma_{\gamma\mu\nu} = \mathrm{Tr}[X_\gamma X_\mu X_\nu]. \\ \{x_\alpha, x_\beta\}^2 = (f_\alpha \beta\gamma x_\gamma)^2 = f_{\alpha\beta\gamma} f_{\alpha\beta\mu} x_\gamma x_\mu. \end{aligned} \tag{3.14}$$

The statement here is that the Weyl symbol $\big(X_\gamma X_\mu\big)_W \neq x_\gamma x_\mu$ for two operators acting on the same cluster. However, for a Gaussian Wigner Function these moments are correctly reproduced (!) at least at $t = 0$ even on the same site. For operators acting on distant (adjacent) clusters, this is also correctly reproduced up to $\mathcal{O}(t^2)$ in accordance with perturbation theory; at $t = 0$ the commutator is

zero, and grows with some strength which the correlator $\langle x_\gamma x_\mu \rangle$ captures correctly. Furthermore, for linear dynamics this correlator is also exact, as linear dynamics also capture all rotations of the Gaussian fluctuations (as it can be seen as an underlying coordinate rotation). Thus, replacing the square of the commutator with the square of the Poisson bracket is **Good only with Gaussian Wigner Functions, and is exact to the same order as the cTWA**.

With this justification of the approximation in hand, we may write the following expression correct up to order $\mathcal{O}(t^2)$ and otherwise approximate under cTWA. Here, $\langle * \rangle$ corresponds to classical phase space averaging over a Gaussian Wigner function for points $x(t)$ and Weyl symbols of local operators $U(x), V(x)$. The negative sign comes from the factor of i^2 when replacing commutator by Poisson brackets.

$$-C(x,t) = -\langle [U(t), V(0)]^2 \rangle \approx \langle \{U(x(t)), V(x(0))\}^2 \rangle. \tag{3.15}$$

All that remains is to find an efficient way to sample the above expression in phase space. Luckily, (Das et al., 2018) asserts a form of the expression, but does not really derive it. A more detailed and basis-agnostic derivation is below.

Suppose the functions $U(x), V(x)$ only have support over a single cluster, with a convenient basis such that there is only one number, eg $U(x) = x_\alpha$ and $V(x) = x_\beta$. Note that here the indices α, β are compound, eg include both cluster operator index and cluster coordinate index. A more general single-site operator would sum over index α. Because of these generalities, these indices could be for fermionic TWA as well. The Poisson bracket becomes the following, where we choose the derivatives acting at $t = 0$ to enforce causality:

$$\{x_\alpha(t), x_\beta(0)\} = f_{abc}x_c(0)\frac{\partial x_\alpha(t)}{\partial x_a(0)}\frac{\partial x_\beta(0)}{\partial x_b(0)} = f_{a\beta c}x_c(0)\frac{\partial x_\alpha(t)}{\partial x_a(0)} \quad \text{using} \quad \frac{\partial x_\beta(0)}{\partial x_b(0)} = \delta_{\beta b}. \tag{3.16}$$

The derivative may be computed via a response to some infinitesimal perturbation $\delta x_\alpha(t)$ started at time $t = 0$

$$\delta x_\alpha(t) = \frac{\partial x_\alpha(t)}{\partial x_a(0)}\delta x_a(0) \tag{3.17}$$

where $\partial x_a(0)$ was driven by a small generator of rotation ϵ_β away from some initial point x_c. This perturbation becomes:

$$\delta x_a(0) = x_c\epsilon_\beta f_{c\beta a} \quad \rightarrow \quad \delta x_\alpha(t) = \epsilon_\beta f_{c\beta a}x_c\frac{\partial x_\alpha(t)}{\partial x_a(0)} = -\epsilon_\beta\{x_\alpha(t), x_\beta(0)\}. \tag{3.18}$$

Under nonlinear chaotic evolution this perturbation will generically grow exponentially in time, consistent with a classical Lyapanov exponent. The quantity $\delta x_\alpha(t)$ can be computed in the following way. First, choose some point in phase space x_α and evolve it forwards in time. Next, rotate that point x_α around a tiny field ϵ to get a slightly different point $\tilde{x}_\alpha$. Evolve that point in time; the quantity $\delta x_\alpha(t) = x_\alpha(t) - \tilde{x}_\alpha(t)$.

The relation to the OTOC is if one takes the square of it, averages over Gaussian initial conditions, and divides by ϵ correctly. Suppose the perturbations ϵ_β are chosen Gaussian randomly sample-to-sample with mean zero and variance $\overline{\epsilon_\beta\epsilon_\gamma} = \epsilon^2_{\beta\gamma}$. The expression becomes the following, where the overline denotes averaging with respect to random initial perturbations and $\langle * \rangle$ is averaging over phase space

$$\overline{\langle \delta x_\alpha(t)^2 \rangle} = \overline{\epsilon_\beta \epsilon_\gamma} \langle \{x_\alpha(t), x_\beta(0)\}\{x_\alpha(t), x_\gamma(0)\}\rangle. \tag{3.19}$$

To simplify, suppose the perturbations are only over one index with variance ϵ^2. This would be the case if, for example, one of the operators $V = \sigma_x$.

$$\frac{\overline{\langle \delta x_\alpha(t)^2 \rangle}}{\epsilon^2} = \langle \{x_\alpha(t), x_\beta(0)\}^2 \rangle \quad \approx \quad -\langle [X_\alpha(t), X_\beta(0)]^2 \rangle \tag{3.20}$$

The value $\delta x_\alpha(t)^2$ may be evaluated more explicitly by considering the two close by points x_α, which is unperturbed, and $\tilde{x}_\alpha$, which is perturbed by the small field ϵ_β. A simplified expression is

$$\langle \delta x_\alpha(t)^2 \rangle = \langle (x_\alpha(t) - \tilde{x}_\alpha(t))^2 \rangle = \langle x_\alpha(t)^2 \rangle + \langle \tilde{x}_\alpha(t)^2 \rangle - \langle 2 x_\alpha(t) \tilde{x}_\alpha(t) \rangle \tag{3.21}$$

The two distributions $\langle x_\alpha(t)^2 \rangle$ and $\langle \tilde{x}_\alpha(t)^2 \rangle$ are indistinguishable after phase space averaging, and due to the Gaussian fluctuations in the initial condition always equal 1 (see chapter 2 for more details on phase space flutuations). Thus, the OTOC may be written as

$$\langle [X_\alpha(t), X_\beta(0)]^2 \rangle \quad \approx \frac{\overline{\langle \delta x_\alpha(t)^2 \rangle}}{\epsilon^2} = \quad \frac{2}{\epsilon^2} \overline{\left(1 - \langle x_\alpha(t) \overline{x}_\alpha(t) \rangle \right)} \tag{3.22}$$

Which corresponds to ref. (Das et al., 2018) equation 4. $x(t)$ is a point sampled from the initial Gaussian distribution, while $\overline{x}(t)$ is the initial point, perturbed by a small amount ϵ, then evolved.

Alternative OTOC: Loschmidt Echoes

Instead of computing OTOC directly, we can instead compute the Loschmidt echo, which is the value of observables under imperfect time reversal. The Loschmidt

echo is defined as follows. Suppose some initial wavefunction $|\psi\rangle$. This state is propagated forwards for time τ according to some Hamiltonian H. Next, that wave function is perturbed for a short time ϵ by some "error" Hamiltonian $\tilde{H}$. Finally, the wave function is propagated "backwards" in time (or equivalently forwards by the negative Hamiltonian) for the same time τ. The value of observables, and overlap with the original state, is the Loschmidt echo. In graphical form

$$|\psi_0\rangle \to e^{i\tau H}|\psi_0\rangle = |\psi_1\rangle \to e^{i\epsilon\tilde{H}}|\psi_1\rangle = |\psi_2\rangle \to e^{-i\tau H}|\psi_2\rangle = |\psi_3\rangle \quad ; \quad E_O = \langle\psi_3|O|\psi_3\rangle. \tag{3.23}$$

In more compact form, the first term of ΔE can be written as the following (restating equation 2 in (Schmitt et al., 2019)) by expanding to lowest order in the pertubation strength ϵ.

$$\begin{aligned} E_O &= \langle\psi_0|\big[e^{iH\tau}e^{i\tilde{H}\epsilon}e^{-iH\tau}\big]O\big[e^{iH\tau}e^{-i\tilde{H}\epsilon}e^{-iH\tau}\big]|\psi_0\rangle \\ &\approx \langle\psi_0|e^{iH\tau}(1+i\epsilon\tilde{H})e^{-iH\tau}Oe^{iH\tau}(1-i\epsilon\tilde{H})e^{-iH\tau}|\psi_0\rangle \\ &= \langle O\rangle + +i\epsilon\langle\psi|[\tilde{H}(t),O]|\psi_0\rangle + \epsilon^2\langle\psi_0|\tilde{H}(t)O\tilde{H}(t)|\psi_0\rangle. \end{aligned} \tag{3.24}$$

If the state $|\psi_0\rangle$ is an eigenstate of O, then the second order term in E_O constitutes the OTOC: if one identifies $W = \tilde{H}$ and $V = O$, then this is the relevant part of the OTOC $\langle V(0)W(t)V(0)W(t)\rangle$ up to an eigenvalue of O. Thus, we can find OTOC by looking at the response of E_O at the order ϵ^2.

Numerical Implementations: Loschmidt Echo and OTOC

The implementation of this Loschmidt echo is simple under cTWA. First, define two Hamiltonians, H and $\tilde{H}$. Next, choose some wavefunction $|\psi\rangle$ and do standard

cTWA on the following time-dependent Hamiltonian

$$H(t) = \begin{bmatrix} t \in (0, \tau) & \to & H \\ t \in (\tau, \tau + \epsilon) & \to & \tilde{H} \\ t \in (\tau + \epsilon, 2\tau + \epsilon) & \to & -H \end{bmatrix}, \tag{3.25}$$

then measure some observable O at the end point 2τ. It is important to make sure that O is an eigen operator of $|\psi\rangle$ in accordance to the perturbative arguments connecting the Loschmidt echo to the OTOC. Note that it is relatively expensive to densely sample different times τ, as it requires that for each timestep the system must be evolved backwards again.

Similarly, the numerics to compute the explicit OTOC are relatively simple. The program is the same as the Loschmidt echo, except instead of propagate $\to$ perturb $\to$ propagate one does perturb $\to$ [propagate, propagate].

In both cases, one must also average over random realizations of the perturbation ϵ to get the effects at order ϵ^2 only.

Model Definitions

With these numerics well in hand, there are several things to explore. First is the set of Hamiltonians and perturbations $\{H, \tilde{H}\}$: H chaotic, integrable, localized, $\tilde{H}$ (not) subextensive, (not) random per realization, localization size, etc. To be concrete, below explores a specific Hamiltonian, wavefunction, and (set of) observables. They are

$$H = \sum_{\langle ij \rangle} \sigma_x^i \sigma_x^i + 0.8090 \sigma_x^{(i)} - 0.9045 \sigma_z^i, \tag{3.26}$$

$$|\psi\rangle \in \{|\uparrow\uparrow \ldots \uparrow\rangle, |\uparrow\downarrow \ldots \uparrow\downarrow\rangle\} \quad \text{Z polarized states}, \tag{3.27}$$

$$O = \sum_i o_i \sigma_z^i \text{ for some } o_i. \tag{3.28}$$

The Hamiltonian is a generically quantum chaotic Ising chain (Kim et al., 2014). The perturbation Hamiltonian is chosen as some onsite fields $\vec{B}_i$ which may or may not be averaged over. The distribution $\vec{B}_i$ depends on specific quantities of interest. For example, only having an onsite field at one site will be used to compute butterfly velocities. Averaging over random $\vec{B}_i$ so that $\langle\langle \vec{B} \rangle\rangle = 0$ means that the order ϵ contribution is zero.

$$\tilde{H} = \sum_i \vec{B}_i \vec{\sigma}^{(i)}. \tag{3.29}$$

Next is the clustering: one can use the Fermion basis (especially relevant if H is almost Free Fermions) or the local cluster basis. For the local cluster basis, one can further choose the cluster size. The Fermion basis has been studied for a specific model in (Schmitt et al., 2019).

An important parameter is the timescales $\{\tau, \epsilon\}$. These are relatively well-controlled and understood: At late times, the difference $E_O(\tau, \epsilon) - \langle\psi_0|O|\psi_0\rangle \sim e^{\tau/\tau_0}$, where τ_0 is a "Lyapanov exponent" independent of ϵ. At short times, this difference should scale as ϵ^2 consistent with perturbation theory. These, of course, can be checked under cTWA.

Scaling behavior of the Loschmidt echo

The following check of ϵ^2 scaling is as follows. The cluster size is fixed at 16 size-4 clusters (64 sites PBC), and scan over a range of ϵ, where the perturbation fields $\vec{B}_i$ are Gaussian random of mean zero variance 1, over every site, and different for every phase point sampled. The observable O is just the Z magnitization $o_i = 1$ and the wavefunction is the fully Z-polarized state. Results are shown in Fig. 3·10

There are a few takeaways from Fig. 3·10. First, the intuition about short-time perturbations is correct: they scale as ϵ^{-2}. This is shown clearly on the middle

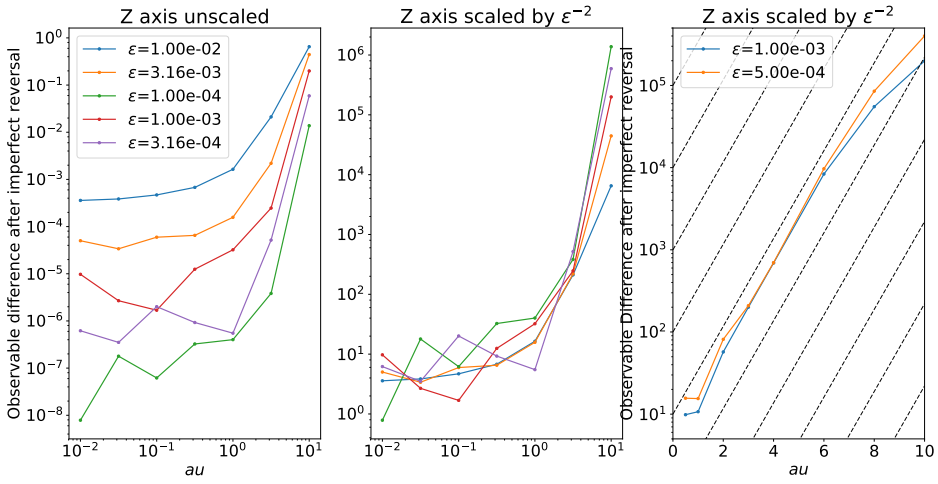

Figure 3·10: Loschmidt Echo collapse under scaling of ϵ. Left, no scaling. Middle and right, with the echo scaled by ϵ^{-2}. The exponential time scale (eg Lyapanov exponent) is found to be $\tau_c \approx 0.81$, represented by the black dashed lines.

subplot, where we plot $E_O(\tau) \times \epsilon^{-2}$. At very short times, $\tilde{H}(\tau) \approx \tilde{H}$ and so

$$E_O(\tau \to 0) = \frac{1}{N} \sum_{\vec{B}_i}^{N} \langle O \rangle + \epsilon \langle [\vec{B}_i \vec{\sigma}^i, O] \rangle + \frac{\epsilon^2}{2} \langle [\vec{B}_i \vec{\sigma}^i, [\vec{B}_j \vec{\sigma}^j, O]] \rangle \tag{3.30}$$

Averaging over $\vec{B}_i$ means the term order ϵ is zero. Similarly, we may average over $\vec{B}_i$ for the quadratic term to get a δ-function per term (using the fact that B is Gaussian), and so:

$$E_O(\tau \to 0) = \langle O \rangle + \frac{\epsilon^2}{2} \sum_{u \in [x,y,z]} \sum_i \sum_j \langle [\sigma_u^i, [\sigma_u^i, \sigma_z^j]] \rangle \tag{3.31}$$

Clearly the second term is nonzero, and equals 2. Thus, our numerics are confirmed by analytics. Note that if we did not average over B, there would be a contribution of order ϵ, unless B pointed only in the Z direction.

Second, as can be seen from Fig. 3·10 Right, is the exponential growth of the

OTOC with time. This is consistent with chaotic dynamics with the characteristic time scale $\tau_c \approx 0.81$. The quantum OTOC is also expected to grow exponentially in time (Sekino and Susskind, 2008) and is an indicator of quantum chaos. Thus, this is a way of matching quantum chaos with its analogous classical version.

Now, where things get interesting is scaling with cluster size. We know that for exact results, the echo will always be very close to 1. This should be clear from expansion of the perturbation unitary as above; the largest component is the identity. Thus, for exact results, the echo should always be of order ϵ^2, for any time (perhaps it goes to order ϵ under linear response after some time, if there isn't averaging over $\tilde{H}$?)

$$E(\tau) = \langle O \rangle + \epsilon \langle [\tilde{H}(\tau), O] \rangle + \frac{\epsilon^2}{2} \langle [\tilde{H}(\tau), [\tilde{H}(\tau), O]] \rangle \tag{3.32}$$

However, we also know that if the cluster size becomes the system size, dynamics become exact and thus **There should never be exponential growth** because dynamics are linear. Thus the natural question is: how does this exponential growth behavior change as the cluster size increases? Does τ_c, the growth coefficient, change? These questions can be answered by using the same system as for ϵ, except varying cluster size. Numerically, it is found that larger clusters have a longer lypanov timescale

$$\tau(N) = \tau_0 N^{1/4} \quad ; \quad E_O(\tau, \epsilon, N) = \epsilon^2 e^{\frac{\tau}{\tau_0 N^{1/4}}} \tag{3.33}$$

scaling as $N^{1/4}$, with N the cluster size. I have no explanation beyond phenomenology why this timescale scales as such. Of course, this is in line with intuition, as we know from the above statements that if the cluster size is the system size, there is never any exponential growth, or equivalently $\tau(N \to \infty) \to \infty$.

The butterfly velocity

One problem to apply these cTWA methods is to computing the "Butterfly velocity" of a system (Khemani et al., 2018). One expects that a de-localized system will exhibit a ballistic growth of entanglement at some velocity v_B, measuring how perturbations and correlations grow ballistically.

Butterfly velocity: Loschmidt echo

Some preliminary results of this effect are shown in Fig. 3·11. Here, we use the Ising Hamiltonian as described in equation 3.26, a Z-polarized state, Z observable, and Z perturbation, using the Loschmidt echo. However, instead of having an infinitesimal perturbation at every site, only a single site (which we call the center site, under periodic BCs) is perturbed by a random amount per sample in phase space. Then we can see the response of a distant site to this perturbation; This is the OTOC of $\langle \sigma_z^i(t)\sigma_z^0(0)\sigma_z^i(t)\sigma_z^0(0)\rangle = C(x,t)$ between site 0 and site i

There are several take-aways from this simulation. First, there is obviously a ballistic growth of the deviation as a function of time, consistent with some velocity-dependent Lyapanov exponent (VDLE) (Khemani et al., 2018) $C(x,t) \sim e^{\lambda(v)t}$ with $x = v_b t$. Furthermore, there is clear exponential growth of distant sites as a function of τ, further consistent with the VDLE. The butterfly velocity, by eye, appears to be $v_b \simeq 1.6$. This velocity is stable in cluster size.

There is also a characteristic time scale under which there is no nonlocal growth of the Loschmidt echo. This can be expected from the perspective of mean field dynamics; the deviation must grow in time, and if it is "too small" adjacent clusters simply see the same edge as the unperturbed case. However, once the perturbation grows to be of order one on the boundaries (which occurs in a time of order one), adjacent clusters' dynamics will also diverge from the unperturbed

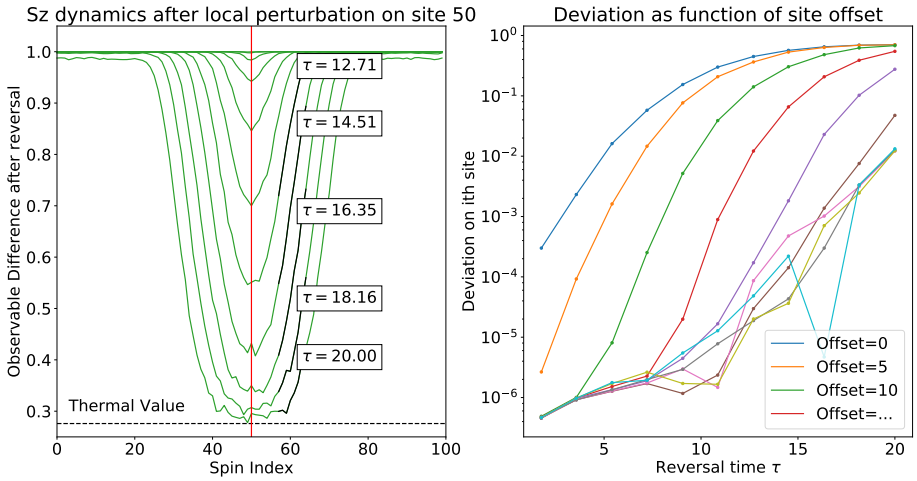

Figure 3·11: Signatures of a Butterfly velocity in the Loschmidt echo. The system is as described by equation 3.26 for a Z-polarized initial condition and infinitesemal random perturbation on the 50th site (denoted by the red line). LEFT: as time increases, the observable on a distant site decays to a thermal value, with ballistic growth. RIGHT: The same data as left, except traced through reversal time for chosen spin indexes. Here, we use size-4 clusters, although there are similar results for other cluster sizes.

limit.

Butterfly Velocity: OTOC

This butterfly behavior can be similarly computed using the explicit OTOC. Here, the system is initialized to a Z polarized state, with an initial perturbation and observable of σ_z^i, on a particular site. This computes the same OTOC as the Loschmidt echo above.

The data is shown in Fig. 3·12. There are several regimes and effects to be discussed. First off, after $t \simeq 30$ numeric floating-point copying error within the numerics causes even very far away sites to still decay to the thermal value. I have checked that this is not a physical effect by using some very tiny perturbation

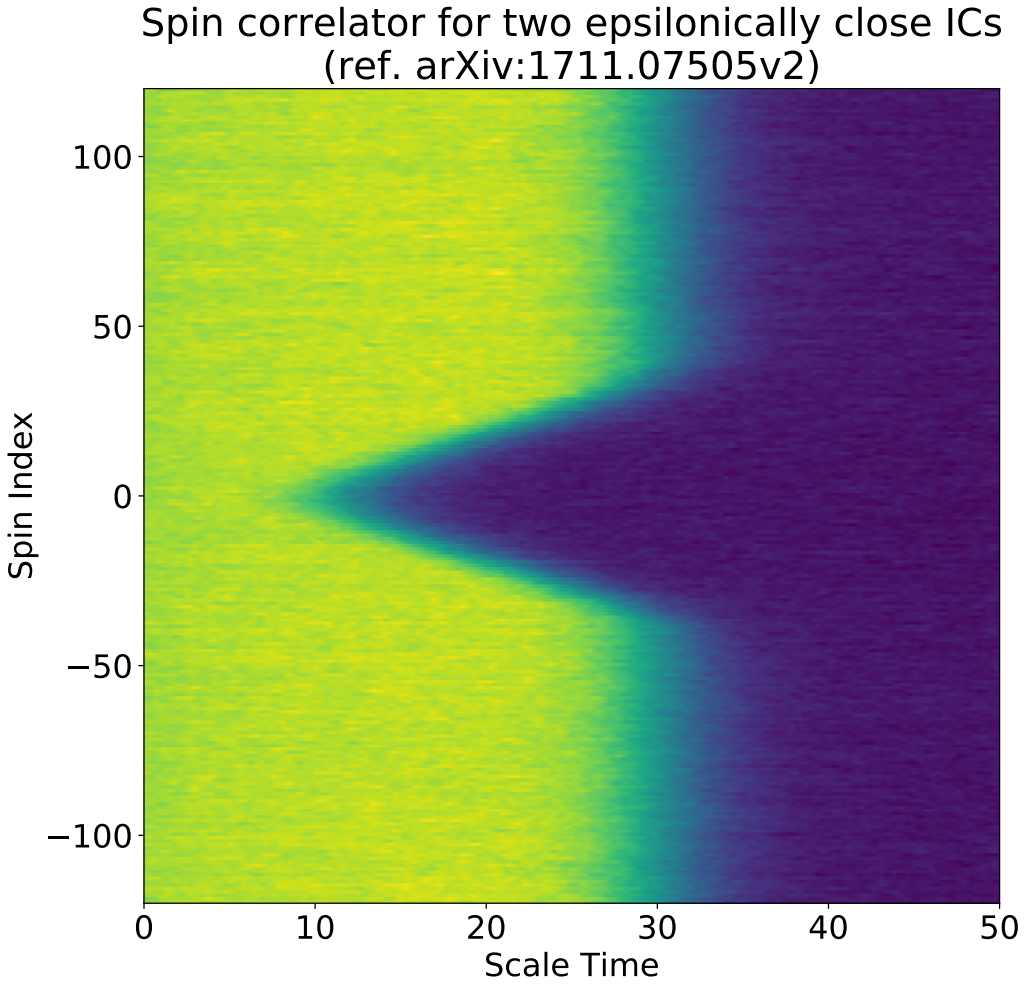

Figure 3·12: Approximate OTOC and butterfly response for the Chaotic Ising model. Here, the zeroth site is perturbed and propigated forwards in time. Clear is a ballistic growth of correlation (OTOC) until a time $t \simeq 30$, at which numeric error of $\sim 10^{-15}$ causes all correlations to disappear. Color indicates relative strength; yellow-green is strongly correlated ($C(i,t)$ small) while blue is the thermal value ($C(i,t)$ saturated). Any relation to pacman is purely coincidental.

strength $\epsilon = 1e-7$, which should have no impact on dynamics, and saw that the same decay occurs at the same time. When I set $\epsilon = 0$ then there is no decay, consistent with there being no numeric error from the integrator.

Beyond numerics, there is actual physical stuff happening as well. Specifically, one finds the same Butterfly Velocity dynamics as seen within the Loschmidt echo. This means that on some initial time scale, (on a linear scale) we see no growth of this correlator, consistent with a small but exponentially growing local perturbation. Then, after some order one time, we see ballistic growth (again, on a linear plot) of this correlation, at a characteristic butterfly speed $v_b \simeq 1.6$, the same as the Loschmidt echo case.

The behavior for different cluster sizes is the same: initial exponential growth (not visible on a linear scale) followed by ballistic growth. Different cluster sizes have the same butterfly speed front shapes. However, the time at which the ballistic growth starts increases as the cluster size increases, consistent with the same increase in the Lyapanov timescale under Loschmidt echo dynamics. This timescale is on the order of $t \approx 10$ for $\epsilon = 0.005$.

Unlike the Loschmidt echo, it is difficult to find exponential growth at early times. This is because, from point-to-point, the square of a generic observable has a variance (as the not-square has a variance). In the limit of the number of points in phase space $N \to \infty$ these fluctuations disappear, but they scale as $N^{-1/2}$ eg shot noise. This means that very early time growth, which is exponentially small, requires an exponential number of points in phase space to be sampled. Depending on how the simulation is built, this isn't that big of a deal, as propagating for a very short time is very quick.

Butterfly Velocities and front growth

Another interesting question, especially when we have two similar methods, is to ask what the butterfly velocities are, and if the fronts have particular behavior in time (eg, diffusive behavior growing as $\sqrt{t}$ (Nahum et al., 2018)). To see behavior of this front, one may go into the comoving frame, eg shift coordinates $x \to x + v_b t$ for some velocity v_b. This can be done for both the Loschmidt echo (for times τ) as well as the correlator. These results are shown in Fig. 3·13. It appears that both ballistic fronts grow with the same speed $v_b \simeq 1.6$, and at least for the short times accessible to numerics the front does not change in time.

The fact that both ballistic velocities are the same arguably is a signature that this is in fact the butterfly velocity in this system. The derivation for these values as OTOC are quite different, and so qualitatively their behavior doesn't necessarily have to be the same, either.

Secondly, it is relatively clear from the plot that the front does not widen in time, which means that is not "diffusive" like in random unitary circuits (a model for OTOC (Nahum et al., 2018)). For the correlator, this is not surprising; the authors (Das et al., 2018) used the same technique on what amounts to size-1 clusters and found no evidence of diffusive spread, instead finding spreading as $t^{1/3}$, which is much more difficult to resolve on these time scales. Inductively, that should hold for larger cluster sizes, as it amounts to dynamics of a higher-dimensional spin.

Conclusions: Loschmidt Echoes and OTOC

This section detailed computing the Loschmidt echo and out of time order correlators, which are indicators of quantum chaos, using semiclassical phase space methods. Following (Schmitt et al., 2019), the Lochmidt echo was re-derived for

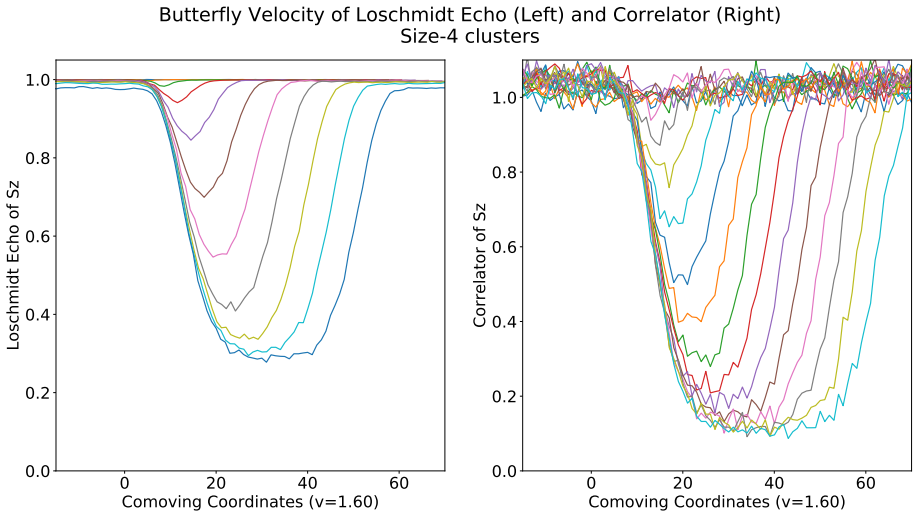

Figure 3·13: The Loschmidt echo and correlator in the co-moving frame. Here, the x axis shifted by vt with a velocity $v = 1.6$ chosen by eye. The right plot is simply making vertical slices through Fig. 3·12

general phase spaces, and then simulated for a chaotic mixed-field Ising model. It was found that the Lyapanov timescale scales as the cluster size to the 1/4 power, consistent with large-cluster-size limits. A butterfly velocity, computed from a position-dependent perturbation, was found to be $v_b \approx 1.6$ with no diffusive broadening.

Additionally, inspired by (Das et al., 2018), the OTOC for general phase spaces was derived. Using this phase space OTOC, a position-dependent pertubation was used for a chaotic mixed-field Ising model to compute a butterfly velocity of $v_b \approx 1.6$, consistent with the velocity computed from the Loschmidt echo.

Future work could be to find more rigorous bounds for (sub)diffusion of the butterfly fronts. This has numerical challenges, however, as numerical precision bounds times to be less then $t \approx 30$ consistent with chaotic dynamics. Alternate future work would be to inspect integrable or almost-integrable models, or classical models which are not chaotic to see if there is different behavior. However, in my

opinion the study of the OTOC was a passing fad and now has waning interest.

Chapter 4

The rotated cluster truncated Wigner approximation

This section will outline an important generalization of the cTWA. Suppose a group of trace-orthogonal operators $\{X\}$ which forms a phase space basis. This set retains its group properties under arbitrary unitary rotations acting on each operator: $X_i \to U^\dagger X_i U = X_i'$. This is relatively clear to see, using cycliciticity of the trace and $U^\dagger U = 1$

$$\mathrm{Tr}[X_i' X_j'] = \mathrm{Tr}[U^\dagger X_i U U^\dagger X_j U] = \mathrm{Tr}[X_i X_j], \tag{4.1}$$

$$[X_i', X_j'] = X_i' X_j' - X_j' X_i' = U^\dagger X_i U U^\dagger X_j U - U^\dagger X_j U U^\dagger X_i U = U^\dagger [X_i, X_j] U = f_{ijk} X_k'. \tag{4.2}$$

Thus, this new set $\{U^\dagger X_\alpha U\} = \{\tau_\alpha\}$ is also a well defined phase space basis, with all of the same geometry as the original basis $\{X_\alpha\}$.

A base idea used extensively elsewhere is that this unitary must act only on a single cluster, eg local coordinate transforms. However, nothing is restricting this unitary from acting over the entire Hilbert space, other then the object being more difficult to figure out. For example, suppose two clusters (L, R). Originally, I would imagine basis rotations (eg, linear evolution) as $U = U^L \otimes U^R$. Generically, I can make a unitary which acts non trivially on both clusters. This may mean an operator acting between clusters might be represented by a single (linear) operator

within the group $\{\tau_\alpha\}$, at the expense that other operators that were once linear are now nonlinear. if it is local, this unitary may act to "dress" cluster boundaries, such that operators may be slightly nonlocal and thus capture dynamics better within the phase space.

Generally, these unitaries can be annoying to work with. This is because it is a large (Hilbert space acts over multiple clusters) operator with a priori no particular structure. One subset of such unitaries are those generated by an adiabatic gauge potential (AGP) as will be discussed later.

A simple sub-set of unitary operators are those of the Clifford group (Gottesman, 1998). As a reminder, the Clifford group is the group of unitaries which send chains of Pauli spin operators to chains of pauli spin operators. The simplest set of Clifford operators is the CNOT, Hadamard, and Phase gates, which map operators as such:

CNOT			Hadamard
YI	→	YX	X→ Z
IX	→	IX	Z→ X
XI	→	XX	Y→ -Y
ZI	→	ZI	
YZ	→	XY	Phase
IY	→	ZY	X→ Y
IZ	→	ZZ	Y→ -X
II	→	II	Z→ Z
YX	→	YI	
XX	→	XI	
XY	→	YZ	
ZX	→	ZX	
ZY	→	IY	
ZZ	→	IZ	
YY	→	XZ	
XZ	→	YY	

(4.3)

In this way, it is simple to construct the action of some unitary acting on some

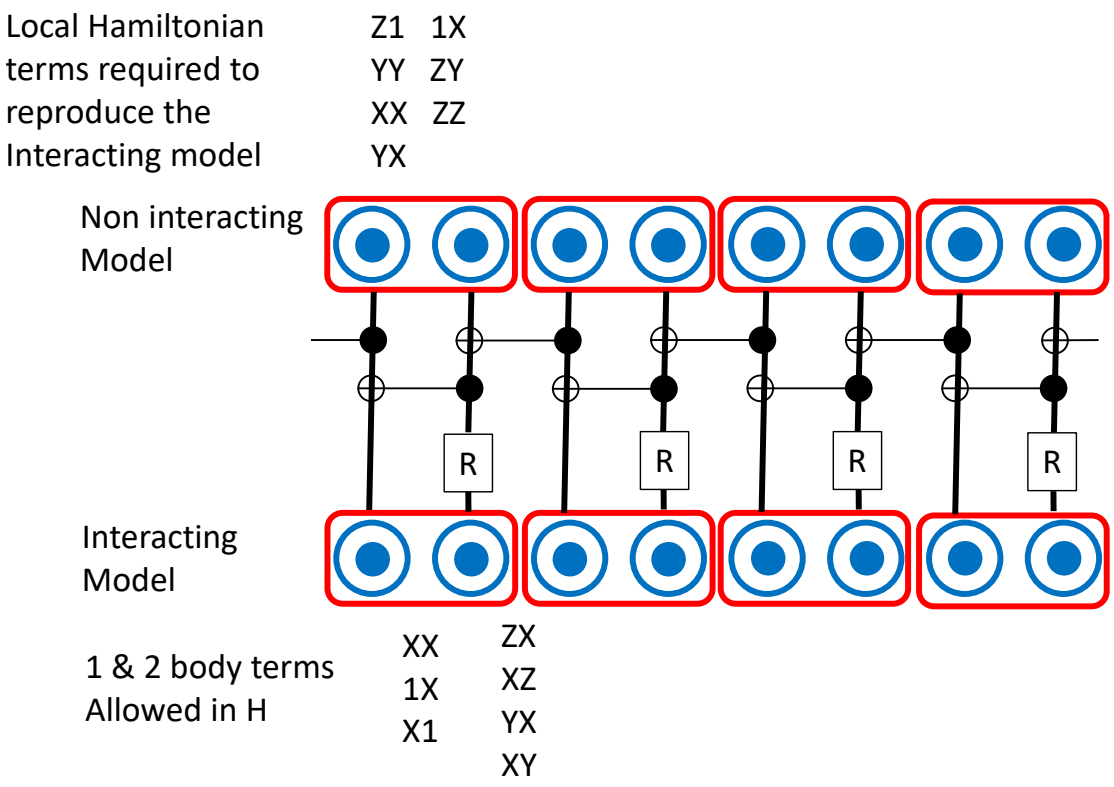

Figure 4·1: An example gate mapping for a linear Hamiltonian under cTWA

group pauli operators $\{X_\alpha\}$ to compute some new group of trace orthogonal and closed operators $\{\tau_\alpha\}$.

Such a set of Clifford gates implementing a particular unitary is shown in Fig. 4·1. Here, all operators local to size-2 clusters (top) are dressed by the unitary implemented by the gate structure, to create a new group of operators. For example, for the basis generated by Pauli strings, this becomes:

	Interacting basis $\{\tau_\alpha\}$		Simple basis $\{X_\alpha\}$	
τ_0	`1XZX`	$\leftrightarrow$	`1X11`	X_0
τ_1	`XYZX`	$\leftrightarrow$	`1Y11`	X_1
τ_2	`XZ11`	$\leftrightarrow$	`1Z11`	X_2
τ_3	`11ZX`	$\leftrightarrow$	`11X1`	X_3
τ_4	`1X11`	$\leftrightarrow$	`1XX1`	X_4
τ_5	`XY11`	$\leftrightarrow$	`1YX1`	X_5
τ_6	`XZZX`	$\leftrightarrow$	`1ZX1`	X_6
τ_7	`XZYX`	$\leftrightarrow$	`11Y1`	X_7
τ_8	`XYX1`	$\leftrightarrow$	`1XY1`	X_8
τ_9	`1XX1`	$\leftrightarrow$	`1YY1`	X_9
τ_{10}	`11YX`	$\leftrightarrow$	`1ZY1`	X_{10}
τ_{11}	`XZX1`	$\leftrightarrow$	`11Z1`	X_{11}
τ_{12}	`XYYX`	$\leftrightarrow$	`1XZ1`	X_{12}
τ_{13}	`1XYX`	$\leftrightarrow$	`1YZ1`	X_{13}
τ_{14}	`11X1`	$\leftrightarrow$	`1ZZ1`	X_{14}

(4.4)

Here, the notation `1X11` denotes the operator σ_x^1 acting on the first site of a 4-site chain. There are 15 simple basis operators corresponding to all permutations of `X,Y,Z,1` and a corresponding number in the interacting basis. One can check that the interacting basis also forms a closed group. One can pick all 2-site terms to write a Hamiltonian acting only with 2 spin terms

$$H = \sum_i h\sigma_x^i + \sum_{i \text{ even}} J_{xx}\sigma_x^i\sigma_x^{i+1} + \sum_{i \text{ odd}} J_{xz}\sigma_x^i\sigma_z^{i+1} + J_{zx}\sigma_z^i\sigma_x^{i+1} + J_{xy}\sigma_x^i\sigma_y^{i+1} + J_{yx}\sigma_y^i\sigma_x^{i+1}. \tag{4.5}$$

Observe, in the basis $\{X_\alpha\}$ this includes terms which are nonlinear acting between clusters (such as $\sum_{i \text{ odd}} J_{xz}^i\sigma_x^i\sigma_z^{i+1}$). However, in the rotated basis $\{\tau_\alpha\}$ these terms are **linear** in cluster operators, which means that dynamics is exact.

$$H(x) = \sum_{i'} h(x_0^{i'} + x_3^{i'}) + J_{xx} x_4^{i'} + J_{xz} x_3^{i'} x_2^{i'+1} + J_{zx} x_{11}^{i'} x_0^{i'+1} + J_{xy} x_3^{i'} x_1^{i'+1} + J_{yx} x_7^{i'} x_0^{i'+1},$$

$$H(\tau) = \sum_{i'} h(\tau_4^{i'} + \tau_{14}^{i'}) + J_{xx} \tau_9^{i'} + J_{xz} \tau_2^{i'} + J_{xz} \tau_3^{i'} + J_{xy} \tau_5^{i'} + J_{yx} \tau_{10}^{i'}. \quad (4.6)$$

Finally, one may find the Wigner function in the $\{\tau_\alpha\}$ variables and compute time evolution. A Wigner function which factorizes between clusters in the simple basis (eg a product state) may no long factorize between dressed clusters in the $\{\tau_\alpha\}$ variables. It is an equivalent procedure to propagate the initial wave function *backwards* with respect to the unitary, then compute the Wigner function with respect to the unrotated variables. This rotation may create additional entanglement to an initial product state, which adds correlations in the Wigner function. This may go in reverse as well: a wave function which is entangled in particular ways may be disentangled or become simpler by this reverse unitary, and thus make the Wigner function factorize.

One of these simple initial wave functions for this particular model is a product state $|\psi\rangle = |\downarrow + \downarrow + \ldots\rangle$, where $|+\rangle$ is the $+1$ eigenvalue of σ_x. The Hadamard gate rotates the X eigenvalue to a Z eigenvalue, and then the Z polarized state is affected by the CNOT gates, keeping it unentangled.

It is simple to compute expectation values of particular observables; for example, σ_x maps to τ_4 and τ_{14} which are easy to compute.

Dynamics of this model for initial state $|\psi\rangle = |\downarrow + \downarrow + \ldots\rangle$, observables σ_x^{odd} and σ_x^{even}, and Hamiltonian parameters $h = 0$, $J_{xx} = 1$, $J_{xy} = J_{yx} = \sqrt{2}$, $J_{zx} = J_{xz} = \sqrt{3}$ are shown in Fig. 4·2. It is clear that the unrotated basis, which is the simple size-2 cluster cTWA, is asymtotically exact at short times but wrong at long times. However, the rotated version is the same as the exact result, which

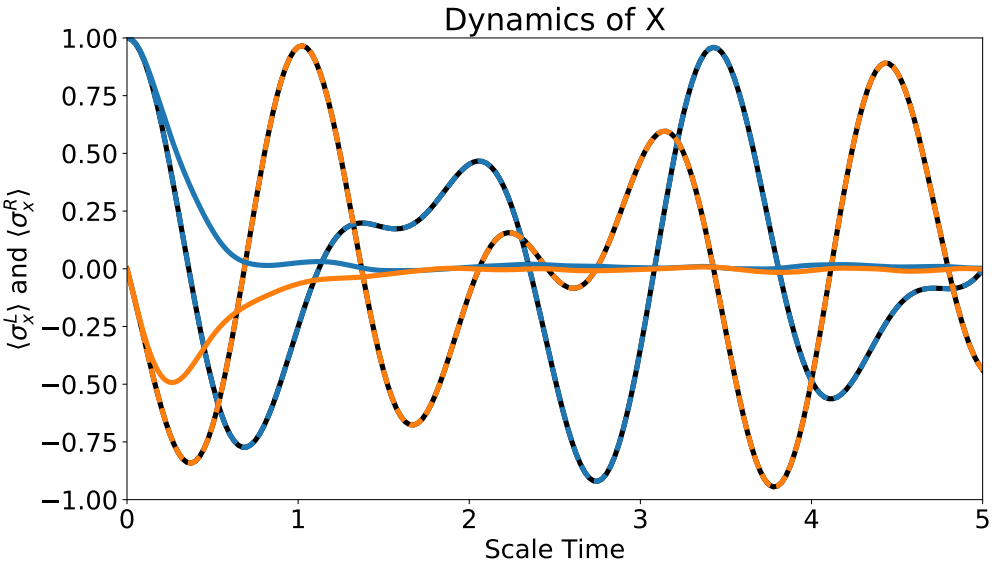

Figure 4·2: Rotated cTWA Observable dynamics of Hamiltonian (4.5)**.** Observables are even and odd σ_x. Black is exact results; colored dashed is rcTWA results; colored filled is cTWA results for size-2 clusters.

is in black overlaid with the dashed rotated version. This emphasizes that the choice of operator basis is important: dynamics may be exact or much closer to in one basis then another!

Extensions of rcTWA

In the above example, the unitary was chosen to be very specific such that implementing it is relatively simple. Furthermore, the example Hamiltonian itself was chosen such that it conspired to be exactly linear in the rotated basis. However, it is generally possible to choose more complicated unitary rotations which do not necessarily have as simple of a structure.

One such way to compute a unitary rotation is to instead compute the generator of rotations S. One particular choice of this generator is the adidiabatic gauge potential (AGP) connecting the Hamiltonian to a nearby point. This choice will

be heavily justified and examined in a different context of Schrieffer-Wolff and state dressing in chapter 5. A thorough investigation of the performance of such rotations for rcTWA is beyond the scope of this thesis.

Chapter 5

Variational Schrieffer Wolff rotations and Adiabatic Dressing

One of the main challenges in quantum theory is computing the dynamics of involved quantum systems without having to resort to exact diagonalization or conventional perturbation theory (Griffiths, 2005). While exact dynamics are generally out of reach, one potential way of obtaining approximate dynamics is through a basis rotation, simplifying the rotated Hamiltonian and the resulting dynamics in a new frame. An extreme example is going to the eigenbasis of the Hamiltonian, where the dynamics are trivial – each state simply picks up a phase. Unfortunately, this basis is generally inaccessible due to the prohibitively large Hilbert space, and approximate methods need to be found. One such alternative method is the Schrieffer-Wolff (SW) transformation (Schrieffer and Wolff, 1966; Bravyi et al., 2011). Provided there's a clear separation of energy scales within a given Hamiltonian, one finds a unitary transformation block-diagonalizing and thus decoupling the low- and high-energy subspaces of the model. The low-energy dynamics then follow from an effective SW Hamiltonian. However, the traditional way of implementing the SW transformation is perturbative and can be used only if there is a very large energy scale separation, otherwise one quickly encounters the problem of small denominators. Alternatively, mapping a static Hamiltonian to a Floquet problem in the rotating frame and applying the van Vleck high frequency

expansion, which was shown to be equivalent to the SW transformation (Bukov et al., 2016), one deals with an asymptotic series that also becomes uncontrollable in the absence of such a large energy scale separation (Abanin et al., 2015; Kuwahara et al., 2016). Similar principles (Vogl et al., 2019) underlie the Wegner flow, where a flow equation is constructed band-diagonalizing the Hamiltonian through the systematic suppression of off-diagonal matrix elements associated with smaller and smaller energy differences (Wegner, 1990).

These diagonalization methods can be reinterpreted in the context of adiabatic gauge potentials (AGPs) (Kolodrubetz et al., 2017a), which are infinitesimal generators of a unitary transformation diagonalizing a given Hamiltonian. Recent works have allowed for controllable variational approximations to the AGP, which lead to unitary transformations partially diagonalizing the Hamiltonian (Sels and Polkovnikov, 2017; Kolodrubetz et al., 2017a; Claeys et al., 2019). The variational AGP is guaranteed to converge to the exact one if the number of variational parameters becomes sufficiently large. In practice, the convergence properties depend on the details of the Hamiltonian, the choice of the variational manifold, the particular energy sector one is interested in, and so on. But even with these limitations, the variational SW transformation has a clear advantage over the perturbative expansions, which generally have a zero radius of convergence. This advantage stems from the fact that the generator of the rotation can be stably computed at any value of the couplings. In this work, we show how Hamiltonians rotated using variational AGPs allow for accurate simulations of dynamics at a fraction of the cost of exact methods. This methodology then allows a description of low-energy quenches and other effective dynamics of interacting quantum systems in non-perturbative regimes.

An alternative perspective of Schrieffer-Wolff block diagonalization with the

adiabatic gauge potential is one of adiabatic continuation (Hastings and Wen, 2005). Given some Hamiltonian of interest, low energy eigenstates of that system may be computed by finding a "simple" Hamiltonian "nearby" in parameter space, which can be easily diagonalized. Then, those simple eigenstates can be mapped to interacting ones using some dressing by a unitary U. This procedure can be used to show that ground states can be mapped to other ground states, as long as there is some path in parameter space which does not go through some gap-closing critical point (Nachtergaele and Sims, 2006; Hastings, 2007; Chen et al., 2010). For example, low energies of interacting fermions may be described by a Fermi gas or Fermi liquid with dressed quasiparticle excitations (Shankar, 1994). However, most of these proofs are non-constructive in the sense that the unitary U is generally never actually computed, or only done so perturbatively.

From this perspective, non-interacting trivial eigenstates are dressed to form nontrivial interacting ones. The AGP evolution modifies non-interacting particle states to quasiparticle states which are "dressed" within some local span of sites. Importantly, the dressing is non-perturbative and not limited to low-energy states. This construction leads to long-lasting quasiparticles and stable nonthermal states, even at finite energy densities.

As a consequence of computing unitary rotations for approximate eigenstates, this procedure also allows one to compute local almost-conserved operators from the approximate eigenstates and dressed non-interacting symmetries. In the presence of integrability breaking terms in some system, undressed symmetries and conserved operators are generally no longer conserved (Langen et al., 2016; Bertini et al., 2016; Tang et al., 2018): instead, these operators may be "dressed" locally by the unitary U to restore approximate conservation of some quasi-local and long lived operator, even though the full system may no longer be integrable (Serbyn

et al., 2013; Imbrie, 2016; Abanin et al., 2017).

The presence of such unitary dressings, quasi-local conservation laws, and good approximate eigenstates in interacting models may suggest that not all integrability-broken models should be treated equally. Certain models may be "close to integrable", in the sense that there exists a good local dressing of particular eigenstates, and strong ETH may be violated. Two particular cases of such ETH violation are many body localization (Abanin et al., 2019) and quantum scars in the PXP model (Bernien et al., 2017; Turner et al., 2018b). Conversely, other models may be far from any simple system, in the sense that there is no path in parameter space that admits a good local adiabatic dressing, and the model is quantum chaotic (Srednicki, 1994). In fact, this unitary rotation may potentially be seen as the analog of the canonical transformation of KAM theory which restores integrability in classical models (Brandino et al., 2015). While this paper focuses on a quantum model, the whole methodology, including variationally computed canonical transformations generated by the AGP (Kolodrubetz et al., 2017b), is fully applicable to classical non-integrable systems.

This method is illustrated on two classes of systems. First, we consider a disordered strongly-attractive Fermi-Hubbard model which, using the lowest order SW transformation, can be mapped to the disordered Heisenberg Hamiltonian (Blundell, 2001), where empty and doubly-occupied states form effective spin degrees of freedom. If the disorder is sufficiently large this model exhibits many-body localization, which is manifested in absence or near absence of thermalization (Abanin et al., 2019). Using the variational approach we go beyond this perturbative construction and obtain a more accurate effective Hamiltonian, which contains a mixture of singly-occupied sites. In turn this mixture leads to enhanced transport in the system and restores quench thermalization in the system.

Next, we apply this method to spin 1/2 chains. The first model is the XY model which maps to free fermions, with an additional symmetry breaking X-field. Using a SW dressing of the Hamiltonian, we calculate time-dependent response functions above the ground state. The second is the nonintegrable mixed-field Ising model, where we use adiabatic continuation to dress states and compute approximate eigenstates and conserved operators.

5.1 Methodology: Schrieffer-Wolff / Heisenberg picture

The goal of the proposed approach corresponds to that of the Schrieffer-Wolff (SW) transformation (Bravyi et al., 2011): given a Hamiltonian acting on different subspaces, an effective Hamiltonian is found acting only on a single subspace, integrating out the degrees of freedom from other subspaces. These are generally taken to be low- and high-energy subspaces (as in Fig. 5·1), leading to an effective low-energy Hamiltonian. Given an unperturbed Hamiltonian H_0 with well-separated energy subspaces (in the Figure represented by highly-degenerate levels separated by an energy scale Ω), a term added to this Hamiltonian as

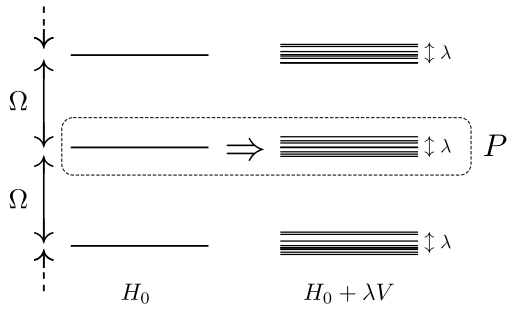

Figure 5·1: A Hamiltonian H_0 with massively degenerate energy levels separated by Ω. An extra term λV breaks this degeneracy and induces level splitting on the order of λ, but dynamics within a given subspace P may still be well-described via a SW rotation.

$$H = H_0 + \lambda V \tag{5.1}$$

will break this degeneracy and lead to level-splitting in the spectrum of the total Hamiltonian. Here, we assume the strength of the perturbation λ to be small

enough such that the mixing between different degenerate sectors of H_0 is not very strong (loosely speaking, $\lambda < \Omega$). Starting from a state within a subspace P, the dynamics of the full model will mainly be governed by the Hamiltonian acting within this subspace, with states within the complement Q of this subspace only leading to small high-frequency deviations. The goal of the SW transformation is to find an effective Hamiltonian acting only within P that is able to describe these dynamics. Conventionally the SW transformation splits into three steps.

First, some projective subspace P is identified in which the Hamiltonian H_0 is block-diagonal. This could be a specific energy sector(s) (as in Fig. 5·1), or alternatively some symmetry sector(s) of H_0. Second, one finds a unitary rotation U to a new basis "$\sim$" such that the Hamiltonian transformed by this unitary $\tilde{H} = U^\dagger H U$ is block-diagonal in P or, equivalently, the original Hamiltonian is block-diagonal in the transformed basis $\tilde{P}$ (see also Fig. 5·2),

$$\tilde{H} = U^\dagger H U \quad \leftrightarrow \quad \mathcal{P}\tilde{H}\mathcal{Q} + \mathcal{Q}\tilde{H}\mathcal{P} = 0, \tag{5.2}$$

$$\tilde{\mathcal{P}} = U\mathcal{P}U^\dagger \quad \leftrightarrow \quad \tilde{\mathcal{P}}H\tilde{\mathcal{Q}} + \tilde{\mathcal{Q}}H\tilde{\mathcal{P}} = 0, \tag{5.3}$$

where $\mathcal{P}$, $\mathcal{Q}$ stand for the projectors to the subspaces P and Q, respectively. Third, an effective Hamiltonian is constructed as a projection of $\tilde{H}$ into the block P

$$\tilde{H}_{\text{eff}} = \mathcal{P}\tilde{H}\mathcal{P}. \tag{5.4}$$

This Hamiltonian effectively projects out the degrees of freedom outside of P such that the dynamics of wave functions with overlap predominantly in subspace $\tilde{P}$ can then be described in terms of this effective Hamiltonian. As such, this new Hamiltonian $\tilde{H}_{\text{eff}}$ has the clear advantage that it acts on a reduced Hilbert space, which can be substantially smaller than that of the original Hamiltonian.

Finally, within the context of quantum dynamics, given some initial wave function $|\psi(0)\rangle$, we wish to find time evolution with respect to H using this reduced Hilbert space. This is equivalent to

$$\begin{aligned} |\psi(t)\rangle &= \exp\big(-itH\big)|\psi(0)\rangle \\ &= U\exp\big(-it\tilde{H}\big)|\tilde{\psi}(0)\rangle \\ &\approx U\exp\big(-it\tilde{H}_{\text{eff}}\big)|\tilde{\psi}(0)\rangle, \end{aligned} \tag{5.5}$$

with $|\tilde{\psi}(0)\rangle = U^\dagger|\psi(0)\rangle$, and where the last expression is exact provided the initial wave function lies within the low-energy sector $\mathcal{P}|\tilde{\psi}(0)\rangle = |\tilde{\psi}(0)\rangle$. Expectation values of observables can be obtained in the standard way as

$$\begin{aligned} \langle\psi(t)|\mathcal{O}|\psi(t)\rangle &= \langle\tilde{\psi}(0)|e^{it\tilde{H}}U^\dagger\mathcal{O}Ue^{-it\tilde{H}}|\tilde{\psi}(0)\rangle \\ &\approx \langle\tilde{\psi}(0)|e^{it\tilde{H}_{\text{eff}}}U^\dagger\mathcal{O}Ue^{-it\tilde{H}_{\text{eff}}}|\tilde{\psi}(0)\rangle. \end{aligned} \tag{5.6}$$

Thus, dynamics of the system can be obtained in one of two ways. Naively, one can calculate dynamics with respect to H, which may be difficult due to an excessively large Hilbert space size. Alternatively, one may rotate and project all operators and observables to the transformed ("$\sim$") basis and calculate projective dynamics (as in Eq. (5.6)).

The main difficulty in the above way of implementing the SW transformation is finding the rotation U, especially if the coupling λ is not too small. Various perturbative expansions exist (Bravyi et al., 2011; Michailidis et al., 2018), but they mainly rely on the massive degeneracy of the ground state and large energy gaps in H_0 in order to be practical. There is an alternative approach based on first mapping the static Hamiltonian to the Floquet one, and then using the high-

frequency expansions (Bukov et al., 2016), with similar complications of being generally asymptotic and uncontrolled unless taking the limit $\lambda \to 0$. A central result of this chapter is developing a controllable and convergent, at least in principle, *approximation* to the unitary U, which can be practically used even at intermediate values of the coupling λ.

Generating the rotation

Rather than immediately calculating the unitary U, we will first compute its generator. Consider a family of unitary transformations $U(\mu)$ with $U(0) = 1$ defined with respect to the running parameter $\mu \in 0 \dots \lambda$ and their infinitesimal generators $A(\mu) = i[\partial_\mu U(\mu)]U^\dagger(\mu)$ such that

$$U^\dagger(\mu) = \mathcal{T} \exp\left(i \int_0^\mu A(\mu') d\mu' \right), \tag{5.7}$$

where $\mathcal{T}$ stands for the path ordering symbol with respect to μ'. At these intermediate points $\mu \in 0 \dots \lambda$, one may define a parameterized Hamiltonian $H_0 + \mu V$ which is rotated by the unitary $U(\mu)$ into the "$\sim$" frame

$$\tilde{H}(\mu) = U^\dagger(\mu) \left(H_0 + \mu V \right) U(\mu). \tag{5.8}$$

The generator $A(\mu)$ is chosen such that at all points $\mu \in [0, \lambda]$, the rotated Hamiltonian $\tilde{H}(\mu)$ is block diagonal in P and Q,

$$\mathcal{P}\tilde{H}(\mu)\mathcal{Q} = 0. \tag{5.9}$$

The unitary $U(\lambda)$ found in this way then generates the desired Schrieffer-Wolff rotation. To compute the form of $A(\mu)$ one may differentiate Eq. (5.9) with

respect to μ,

$$\begin{aligned}&\partial_\mu\big[\mathcal{P}\tilde{H}(\mu)\mathcal{Q}\big]=0,\\&\Rightarrow\mathcal{P}U^\dagger(\mu)\Big(V+i[A(\mu),H(\mu)]\Big)U(\mu)\mathcal{Q}=0.\end{aligned}\tag{5.10}$$

The solution to this equation is obviously not unique, since one can perform arbitrary unitary rotations within the sub-blocks P and Q as well as add any operator to $A(\mu)$ which commutes with $H(\mu)$.

A particular solution to this equation is the adiabatic gauge potential (AGP) $\mathcal{A}(\mu)$ (Kolodrubetz et al., 2017a), which is defined as the generator of evolution of instantaneous Hamiltonian eigenfunctions in parameter space: for Hamiltonian $H(\mu)$ and eigenstates $|n(\mu)\rangle$ the AGP $\mathcal{A}(\mu)$ satisfies

$$\mathcal{A}(\mu)|n(\mu)\rangle\equiv i\partial_\mu|n(\mu)\rangle.\tag{5.11}$$

If $A(\mu)=\mathcal{A}(\mu)$, the rotated Hamiltonian $\tilde{H}$ becomes exactly diagonal in the eigenbasis of H_0,

$$\tilde{H}(\mu)=\sum_n|n(0)\rangle E_n(\mu)\langle n(0)|.\tag{5.12}$$

with the correct eigenvalues of $H_0+\mu V$. Thus, the AGP satisfies a stronger requirement than Eq. (5.9) imposes: $\tilde{H}(\mu)$ has no off-diagonal matrix elements, not just those for states belonging to different subspaces. In other words, it is a good SW generator for *any* choice of energy subspace P, Q. This fact is illustrated in Fig. 5·2.

Recasting Eq. (5.11) for all states (Sels and Polkovnikov, 2017) yields an

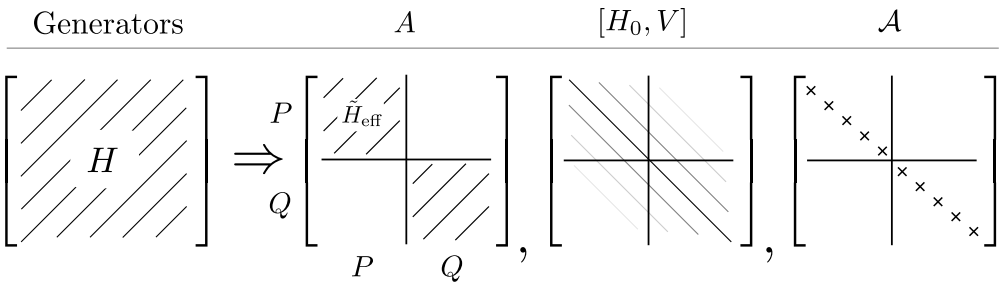

Figure 5·2: Graphical representation of various Hamiltonian transformations depending on the generator. A Hamiltonian H is written in the eigenbasis of H_0 (which can be separated in subspaces $P + Q$), and generically has off-diagonal elements. The Schrieffer-Wolff generator A block-diagonalizes this Hamiltonian, the Wegner-flow generated by the first-order approximation to the gauge potential $[H_0, V]$ band-diagonalizes this Hamiltonian by suppressing off-diagonal elements between states with large energy differences, and the exact adiabatic gauge potential $\mathcal{A}$ goes a step further by exactly diagonalizing H in the eigenbasis of H_0.

operator equation similar to Eq. (5.10) but without any projectors:

$$\big[V + i[\mathcal{A}(\mu), H(\mu)], H(\mu)\big] = 0. \tag{5.13}$$

This equation is even more difficult to solve than Eq. (5.10) because solving it amounts to fully diagonalizing the Hamiltonian. Moreover, the exact AGP is generally an exponentially divergent and highly nonlocal operator in the thermodynamic limit (Kolodrubetz et al., 2017a). However, there has been recent work on finding various *local approximations* to the exact gauge potential (Sels and Polkovnikov, 2017; Claeys et al., 2019). Such approximations were shown to be able to efficiently reproduce the action of the gauge potential between states that can be distinguished by local operators. These can be states corresponding to either different energy sectors or symmetry sectors of H_0. In particular, local approximations of the AGP were shown to efficiently suppress matrix elements of the rotated Hamiltonian between states separated by large energies while failing to

diagonalize it with states close in energy (Claeys et al., 2019). As we will show below, the local AGP is also efficient at suppressing matrix elements between states with close energies as long as they belong to different blocks of the unperturbed Hamiltonian. Therefore identifying the generator of the SW transformation $A(\mu)$ with local approximations of the AGP leads to an accurate approximation to the unitary $U(\lambda)$.

From an adiabatic continuation standpoint, the connection with this approximate gauge potential is clear; in fact M. Hastings in (Hastings and Wen, 2005) has is a particular implementation of an approximate AGP for gapped ground states. A simplification of Eq. (17) in Ref. (Hastings and Wen, 2005) defining a rotation $\tilde{V}(s)$ (analogously $U^\dagger$) as

$$\tilde{V}(s) = \mathcal{S}' \exp\Big\{ -\int_0^s ds' \int_0^\infty d\tau e^{-(\tau/\tau_q)^2/2} [\tilde{u}^+_{s'}(i\tau) - \text{H.c.}] \Big\}. \tag{5.14}$$

Here, $\mathcal{S}'$ is parameter ordering (analogously $\mathcal{T}$) for parameter s' (analogously μ). The object $\tilde{u}^+_{s'}(i\tau)$ is defined as

$$\tilde{u}^{\pm}(\pm i\tau) \equiv \frac{1}{2\pi} \int_{-\infty}^{\infty} dt \frac{[\partial_s H_s](t) e^{-(t/\tau_q)^2/2}}{\pm it + \tau} \tag{5.15}$$

with $[*](t)$ denoting time evolution with respect to instantaneous Hamiltonian $H_{s'}$ (analogously $H(\mu)$). Substituting this into the inner integrand and simplifying by integrating over τ yields

$$\int_0^\infty d\tau e^{-(\tau/\tau_q)^2/2}[\tilde{u}^+_{s'}(i\tau) - \text{H.c.}] \tag{5.16}$$

$$= \frac{1}{2\pi}\int_{-\infty}^{\infty} dt[\partial_s H_s](t)e^{-(t/\tau_q)^2/2}\int_0^\infty d\tau e^{-(\tau/\tau_q)^2/2}\left[\frac{2it}{t^2+\tau^2}\right] \tag{5.17}$$

$$= \frac{1}{2\pi}\int_{-\infty}^{\infty} dt[\partial_s H_s](t)e^{-(t/\tau_q)^2/2}\left[- i\pi e^{(t/\tau_q)^2}\text{erfc}\Big(\Big|\frac{t}{\sqrt{2}\tau_q}\Big|\Big)\text{SGN}(t)\right] \tag{5.18}$$

$$= \frac{-i}{2}\int_{-\infty}^{\infty} dt[\partial_s H_s](t)\text{erfc}\Big(\Big|\frac{t}{\sqrt{2}\tau_q}\Big|\Big)\text{SGN}(t).$$

This integrand is the generator of the unitary rotation, which is also written as an approximation of the adiabatic gauge potential

$$\mathcal{A}(\mu) \approx -\frac{1}{2}\int_{-\infty}^{\infty} \text{SGN}[t]f(t)[\partial_\mu H](t)dt, \tag{5.19}$$

$$f(t) = \text{erfc}\left(\left|\frac{t}{\tau_q}\right|\right) \tag{5.20}$$

where $\partial_\mu H(t)$ is the operator $\partial_\mu H$ in the Heisenberg representation, erfc is the complementary error function for which $\text{erfc}(0) = 1$ and $\text{erfc}(\infty) = 0$, and $\text{SGN}(t)$ is ± 1 depending on sign of t. This expression is nothing but an approximation of the gauge potential with a particular choice of regularizer $f(t)$ (Claeys et al., 2019). For the regularization time $\tau_q \to \infty$, this approximate AGP becomes exact. For a finite regularization time, the AGP is approximate but local within some span of sites.

Instead of using a regularizer, this AGP can be computed variationally. This means the accuracy of the approximation is determined not by smallness of the

perturbation of λ but by the locality of rotations needed to block-diagonalize the Hamiltonian. It is also controlled by the size of the variational manifold used to find the approximate gauge potential: as the number of variational parameters increases the variational AGP approaches the exact one. As we will show using two particular examples, one can get a very good convergence even well beyond the regime of applicability of conventional perturbative approaches. More specifically, Eq. (5.13) can be recast as the minimization of an action. Following (Sels and Polkovnikov, 2017), suppose some ansatz for an approximate gauge potential over some subset of local operators $\{B_i\}$ (for example, all operators with a fixed finite spatial support)

$$A(\mu, \{\alpha\}) = \sum_i \alpha_i B_i. \tag{5.21}$$

One can compute the best variational solution to coefficients $\{\alpha_i\}$ by computing the minimum Hilbert-Schmidt tracenorm $||A|| = \mathrm{Tr}\big[A^2\big]/\mathcal{D}$ of Eq. (5.13)

$$\text{MIN:} \quad \Big|\Big|\big[H(\mu), V + i[A(\mu, \{\alpha\}), H(\mu)]\big]\Big|\Big|. \tag{5.22}$$

Finding this minimum amounts to quadratic minimization of coefficients α_i and the absolute minimum of this norm is achieved precisely when $A(\mu, \{\alpha\}) = \mathcal{A}(\mu)$. Remarkably, since the resulting tracenorm can generally be calculated without constructing the operator in the full Hilbert space, the semi-analytic nature of such variational approaches allows for calculation of $A(\mu)$ in the thermodynamic limit (see Appendix 5.1).

The last step consists of projecting the rotated Hamiltonian to the subspace. Given a projector on the subspace as $\mathcal{P} = \sum_{p\in\mathcal{P}} |p\rangle\langle p|$, computing $H_{\text{eff}} = \mathcal{P}\tilde{H}\mathcal{P}$ amounts to computing the matrix elements of the Hamiltonian $\tilde{H}$ between the

states within the subspace P since $\langle p|\tilde{H}_{\text{eff}}(\lambda)|p'\rangle = \langle p|\tilde{H}\,(\lambda)|p'\rangle$, p, $p' \in P$. Similarly one can compute the matrix elements of all other observables. This procedure is feasible if the basis elements are well defined: for example, all elements in some symmetry sector, or low-energy eigenstates of an integrable model.

Method implementation

Before illustrating the power of our approach we will summarize its implementation step by step.

The abbreviated method is as follows: First, Find approximate generators along the range of $\mu \in [0,\, \lambda]$ by minimizing the Hilbert-Schmidt tracenorm of Eq. (5.13) for $A(\mu)$ constructed within a given (local) operator basis (see Refs. (Sels and Polkovnikov, 2017; Claeys et al., 2019) and discussion below for examples of possible basis choices).

Next, compute rotated operators $\tilde{\mathcal{O}} \equiv \tilde{\mathcal{O}}(\lambda) = U^\dagger(\lambda)\mathcal{O}U(\lambda)$ including the Hamiltonian $H = H_0 + \lambda V$ and observables. This may be done efficiently by computing Heisenberg evolution of some intermediary operator $Q(\mu) = U(\mu)U^\dagger(\lambda)\mathcal{O}U(\lambda)U(\mu)^\dagger$, which satisfies the following equation of motion:

$$\partial_\mu Q(\mu) = i[Q(\mu), A(\mu)]. \tag{5.23}$$

By construction, $Q(\lambda) = \mathcal{O}$ as $UU^\dagger = \mathbb{1}$, and $Q(0) = \tilde{O}$ as $U(0) = \mathbb{1}$. Thus, this evolution should be propagated starting at $\mu = \lambda$ and evolving from $\mathcal{Q}(\lambda) = \mathcal{O}$ to $Q(0) = \tilde{\mathcal{O}}$. Critically, because the generator is local by construction, this evolution can be performed efficiently by taking advantage of locality as detailed below.

Next, find the effective Hamiltonian H_{eff} by evaluating the matrix elements of

$\tilde{H}$ in the original (unrotated) basis of P

$$\langle p|\tilde{H}_{\text{eff}}|p'\rangle \equiv \langle p|\tilde{H}|p'\rangle,$$

for all states $p, p' \in P$. Diagonalizing $\tilde{H}_{\text{eff}}$ will automatically generate the spectrum of the Hamiltonian within the dressed subspace $\tilde{P}$. If the latter stands for the low-energy sector, then this diagonalization yields approximate (dressed) eigenstates and eigenenergies of the ground state and low-energy excitations of H.

For describing quenches, i.e. a time-independent Hamiltonian starting from the initial state $|\psi\rangle$ belonging to the dressed subspace $\tilde{P}$, the rotated initial state is obtained by solving the Schrödinger equation again backwards in μ: $i\partial_\mu|\Psi(\mu)\rangle = A(\mu)|\Psi(\mu)\rangle$ from $\mu = \lambda$ to $\mu = 0$, with $|\Psi(\lambda)\rangle = |\psi\rangle$ and $|\Psi(0)\rangle = |\tilde{\psi}\rangle$. This evolution can be calculated using e.g. Krylov methods or matrix product states (Haegeman et al., 2011), as it requires evolution in the full Hilbert space *before* projecting to the subspace.

Time evolution of the observable $\mathcal{O}$ can now be calculated within the subspace $\tilde{P}$ by first evolving the wave function $|\tilde{\psi}(0)\rangle = |\tilde{\psi}\rangle$ with the Hamiltonian $\tilde{H}_{\text{eff}}$, leading to the time dependent state $|\tilde{\psi}(t)\rangle$ as $|\tilde{\psi}(t)\rangle = \exp[-i\tilde{H}_{\text{eff}}t]|\tilde{\psi}(0)\rangle$, and second computing the expectation values of rotated observables such that $\langle\psi(t)|\mathcal{O}|\psi(t)\rangle \approx \langle\tilde{\psi}(t)|\tilde{\mathcal{O}}|\tilde{\psi}(t)\rangle$. If the initial state $|\psi\rangle$ *does not* belong to a single subspace $\tilde{P}$ then one has to first project this state into different subspaces $\tilde{P}_1, \tilde{P}_2, \ldots$ and then evolve it separately in each subspace together with each subspace's effective Hamiltonian and observables. Because the Hamiltonian $\tilde{H}$ is approximately block diagonal, the wave function in each subspace evolves in time independently.

Generating the transformed Hamiltonian

One of the numerical challenges is computing the rotated Hamiltonian $\tilde{H}$ and associated wavefunctions and observables. The evolution of the operators is written as

$$\partial_\mu Q(\mu) = i[Q(\mu), A(\mu)] \tag{5.24}$$

The challenge is, of course, in implementing this evolution. There are several ways.

- **Matrix Product Operators**. Because the rotated operator is quasi-local, one may do time-evolution of operators under a matrix product operator ansatz with a reasonably small bond dimension.
- **Krylov Subspaces**. Using super-operator formalism one may evolve operators in a subspace, which amounts to a low-order resummation of a Baker-Campbell-Hausdorff expansion (Viswanath and Müller, 2008).
- **Exact Evolution on small systems**. If the evolution length is small enough, an exact evolution can be done for a smaller system, then expanded. This is the method used in this work. As such, more details are given below.

The translationally-invariant operator $\tilde{H}$ is computed in the following way. First, pick the translationally-invariant terms (say, the hopping $\sigma_x^i \sigma_x^{i+1}$) and act with them on two center spins of (nominally) 12 spins as some dense $2^{12} \times 2^{12}$ operator. Then, implement time evolution of Eq. (5.23) to find the $2^{12} \times 2^{12}$ dense operator representing $\tilde{H}$. Next, compute the decomposition of $\tilde{H}$ into Pauli matrices via traces, using the identity

$$\tilde{H} = \frac{1}{2^N} \sum_{\{\alpha\}} \mathrm{Tr}\big[\sigma_\alpha^i \tilde{H}\big] \sigma_\alpha^i + \mathrm{Tr}\big[\sigma_\alpha^i \sigma_\beta^j \tilde{H}\big] \sigma_\alpha^i \sigma_\beta^j + \ldots \tag{5.25}$$

Here the summation runs over all of the 4^N combinations of the Pauli matrices, which form a complete, trace-orthogonal operator basis. Because the operator $\tilde{H}$ is known to be quasi-local, one would expect most of the contributing Pauli operator strings to only have a few operators: because of this, using a sub-basis of all Pauli operator strings of extent less then, say, 5 sites captures $\tilde{H}$ almost exactly.

With this set of translationally-invariant operators in hand, it is simple to replicate across the larger system: the m operators of the rotated translationally invariant term becomes mN operators across N sites. Similar challenges exists in computing the rotated wave function $|\tilde{\psi}\rangle = \mathcal{P}U^\dagger|\psi\rangle$, as one must rotate *then* project. For this work, evolution was done via a Krylov subspace on sparse vectors.

5.2 Methodology: Adiabatic continuation / Schrödinger picture

One can also use the approximate AGP to compute approximate eigenstates, in the same manner of the exact AGP computing exact eigenstates. First, choose some set of $\mathcal{D}_p$ states $\{|q\rangle\}$ of the exactly solvable Hamiltonian $H(0)$. This choice depends on the system at hand. One choice could be, for example, all eigenstates below some energy cutoff. Another choice would be all states within some particular symmetry sector such as fixed particle number, which form a subset of eigenstates not necessarily sorted by energy. The set of states forms some projective subspace P with projector $\mathcal{P} = \sum_q |q\rangle\langle q|$.

Approximate eigenstates of the interacting model $H(1)$ can be computed by "dressing" each state via Schrödinger evolution with repect to the AGP (eg eq. (5.11)). This equivalently implements the unitary of Eq. (5.7) to get some set of "dressed" states $\{|q(1)\rangle\} \equiv \{U|q\rangle\}$.

As a comment on implementation, care must be taken in the direction of evolution: the AGP is parameter dependent so generally $A(1) \neq A(0)$. For perturbative couplings this parameter dependence is very weak so that the AGP approximately commutes with itself for all μ and the directionality doesn't matter; however strong coupling may lead to nonsensical answers. One may start by accidentally acting on a non-interacting wavefunction with the AGP from the interacting point, which may be much different than the correct non-interacting AGP.

An effective Hamiltonian within that subspace can be computed via matrix elements in the dressed subspace:

$$\left(H_{\text{eff}}\right)^{pq} = \langle p(1)|H(1)|q(1)\rangle = \langle p|U^\dagger H(1)U|q\rangle. \tag{5.26}$$

Note that this is equivalent to computing the effective Schrieffer-Wolff Hamiltonian where one rotates the operator $\tilde{H} = U^\dagger H(1)U$ instead of the states. If the AGP is exact, this effective Hamiltonian will be exactly diagonal. However, if the AGP is not exact or the initial subspace was a degenerate symmetry sector, the effective Hamiltonian will not be diagonal. One can then compute the eigensystem of the $\mathcal{D}_p \times \mathcal{D}_p$ matrix via standard linear algebra techniques to find eigenenergies E_i and eigenvectors V_i such that

$$\left(H_{\text{eff}}\right)^{nm} V_{mi} = E_i V_{ni}. \tag{5.27}$$

The approximate eigenvectors of the system are then given by

$$|E_i\rangle = \sum_q V_{qi}|q(1)\rangle \tag{5.28}$$

with eigenvalues E_i. This final step is functionally equivalent to the truncated

spectrum Approach (TSA) (James et al., 2017), except instead of using a non-interacting subspace P, the subspace is first rotated by the approximate AGP to obtain some improved subspace $\tilde{P}$. This basis better resembles eigenvectors of the interacting system, and may be exponentially orthogonal from the original basis due to the finite rotation. This corresponds to a *rotated* truncated spectrum approach (rTSA)

The abbreviated method is as follows:

1. Define some Hamiltonian $H(\mu)$, with $H(0)$ being exactly solvable and $H(1)$ being a system of interest, with some path in parameter space linking the two.

2. Given some ansatz, compute a variational adiabatic gauge potential $A(\mu)$ along the points $\mu \in [0, 1]$.

3. Define some set of eigenstates of $H(0)$, either within some energy window or within some symmetry sector(s) such as particle number.

4. Evolve the set of states via the Schrödinger equation from $\mu = 0$ to $\mu = 1$ with the variational AGP.

5. Compute the effective Hamiltonian and its eigensystem to find approximate eigenstates and eigenvalues.

Error analysis

The eigenstates computed in this manner are approximate, in that they are not exact eigenstates of the Hamiltonian $H(1)$. The simplest indicator of the closeness to an exact eigenstate is the energy variance of the state

$$\Delta_n^2 \equiv \langle E_n|H^2|E_n\rangle - \left|\langle E_n|H|E_n\rangle\right|^2. \tag{5.29}$$

Exact eigenstates have zero energy variance, and so approximate eigenstates should have minimal energy variance $\Delta_n^2 \approx 0$. The average energy variance of these eigenstates within the subblock corresponds to the average block-off-diagonal matrix elements in the Hamiltonian and thus indicates the performance of the block diagonalization procedure. When computing an effective Hamiltonian within a rotated subspace, the procedure is an analogous one to a Schrieffer-Wolff transformation: a unitary rotation block diagonalizes some Hamiltonian into a subspace P and complement Q. A measure of the quality of this diagonalization is the average strength of the off-diagonal elements: zero strength means exact block diagonalization, while nonzero strength means approximate diagonalization. The average energy variance is defined as

$$\Gamma^2 = \frac{1}{\mathcal{D}_P}\sum_n^p \langle E_n|H^2|E_n\rangle - \Big(\langle E_n|H|E_n\rangle\Big)^2, \tag{5.30}$$

$$\Gamma^2 = \frac{1}{\mathcal{D}_P}\sum_n^p \langle E_n|H\Big(|q\rangle\langle q| + |E_{p'}\rangle\langle E_{p'}|\Big)H|E_p\rangle - \Big(\langle E_n|H|E_n\rangle\Big)^2, \tag{5.31}$$

$$\Gamma^2 = \frac{1}{\mathcal{D}_P}\sum_{nq} \Big|\langle E_n|H|q\rangle\Big|^2. \tag{5.32}$$

Step 2 inserts the identity, for complete set of states $|q\rangle \in Q$, and complete set of states $|E_p\rangle \in P$, while step 3 simplifies using the fact that $|E_n\rangle$ are eigenstates of the effective Hamiltonian within subspace P. Because $|E_n\rangle$ is a complete set of states in P and similarly for Q, the sum is then over all off-block-diagonal matrix elements, giving an average off diagonal strength.

Connection with Wegner flow, perturbative SW transformations, and Floquet systems

As mentioned previously, it was recently argued by some of us that an accurate approximation to $A(\mu)$ can be found through a commutator expansion (Claeys et al., 2019):

$$A(\mu, \{a\}) = i \sum_{k=1}^{\ell} a_k \underbrace{[H(\mu), [H(\mu), \ldots [H(\mu)}_{2k-1}, V]]], \tag{5.33}$$

where $\{a\} = \{a_1, a_2, \ldots, a_\ell\}$ follows from the variational minimization. Truncating this expansion to a single commutator level ($\ell = 1$), we get

$$\partial_\mu H(\mu) = i a_1 [[H, V], H]. \tag{5.34}$$

This equation is highly reminiscent of the Wegner flow (Kehrein, 2006) (also known as the similarity renormalization group (Szpigel and Perry, 2000)), where a flow equation is constructed for the Hamiltonian as $\partial_s H(s) = [\eta(s), H(s)]$, with the goal of obtaining a diagonal matrix for $s \to \infty$. A commonly-used generator is given by $[H(s), V(s)]$, where V is the off-diagonal part of $H(s)$. This flow systematically suppresses off-diagonal elements of $H(s)$ in the same vein as the Schrieffer-Wolff generator, and it can be seen that a similar equation can be obtained by rescaling μ by a_1, with the crucial difference that the flow equation for the SW transformation only ranges in the interval $\mu \in [0, \lambda]$, whereas the Wegner flow necessitates the limit $s \to \infty$. This observation then also suggests that convergence of the Wegner flow may be improved by adding higher-order variationally-optimized commutators to the flow generator.

Finally, we point out that the standard perturbative SW transformation is obtained when we approximate $U \approx \exp[-i\lambda A(0)]$, where $A(0)$ is the solution of

Eq. (5.13) at $\lambda = 0$, which simplifies to

$$[V + i[A(0), H_0], H_0] = 0. \tag{5.35}$$

This equation is exactly the one to be solved for defining the leading order in standard Schrieffer-Wolff transformation (Bravyi et al., 2011). Note that in some cases it is also possible to go to higher-orders of the perturbation in SW theory, which is equivalent to the van Vleck high-frequency expansion of the rotating frame Floquet Hamiltonian (Bukov et al., 2016). Then it is possible to systematically develop perturbation theory for the generator of the SW transformation.

In general, a Floquet problem can be mapped to a time-independent problem by coupling to a static Hamiltonian to a bosonic photon mode (Cohen-Tannoudji et al., 1998), then going to the rotating frame. By applying these variational transformations to this setup, one may compute effective local Floquet Hamiltonians which decouple from the bosonic mode. This is a topic of recent interest, especially if one considers prethermalization and emergent integrals of motion (Abanin et al., 2017; Ho et al., 2018; Haldar et al., 2018; Haldar et al., 2019; Luitz et al., 2019) in such periodically-driven systems.

Example

For an explicit example where the first-order commutator expansion is exact, let us choose a Hamiltonian as in Fig. 5·1,

$$H = H_0 + \lambda(V_+ + V_-), \quad V_+^\dagger = V_-, \tag{5.36}$$

where H_0 consists of degenerate levels separated by Ω, and $V_\pm$ acting on an eigenstate of H_0 can only change the energy by $\pm\Omega$. This requirement leads to commu-

tation relations $[H_0, V_\pm] = \pm\Omega V_\pm$. While such a model might seem somewhat artificial, such Hamiltonians are commonly encountered in Floquet systems (Bukov et al., 2019) and standard SW transformations (see e.g. the Fermi-Hubbard model below).

Considering the expansion from Eq. (5.33) and keeping only the first-order term leads to

$$A(\mu) = ia_1(\mu)[H, V] = ia_1(\mu)\Omega\big(V_+ - V_-\big). \tag{5.37}$$

Plugging this equation in the variational minimization for $\mu = 0$ results in finding the minimum of

$$\begin{aligned} &\mathrm{Tr}\big[(V_+ + V_- - a_1(0)\Omega[V_+ - V_-, H_0])^2\big] \\ &\quad = (1 + a_1(0)\Omega^2)^2 \mathrm{Tr}\big[(V_+ + V_-)^2\big]. \end{aligned} \tag{5.38}$$

This expression is exactly zero when $a_1(0) = -1/\Omega^2$, leading to $A(0) = -i(V_+ - V_-)/\Omega$. For small λ/Ω the rotation can be expanded up to $\mathcal{O}(\lambda^2)$ to return

$$U^\dagger H U \approx H + [A, H] + \frac{1}{2}\big[A, [A, H]\big] \tag{5.39}$$

$$= H_0 - \frac{\lambda^2}{\Omega}\big[V_+, V_-\big]. \tag{5.40}$$

The first commutator exactly cancels the perturbative term, yielding a new Hamiltonian which is block-diagonal in the eigenbasis of H_0 up to $\mathcal{O}(\lambda^2)$, returning the standard SW results. In order to go beyond these results, it is possible to retain the higher-order terms in the commutator expansion and perform the rotation in a more involved way, which is precisely explained below for specific models.

In general, the critical parts of the variational commutator expansion are twofold. First, the magnitude of the rotation is controlled by the size of gaps Ω in the system, but does not necessarily require any additional structure in the

original Hamiltonian: for example, it could have a varying Hilbert subspace size, not have exact gap differences, or not be degenerate within each subspace. These are significant relaxations on traditional Schrieffer-Wolff transformations, which normally require exact degeneracies in order to be feasible.

The second advantage of these expansions is that it is by nature local; the n-th order term of the expansion will have operator support on the order of n sites. This means, for order-1 parameter λ/Ω, the rotated wave function $|\tilde{\psi}\rangle$ is only entangled within some finite support and the Hamiltonian $\tilde{H}$ is similarly quasi-local, due to locality of $A(\mu)$ and bounded evolution "time" in the λ-space. With this observation in hand, existing methods which take advantage of locality may be readily applied to extract the basis-rotated objects, as also detailed in Appendix 5.1.

In the perturbative limit for large gaps $\lambda/\Omega \ll 1$, the variational ansatz is asymptotically exact, as shown in this example. However, nothing is preventing larger, non-perturbative couplings from nonetheless having an accurate block-diagonalization procedure, even when the gaps Ω close or are non-existent. This is because the accuracy is controlled by the locality of the variational ansatz: if eigenstates within the subspace only mix within a small spatial region, then they should be well-captured. Thus, one should anticipate that local dressing should, for example, work well for if the system is far from singularities and phase transitions.

5.3 The Fermi-Hubbard model

A classic example to apply the proposed method to is the attractive Fermi-Hubbard model, where the perturbative Schrieffer-Wolff transformation returns the well-known Heisenberg model (Hubbard, 1963; Shastry, 1986b; Shastry, 1986a).

Here, this model will be used to illustrate the non-perturbative nature of the variationally-obtained rotations, which allows for effective dynamics at values of λ/Ω where the perturbative SW transformation is no longer expected to return accurate results. The disordered Fermi-Hubbard Hamiltonian is given by

$$H = -\Omega \sum_i \left(n_{i,\uparrow} - \frac{1}{2}\right)\left(n_{i,\downarrow} - \frac{1}{2}\right) + \sum_i \delta_{i\sigma} n_{i,\sigma} + \lambda \sum_{i,\sigma} \left(c^\dagger_{i,\sigma} c_{i+1,\sigma} - h.c.\right), \tag{5.41}$$

in which $n_{i,\sigma} = c^\dagger_{i,\sigma} c_{i,\sigma}$ and δ_i are independent random numbers, which are drawn from a normal distribution with variance $\lambda^2\Delta/2\Omega$. The factor $\lambda^2/2\Omega$ is such that the crossover from weak to strong disorder regimes in the effective Heisenberg model happens at $\Delta \sim 1$. For N sites, there are of the order of 4^N degrees of freedom, with 4 possible fermion states for each site $\{|0\rangle, |\uparrow\rangle, |\downarrow\rangle, |\uparrow\downarrow\rangle \equiv |2\rangle\}$.

Given the expansion from the $\lambda = 0$ point we choose H_0 to be the Hubbard interaction and disorder term and V to be the nearest-neighbor hopping terms. Notice that the disorder breaks the otherwise massive degeneracy of the unperturbed Hamiltonian H_0. The hopping can change energy of H_0 by either $\pm\Omega$ if it corresponds to changing the number of singly occupied sites (spinons), or by 0 if it conserves this number. For this reason the Fermi-Hubbard model is a more complicated version of the Hamiltonian (5.36), though it shares many of its features. We choose the commutator expansion (5.33) to get the first two basis operators of the variational gauge potential

$$A(\mu) = i a_0(\mu)[H(\mu), V] + i a_1(\mu)\big[H(\mu), \big[H(\mu), [H(\mu), V]\big]\big]. \tag{5.42}$$

Due to the local structure of the Hamiltonian, this approximate generator is also local, constrained to operators with span of 4 sites or less. Specifically, the first

commutator has 12 terms per site and appears as

$$[H(\mu), V] = \sum_{i,\sigma} \left(\frac{\delta_i}{\Omega} + n_{i,\bar{\sigma}} - n_{i+1,\bar{\sigma}} \right) \times \left(c^\dagger_{i,\sigma} c_{i+1,\sigma} + c_{i,\sigma} c^\dagger_{i+1,\sigma} \right). \tag{5.43}$$

The second commutator has 144 terms per site, which is intractable to write down and solve by hand; instead we turn the computer to calculate the commutators.

Next, we minimize the norm in Eq. (5.22) within the operator space spanned by these two commutators, which is equivalent to inversion of a 2×2 matrix to get a variational approximation of $A(\mu)$. We choose to compute the AGP in the disorder-free case for computational simplicity, and apply it to the disordered Hamiltonian. While this may generate some error at large disorder, it is suppressed by powers of at least $(\lambda/\Omega)^3$: two orders from the base disorder strength of $\Delta\lambda^2/\Omega$, an additional power stemming from the fact that the unrotated operator is still block-diagonal. We checked numerically that in the analyzed regimes the variational gauge potential does not change significantly when computed with vs. without disorder and this difference only slightly affects the results presented below [1].

Let us start in the perturbative regime $\lambda/\Omega \ll 1$. Here, one may compute the AGP in powers of μ as $A(\mu) = A_0 + \mu A_1$. Then we can reduce the generator of the SW rotation to a "time"-independent operator via a Magnus expansion (Blanes et al., 2009)

$$\mathcal{T} \exp \left(i \int_0^\lambda A(\mu) d\mu \right) \approx \exp \left(i\lambda A_0 + i \frac{\lambda^2}{2} A_1 + \mathcal{O}(\lambda^3) \right). \tag{5.44}$$

[1] For $\Omega/\lambda = 7.5$, 6 sites, and $\Delta = 10$ the operator norm of the difference between the AGP computed with and without disorder is $||dA|| \approx 0.05||A||$. The wave-function fidelity of a Néel state is changed by less then 0.5%.

The rotated Hamiltonian can then be computed via a second-order BCH expansion (Griffiths, 2005), keeping terms up to order λ^2

$$\begin{aligned}\tilde{H} = &-\Omega \sum_i \left(n_{i,\uparrow} - \frac{1}{2}\right)\left(n_{i,\downarrow} - \frac{1}{2}\right) + \delta_i(n_{i,\uparrow} + n_{i,\downarrow}) \\ &+\lambda \sum_{i,\sigma} \left(1 - (n_{i+1,\bar{\sigma}} - n_{i,\bar{\sigma}})^2\right)\left(c^\dagger_{i,\sigma} c_{i+1,\sigma} - c_{i,\sigma} c^\dagger_{i+1,\sigma}\right) \\ &-\frac{\lambda^2}{\Omega} \sum_{i,\sigma} (c_{i,\sigma} c_{i,\bar{\sigma}})(c^\dagger_{i+1,\sigma} c^\dagger_{i+1,\bar{\sigma}}) + \text{c.c.} \\ &+\frac{\lambda^2}{\Omega} \sum_{i,\sigma} (c_{i,\sigma} c^\dagger_{i,\bar{\sigma}})(c^\dagger_{i+1,\sigma} c_{i+1,\bar{\sigma}}) + \text{c.c.} \\ &+\frac{\lambda^2}{\Omega} \sum_{i\sigma} (1 - 2n_{i,\bar{\sigma}})(1 - 2n_{i+1,\sigma}).\end{aligned}$$

Here, the blocks diagonalizing the leading order-Ω term define the subspaces, while the order-λ term describes hopping of spinons and doublons: the $1-(n_{i+1,\bar{\sigma}}-n_{i,\bar{\sigma}})^2$ term suppresses hopping between states belonging to different subspaces. The order-λ^2/Ω terms describe either the double hopping between adjacent sites (the third term) or spin exchange between adjacent spinons (fourth term).

This Hamiltonian still acts on the full Hilbert space but it is block diagonal up to λ^2/Ω. For this reason the projective subspace P can be chosen to be any sector of fixed number of singly-occupied sites (spinons). One such choice is that of no singly occupied sites, which corresponds to the lowest-energy subspace for $\Omega > 0$. The Hamiltonian confined to this subspace can be in turn mapped to a spin Hamiltonian by identifying $|0\rangle \to |\Downarrow\rangle$ and $|2\rangle \to |\Uparrow\rangle$, as well as operators $(c_{i,\sigma} c_{i,\bar{\sigma}}) \to \sigma_i^-$ and so forth. The effective Hamiltonian in this subspace is then given by the Heisenberg model.

In general, the subspace P does not necessarily need to be the lowest-energy subspace, just one of the energy blocks of H_0. In this way, one may compute

the effective Hamiltonian with any number of spinons as well. Note that in those sectors the hopping term will be non-zero and thus the time evolution there will be dominated by a timescale λ corresponding to spinon hopping. Because the rotated Hamiltonian is block-diagonal, each subsector can be time-evolved independently.

The above derivation was perturbative, in that the rotation was computed using a perturbative BCH expansion, which requires careful power-counting. It comes as no surprise that it is asymptotically exact in the limit $\lambda/\Omega \to 0$: the hopping terms raise or lower the energy by $\pm\Omega$, and so this model is a more explicit version of the example (5.36). In principle, one could go to higher orders of perturbation theory or SW to compute corrections, but in practice it becomes unwieldy. Instead, this same process can be applied for finite λ by computing the generator $A(\mu)$ at each step μ variationally, then computing the rotated operators numerically. These numerical computations take advantage of the fact that the generator is local. In this way, the only error comes from the variational approximation for the gauge potential, whose validity can be found by increasing the variational ansatz size.

Quench Dynamics of the Fermi Hubbard Model

We will now analyze quench dynamics of the Fermi-Hubbard model starting from Néel and boundary-wall initial states. We choose the subspace P as the space containing no singly-occupied sites, and thus would recover the Heisenberg model for $\lambda \to 0$.

In Fig. 5·3 we show a comparison of the fermion imbalance computed by a variationally-projected model, the perturbative Schrieffer-Wolff model, i.e. the Heisenberg model with disorder, and the original Hubbard model, for a small system of 8 sites. The initial condition is chosen to be a Néel state of doubly-

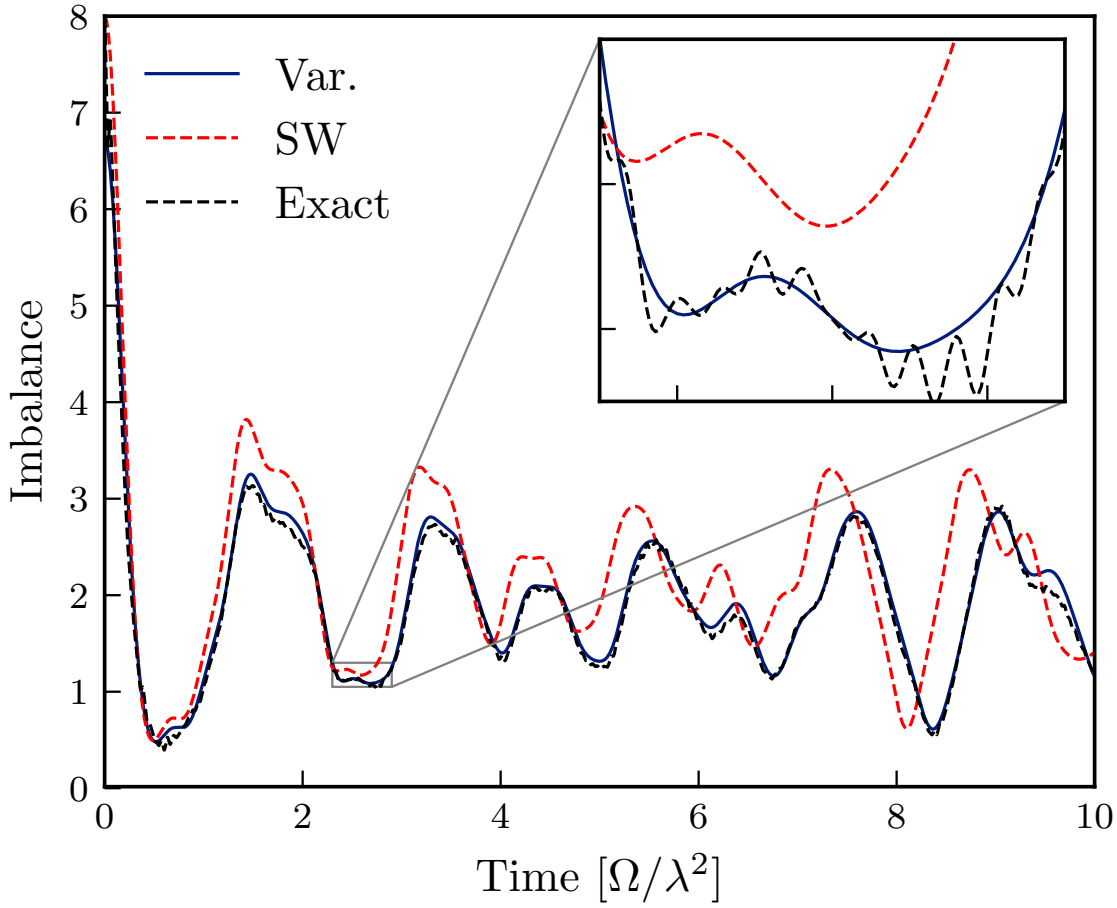

Figure 5·3: Comparing exact (black dashed line), projected variational (blue solid line), and perturbative SW (red dashed line) dynamics of the Fermi-Hubbard model. Here, the system size is 8 fermionic sites, $\Omega/\lambda = 5.0$ and a single disorder realization of strength $\Delta = 2.5$. The initial condition is a Néel state of alternating doubly-occupied and non-occupied sites, with periodic boundary conditions. Inset details how the projected dynamics miss high-frequency oscillations.

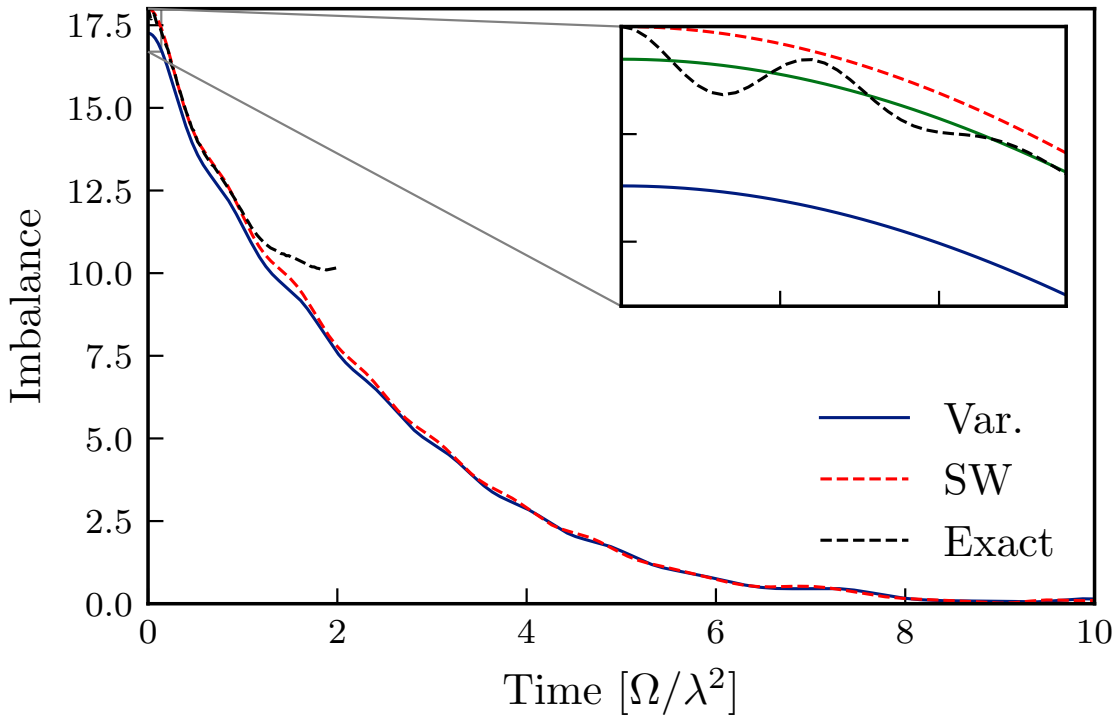

Figure 5·4: Comparison of exact and projected dynamics of the Fermi-Hubbard model for a large system of 18 fermionic sites. This is beyond the reach of exact dynamics, with $\Omega/\lambda = 5$ and a boundary-wall initial condition. The black dashed line represents exact results for a small system of 8 sites, where finite-size effects occur after a time of order 2. Error at time $t = 0$ is due to missing overlap w.r.t. higher-energy sectors. This can be seen from the green line in the inset, representing the variational results renormalized by the fidelity of the projected initial state as $\langle \tilde{O}(t) \rangle / \langle \tilde{\mathcal{P}} \rangle$.

occupied sites $|\psi(0)\rangle = |20202020\rangle$. The Hamiltonian is chosen to have the ratio of the Hubbard interaction and the hopping $\Omega/\lambda = 5$ and disorder strength $\Delta = 2.5$. We calculate the density imbalance as the expectation value of $\mathcal{I} = \sum_{i,\sigma}(-1)^i n_{i,\sigma}$, which is extremal at $t = 0$ and is expected to vanish if the system thermalizes.

To demonstrate applicability of the method to go well beyond system sizes amenable to exact diagonalization, in Fig. 5·4 we show the imbalance for a quench from a domain wall initial condition of 18 sites for $\Omega/\lambda = 5$ and zero disorder, where

$$|\psi(0)\rangle = |222222222000000000\rangle. \tag{5.45}$$

Computing the exact time evolution requires access to approximately 4^{18} degrees of freedom (36 qubits), which is on the edge of computational feasibility, although variational methods such as DMRG may perform well. For this plot and initial state the relevant imbalance is defined as $\mathcal{I} = \sum_{i=1}^{9} n_i - \sum_{i=10}^{18} n_i$, again maximal at the initial time $t = 0$ and vanishing in time as the system thermalizes and the boundary wall dissolves.

The results illustrated in Figs. 5·3 and 5·4 highlight two important aspects of the method. Fig. 5·3 demonstrates that the method can be used to go beyond standard perturbative SW transformations and give a systematic and significant improvement to the perturbative results. At the same time Fig. 5·4 shows that the domain wall dynamics is very accurately described by the Heisenberg model, even in the regime where such an accuracy might not be anticipated. As can be seen from the inset of Fig. 5·3 the variational method accurately reproduces the low-frequency behavior, while failing to reproduce the high-frequency oscillations. These high-frequency oscillations originate from the fact that the dynamics follow a sudden quench, which excites the initial wave function beyond the lowest block.

A more realistic and experimentally relevant situation is a gradual ramp of the coupling, which might be still fast with respect to the effective low-energy degrees of freedom, but slow with respect to the scale Ω. These high-frequency oscillations are then expected to be strongly suppressed. In order to reproduce these fast oscillations within our scheme one needs to add evolution coming from other blocks, which can be done in parallel and hence does not significantly increase the complexity of the computation.

Wave function fidelity

The quench effects also lead to a small mistake in the imbalance for an initial domain wall state even at the initial time, as illustrated in the inset of Fig. 5·4. As we explained above this happens because the wave function needs first be rotated, and then projected into the subspace; the rotation can result in a nonzero projection of the rotated wave function $|\tilde{\psi}\rangle$ to other subspaces even if the unrotated state $|\psi\rangle$ is fully contained in P. Mathematically this can be expressed in the partial loss of fidelity of the rotated wave function

$$\langle\psi|U\mathcal{P}U^{\dagger}|\psi\rangle = \langle\tilde{\psi}|\mathcal{P}|\tilde{\psi}\rangle = \langle\psi|\tilde{\mathcal{P}}|\psi\rangle \leq 1. \tag{5.46}$$

The subspace P contains the lowest-energy eigenstates of the *non-interacting* model, including the Néel and boundary wall states. However, the subspace $\tilde{P}$ can be seen as the lowest-energy eigenstates of the *interacting* model, which may include mixed spin-charge degrees of freedom. Equivalently, a quench can be seen as injecting some finite energy density into the system, such that there must be some overlap with higher-energy sectors with some finite number of defects (spinons or doublons), which would be indicated here as a wavefunction fidelity less than one.

This loss can be recovered by adding extra subspaces P_i and evolving each

independently, then resumming observables within each subspace:

$$\langle O(t)\rangle \approx \langle\tilde{\psi}(t)|\tilde{O}|\tilde{\psi}(t)\rangle + \sum_n \langle\tilde{\psi}_n(t)|\tilde{O}_n|\tilde{\psi}_n(t)\rangle, \tag{5.47}$$

where the index n denotes the wave function or operator within the higher subspaces n. For Néel/boundary wall quenches, these higher subspaces correspond to $2n$ singly-occupied sites.

The fidelity in the lowest energy sector can be well-described as the probability of having zero defects in the system. In the dilute limit these defects appear with independent probabilities $\rho(\lambda/\Omega)$ such that,

$$\left|\langle\tilde{\psi}|\mathcal{P}|\tilde{\psi}\rangle\right| \approx \Big(1-\rho(\lambda/\Omega)\Big)^n, \tag{5.48}$$

We numerically checked that for the initial Néel state $\rho(x)$ is well fitted by $\rho(x) \approx \frac{x^2}{2} - \frac{3x^4}{2} + \mathcal{O}(x^6)$ [2]. For $\Omega/\lambda = 5$ this expression gives $\rho \approx 0.017$, i.e. approximately 1.7% chance of exciting a spinon pair per site. The fidelity is thus exponentially suppressed in the system size, and thus a better thermodynamic description would generally correspond to a sector with a small, finite density of spinons. Vanishing fidelity in the thermodynamic limit is of course related to the well-known orthogonality catastrophe (Anderson, 1967), which is often easy to forget about especially if the perturbative limit $\Omega/\lambda \to \infty$ is taken before the thermodynamic limit $N \to \infty$. In passing, we comment that this dressing may have similarities to polarons (Grusdt et al., 2018; Koepsell et al., 2019), which are particle excitations dressed by spin degrees of freedom through interactions. The rotation U may serve the same purpose of dressing such purely particle excitations.

[2] This functional form is changed slightly by computing the AGP with disorder

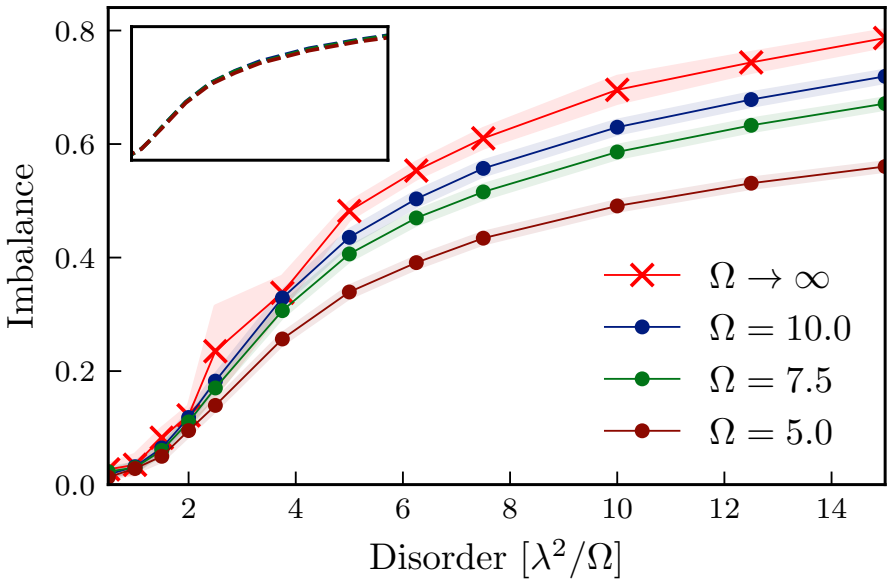

(a) System of 18 fermionic sites and varying disorder and Ω. Inset is the imbalance rescaled by the fidelity, collapsing all lines to the $\Omega \to \infty$ result and indicating that the loss is due to overlap with thermalizing finite-spinon sectors.

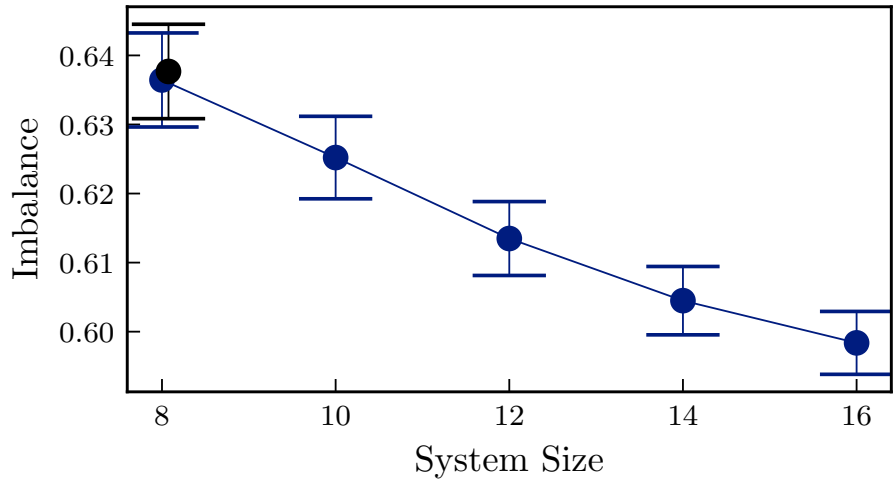

Figure 5·5: Steady-state imbalance for a disordered Fermi-Hubbard model. The initial condition is a Néel state of alternating doubly-occupied and non-occupied sites with periodic boundary conditions, and is computed at time $t = 25\Omega^2/\lambda$. The imbalance decreases with decreasing Ω and increasing system size, mainly due to fidelity loss. Here, disordier is fixed at $\Delta = 10$ and $\lambda/\Omega = 7.5$. Small system sizes are consistent with exact results (black).

Many-body localization at finite Ω

We will now apply this method to analyze the effects of onsite disorder on the Fermi-Hubbard model. In the $\Omega \to \infty$ Heisenberg limit, it is widely believed that the model exhibits a many-body localization (MBL) transition indicated by long-time memory of initial conditions and lack of conductivity in equilibrium (Gopalakrishnan et al., 2015; Agarwal et al., 2015). The situation becomes much less clear when the ratio λ/Ω becomes finite and the mapping to the Heisenberg model starts to break down. In Fig. 5·5a, we present the results of simulations of the long-time ($t = 25\Omega^2/\lambda$) imbalance of an 18-site Hubbard chain with the Néel initial condition as a function of the disorder Δ and different ratios of Ω/λ. Here a nonzero long-time value of the imbalance is an indicator of localization (Bordia et al., 2016; Abanin et al., 2019). Note that the disorder strength in the Hubbard Hamiltonian is appropriately rescaled by a factor λ^2/Ω (c.f. Eq. (5.41)). As can be clearly seen, for smaller values of Ω/λ the late-time imbalance decreases, which can be heuristically explained by proliferation of spinons at smaller values Ω/λ. The spinons hop at a much faster time scale than the spin exchange, allowing the otherwise MBL-frozen state to thermalize.

This qualitative reasoning can be quantified using the variational SW method developed here. We can check that the fidelity of the initial 18-site Néel state with the lowest energy subspace is 0.73, 0.86, and 0.92 for $\Omega/\lambda = 5$, 7.5, and 10, respectively, fully consistent with Eq. (5.48). Such relatively small numbers, especially for the lowest analyzed ratio $\Omega/\lambda = 5$, imply that already for the system sizes studied there is a significant fraction of spinons present in the system. On top of that the effective Hamiltonian is also modified slightly: there are longer-range spin-spin interaction terms and emergent weak correlations in the disorder. However, we checked numerically (results are not shown here) that these effects

are small and do not lead to thermalization within the subspace $\tilde{P}$, at least for these system sizes. This was done by computing ZZ time correlation functions within the $\tilde{P}$ sector. At the same time, the late-time imbalance shown in Fig. 5·5a normalized by the fidelity as $\frac{\langle \tilde{O}(t) \rangle}{\langle \tilde{P} \rangle}$ corresponds closely to the $\Omega \to \infty$ case, as shown in the inset of Fig. 5·5a. Thus, the apparent decrease in imbalance is mostly due to projective loss of the wave function to other spinon sectors.

This loss can be compensated by analyzing the dynamics of these sectors and combining these results together. However, it turns out to be unnecessary as free spinons lead to a very rapid decay to zero of the imbalance because their hopping λ is much larger than the disorder strength. Thus the sectors containing free spinons do not affect the long time imbalance as shown in Fig. 5·5a. It can easily be shown that even a single spinon moving on top of a Néel state destroys the magnetic order (Shraiman and Siggia, 1988). For example, as illustrated below a spinon moving from right to left swaps the states $|0\rangle \leftrightarrow |2\rangle$ in the middle

$$|2, 0, 2, \uparrow\rangle \to |2, 0, \uparrow, 2\rangle \to |2, \uparrow, 0, 2\rangle \to |\uparrow, 2, 0, 2\rangle. \tag{5.49}$$

We confirmed these considerations by checking numerically that the higher-defect sectors always thermalize; recent work with a similar setup also shows similar behavior (Krause et al., 2019).

The immediate implication of these observations is on the absence of MBL in the Fermi-Hubbard model. Indeed, for any finite λ/Ω, there will be some density of defects, and the overlap with the zero-defect sector will be exponentially small in the system size, with exponential prefactor λ^2/Ω^2. The zero-defect sector is believed to exhibit MBL behavior in the Heisenberg limit (Nandkishore and Huse, 2015) (with some recent contestation (Suntajs et al., 2019)), which appears to be robust for finite λ/Ω (see above). However, due to inevitable spinon excitations,

the long-time imbalance in the original Hubbard model always goes to zero in the thermodynamic limit. An example of this behavior is shown in Fig. 5·5, where the imbalance is plotted as a function of system size for disorder $\Delta = 10$ and $\Omega/\lambda = 7.5$. The density of spinon excitations and hence the imbalance decay can be reduced by considering a smooth ramps of the hopping strength λ instead of a quench or by going to larger ratios Ω/λ. However, it is virtually impossible to eliminate spinons entirely, and thus care must be taken in finding the overlap of the rotated initial state $|\tilde{\psi}\rangle$ with the zero-spinon subspace.

5.4 The integrability-broken XY model

Another application of the Schrieffer-Wolff transformations we consider here is finding response functions of operators around the ground state $|\emptyset\rangle$ of some Hamiltonian H, such as

$$C_{XY}(t) = \langle\emptyset|X(t)Y(0)|\emptyset\rangle. \tag{5.50}$$

Response functions, and their Fourier-space counterparts structure functions, are fundamental objects describing low-energy excitations such as particles (Sachdev, 2011). For local operators the energy of the wave function $Y|\emptyset\rangle$ is sub-extensive; a low-energy subspace of H suffices to describe the dynamics of this response function as

$$\begin{aligned} C_{XY}(t) &= \langle\emptyset|Xe^{-itH}Y|\emptyset\rangle \\ &\approx \langle\emptyset|X\exp\left(-it\mathcal{N}H\mathcal{N}\right)Y|\emptyset\rangle, \end{aligned} \tag{5.51}$$

where $\mathcal{N}$ is the projection to N low-lying eigenstates of the Hamiltonian H. However, computing these excited states for a generic interacting model is generally intractable, as one must deal with the exponential size of the basis set. As such,

we turn to the Schrieffer-Wolff transformation to find some rotation U to the "$\sim$" basis, and then project the rotated Hamiltonian to a subspace with known analytic properties, avoiding the otherwise exponential complexity of the system. Inserting this rotation $UU^\dagger = \mathbb{1}$ into the above leads to

$$C_{XY}(t) \approx \langle\emptyset|XU \exp\Big(- it\tilde{\mathcal{N}}\tilde{H}\tilde{\mathcal{N}}\Big)U^\dagger Y|\emptyset\rangle.$$

The SW rotation can thus be recognized if a simple low-energy subspace $\mathcal{P}$ is associated with the interacting one as $U^\dagger \mathcal{N} U = \mathcal{P} = \tilde{\mathcal{N}}$. We further define $|\emptyset\rangle = U|\emptyset_0\rangle$, e.g. the interacting ground state rotated from the free basis. It is known that if there is no phase transition between Hamiltonians H and H_0, there exists a quasi-local generator of rotations which maps between these ground states, exactly corresponding to the local gauge potential (Bachmann et al., 2017). The response function can then be approximated as

$$C_{XY}(t) = \langle\emptyset_0|\tilde{X}e^{-it\mathcal{P}\tilde{H}\mathcal{P}}\tilde{Y}|\emptyset_0\rangle, \tag{5.52}$$

with the " $\sim$ " basis being the one generated by rotating using U. As seen previously, for a Hamiltonian $H = H_0 + \lambda V$, the generator can be variationally obtained if the projective subspace are low-energy eigenstates of H_0, written as $\{|n_0\rangle\}$. Explicitly writing this projector as a sum, we find

$$C_{XY}(t) = \sum_{nm}\langle\emptyset_0|\tilde{X}|n_0\rangle\langle m_0|\tilde{Y}|\emptyset_0\rangle \exp\big(- it\langle n_0|\tilde{H}|m_0\rangle\big). \tag{5.53}$$

This is exact in the limit where the generator is the exact gauge potential, or when the subspace is the full space. Thus, the challenge of calculating response functions reduces to two tasks: (i) computing an appropriate generator of rotations, and (ii) computing matrix elements of operators. As argued before, task (i) can be

performed variationally. Task (ii) is implementable, in principle, if the structure of eigenstates are known analytically. This is the case if the Hamiltonian H_0 is integrable and thus the eigenstates are written as particle excitations on top of some vacuum (Faddeev, 1996; Karbach and Muller, 1998). The operators $\tilde{X}$ are quasi-local, as the generator of the rotations is local by the ansatz. This quasi-locality gives some hope of computing the matrix elements analytically, which would allow for the calculation of approximate dynamics even when the Hilbert space of the effective Hamiltonian becomes intractably large.

Thus, this recipe will perform well for the following set of models. Given some integrable Hamiltonian H_0 and an integrability-breaking term V with strength λ, one may compute low-energy excitations of the Hamiltonian $H = H_0 + \lambda V$. One can anticipate that the integrability-breaking terms can even become non-perturbative, as long as the system is relatively far from any phase transition. As an example, let us choose a relatively simple integrable system described by an XY-type model and an additional integrability-breaking term in the form of a longitudinal magnetic field,

$$H = \sum_i J_{xx}\sigma_x^i\sigma_x^{i+1} + J_{yy}\sigma_y^i\sigma_y^{i+1} + h\sigma_z^i + \lambda\sigma_x^i. \tag{5.54}$$

For $\lambda = 0$ this model maps to free fermions under a Jordan-Wigner transformation (Sachdev, 2011). For $J_{yy} = 0$ this is the transverse field Ising (TFI) model, while for $J_{xx} = J_{yy}$ this is the XY model. For $\lambda = 0$ the eigenstates can be written in terms of fermionic raising operators $\gamma_k^\dagger$ acting on some ground state, where each adds one particle of momentum k to the system

$$|k, k', \ldots, k''\rangle = \gamma_k^\dagger\gamma_{k'}^\dagger \ldots \gamma_{k''}^\dagger|\emptyset\rangle. \tag{5.55}$$

The integrability-breaking term $\lambda\sigma_x^i$ in Jordan-Wigner notation can be seen as

coherently adding and removing fermionic excitations from the system; it breaks the conservation laws in the system preserving the number of fermions. It also breaks the $\mathbb{Z}_2$ symmetry, as well as the $U(1)$ symmetry for the XY point. For the following example, let us choose periodic boundary conditions and parameters

$$J_{xx} = J_{yy} = 1,\ h = 3,\ \lambda = 1.25. \tag{5.56}$$

Here, the integrability breaking term is *non-perturbative*, in the sense that it is of the same order as the other terms; there are no symmetries other than geometric ones such as translations, and the model is quantum chaotic (as shown in Appendix A.1). Of course, special eigenstates (Bernien et al., 2017) such as those at the edges of the spectrum can preserve their integrable structure. Let us then proceed by calculating the generator $A(\mu)$ variationally. For this example, we will choose the variational manifold consisting of all operators with support up to three sites:

$$\begin{aligned} A(\mu) &= a_0^i\sigma_x^i + a_1^i\sigma_y^i + a_2^i\sigma_z + \\ &+ a_3^i\sigma_x^i\sigma_y^{i+1} + a_4^i\sigma_y^i\sigma_z^{i+1} + \dots \\ &+ a_5^i\sigma_x^i\sigma_y^{i+1}\sigma_z^{i+2} + a_6^i\sigma_z^i\sigma_y^{i+2}, + \dots \end{aligned} \tag{5.57}$$

where all coefficients a_j are μ-dependent. This anatz gives a variational minimization procedure on $63N$ parameters, which have to be computed in the interval $\mu \in [0, \lambda]$. A further simplification comes from noting that for any real Hamiltonian the AGP is strictly imaginary so only the terms containing an odd number of σ_y matrices are non zero (Sels and Polkovnikov, 2017). Therefore

$$A(\mu) = \sum_i \alpha_1\sigma_y^i + \alpha_2(\sigma_z^i\sigma_y^{i+1} + \sigma_y^i\sigma_z^{i+1}) + \dots, \tag{5.58}$$

where the first term is simply a generator of rotations along the XZ plane, and would be the exact gauge potential in the absence of the spin-spin coupling J. The "..." represents higher-order terms. At large values of h we have $\alpha_1 \sim \lambda/2h$ and $\alpha_2 \sim \lambda J/2h^2$. As such, the magnitude of the rotation is determined by the *energy gap* in the system, as expected. The AGP is translationally invariant: in general a gauge can be chosen such that it obeys all of the symmetries of the Hamiltonian.

The rotated operators and Hamiltonian can be computed efficiently for large systems, because the rotation and operators are all local. The leading terms are as follows

$$\begin{aligned}\tilde{H} =& h_1\sigma_z^i + h_2\sigma_y^i\sigma_y^{i+1} + h_3\sigma_x^i\sigma_x^{i+1} + h_4\sigma_z^i\sigma_z^{i+1} \\ &+ h_5\sigma_x + h_6\sigma_x^i(\sigma_z^{i+1} + \sigma_z^{i-1}) + h_7\sigma_y^{i-1}\sigma_x^i\sigma_y^{i+1} + \dots \end{aligned} \tag{5.59}$$

Dots correspond to higher-order contributions from the further non-local terms that go into any quasi-local Hamiltonian. The first three terms are modified from the original Hamiltonian, while the new term $\sigma_z\sigma_z$ appears as a density-density interaction, with a strength $h_4 \sim J\lambda^2/h^2$ for $h \gg J, \lambda$. The first four terms are block-diagonal in the sectors with fixed number of Jordan-Wigner fermions. The further terms break the block structure and are suppressed with increasing size of the variational ansatz.

The last step is to compute the low-energy matrix elements. For the particular values chosen, the ground state is a polarized product state $|\downarrow\downarrow \dots \downarrow\downarrow\rangle$ and the one- and two-particle subspaces have the same span as the one- and two-spin-flipped sectors. Therefore the matrix elements of $\tilde{H}$ are particularly easy to compute. Remarkably, for $h = 3$ the one- and two-particle states are not the lowest-energy states due to the hopping bandwidth, as some three-particle states

have lower energies. This observation means that the projected manifold does not describe all low-energy states of H. Nonetheless, this projection contains the most relevant states with the largest contributions to the correlation functions, and therefore the method still works very well. The importance of few-particle states is also generally observed in truncated spectrum approaches (see below).

The effective Hamiltonian $\tilde{H}_{\text{eff}}$ can be represented in matrix form in the eigenbasis of H_0 as

$$\begin{bmatrix} \langle\emptyset_0|\tilde{H}|\emptyset_0\rangle & \langle\emptyset_0|\gamma_k\tilde{H}|\emptyset_0\rangle & \langle\emptyset_0|\gamma_k\gamma'_k\tilde{H}|\emptyset_0\rangle \\ \dots & \langle\emptyset_0|\gamma_k\tilde{H}\gamma^\dagger_{k'}|\emptyset_0\rangle & \langle\emptyset_0|\gamma_k\gamma_{k'}\tilde{H}\gamma^\dagger_{k''}|\emptyset_0\rangle \\ \dots & \dots & \langle\emptyset_0|\gamma_k\gamma_{k'}\tilde{H}\gamma^\dagger_{k''}\gamma^\dagger_{k'''}|\emptyset_0\rangle \end{bmatrix}.$$

We emphasize that these matrix elements are computed with respect to the unperturbed Hamiltonian's eigenstates, whose analytic properties are known. In principle, computing the overlaps may require a systematic decomposition of $\tilde{H}$ into products of fermionic raising and lowering operators $\tilde{H} = \sum \gamma{+}\gamma\gamma{+}\gamma\gamma\gamma{+}\dots$ and repeated application of Wick's theorem; in this example it was avoided by direct computation in the total $Z \in \{-N, -N+1, -N+2\}$ subspace. The effectiveness of the rotation is shown in Fig. 5·6, where the block-diagonal structure can be clearly observed.

It might be tempting to decompose these matrix elements as "fixed-particle-number" states; however this may only work for low-energy states well separated in energy. At larger energies and at any finite density this particle picture breaks down and states exhibit the chaotic behaviors associated with the Eigenstate Thermalization Hypothesis (Rigol et al., 2008; D'Alessio et al., 2016) (also Appendix A.1).

Instead, this rotation-and-truncation procedure should be seen as a low-energy/low-

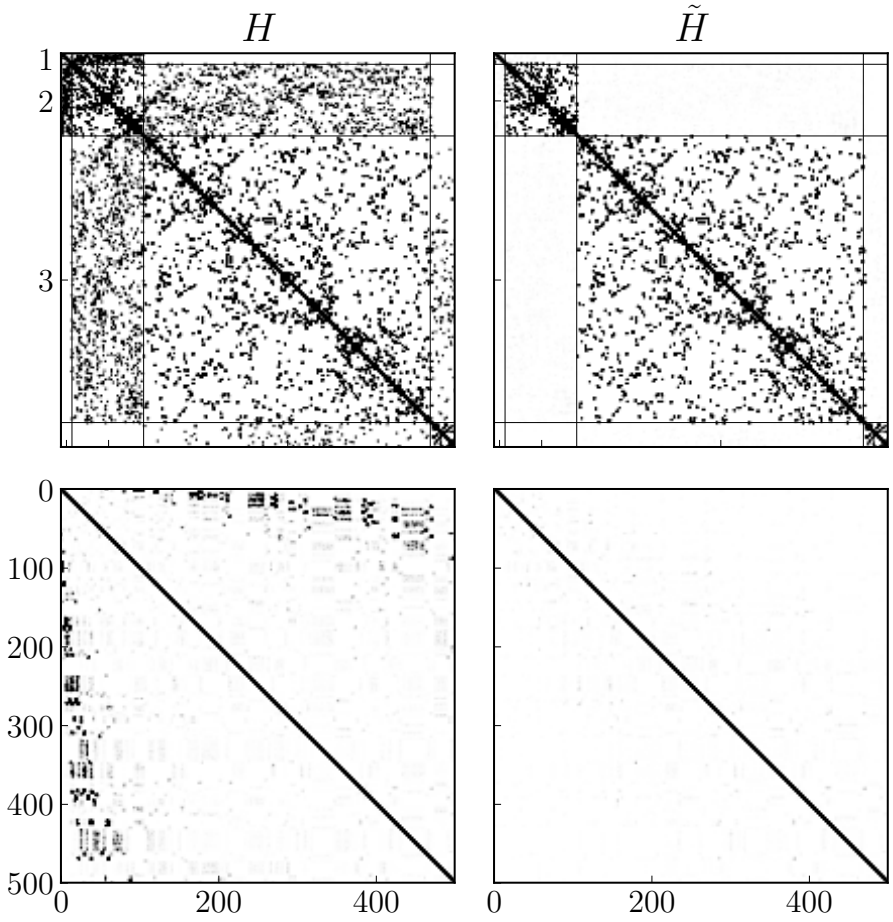

Figure 5·6: Illustration of the matrix structure of 14-site original and rotated XY Hamiltonian. This is shown in both the eigenbasis of $\sum_i \sigma_z^i$ (top) and the eigenbasis of H_0 (bottom).

density field theory limit of a quantum chaotic model, where integrable states transform into other integrable states. The rotation U can be seen as a dressing of low-energy particle excitations, which include the non-perturbative integrability-breaking effects. For low energies and large gaps, the particle nature of excitations persists, simply from scattering phase-space considerations: a single particle cannot decay into two due to mass differences.

Results for this model are shown in Figs. 5·7 and 5·8. The first of these figures shows the comparison between the approximate and exact results for a small system of 16 sites. For computing the exact results the full 2^{16} Hilbert space was used, as there are no simultaneous symmetries of the Hamiltonian and wave function. However, the wave function is still close to the ground state and the largest overlap was with low-energy eigenstates, as can be seen in the right figure. The rotated, projected version has 137 states corresponding to zero, one, or two spins flipped (see also Fig. 5·6). Note again that these 137 states represent the most relevant states, which do not necessarily correspond to the lowest energy states.

It may come as a surprise how close to the exact result this method is. There is no small parameter in the Hamiltonian, and there are no clearly defined energy spacings. However, one can see even a single-site ansatz can do quite well. Suppose a SW generator with $\theta = \tan^{-1}(\lambda/h)$

$$A = \theta \sum_i \sigma_y^i. \tag{5.60}$$

The rotated Hamiltonian can be calculated exactly, as the generator is explicitly local, and is

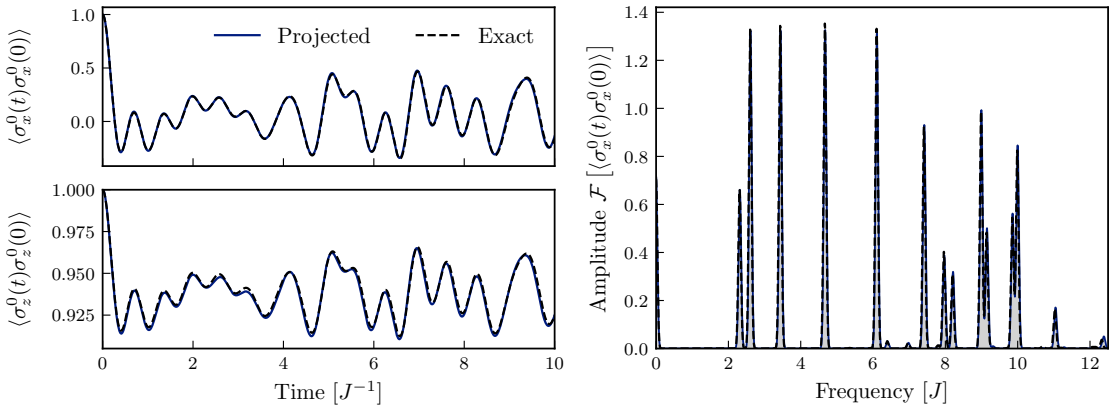

Figure 5·7: Approximate and exact response functions for the $U(1)$-broken XY model for a system of 16 sites. Left figures present time-dependent expectation values for $\langle \sigma_\alpha^0(t)\sigma_\alpha^0(0)\rangle$ with $\alpha = x, z$, both for the exact (2^{16} degrees of freedom) and the projected (137 degrees of freedom) system. Observe that exact and projected results are almost indistinguishable. Right figure presents the dynamic structure factor $S(\omega)$ as Fourier transform of $\langle \sigma_x^0(t)\sigma_x^0(0)\rangle$. The rotated Hamiltonian gets both the correct energy eigenvalues and wave function overlaps. A decoherence width of $0.05J$ has been applied to smoothen the spectrum.

$$\tilde{H} = \sum_i \cos^2(\theta)\sigma_x^i\sigma_x^{i+1} + \sin^2(\theta)\sigma_z^i\sigma_z^{i+1} + \sin(\theta)\cos(\theta)\left(\sigma_x^i\sigma_z^{i+1} + \sigma_z^i\sigma_x^{i+1}\right) + \sigma_y^i\sigma_y^{i+1} + \sqrt{h^2+\lambda^2}\sigma_z^i. \tag{5.61}$$

This rotated Hamiltonian still has matrix elements between particle sectors. In particular it contains an anisotropy of $(1 - \cos^2\theta)$ corresponding to the difference between the XX and YY interactions, which adds/removes two particles. In addition, the new XZ interactions proportional to $\sin\theta\cos\theta$ allow for the creation of single-particle excitations. However, for $J \ll \lambda, h$ these terms are suppressed by powers of J/h and J/λ, so the Hamiltonian is still effectively free with a renormalized mass. Higher orders of the gauge potential conspire to make these particle-nonconserving terms smaller, at the expense of adding longer range particle-conserving interactions.

This non-perturbative performance may also be a consequence of the choice of subspace. While the model is quantum chaotic and obeys the Eigenstate Thermalization Hypothesis (see Appendix A.1), low energy states don't necessarily need to be chaotic, and may deform nicely under local transformations, which is well-captured by these local generators.

To emphasize applicability of the method to large systems Fig. 5·8 presents the response functions for 144 sites, leading to 10441 states in the restricted Hilbert space. At low energies the excitations resemble those of free particles, while at energies greater than $\sim 6J$, the spectrum broadens as two-particle effects become relevant, indicative of a finite particle lifetime.

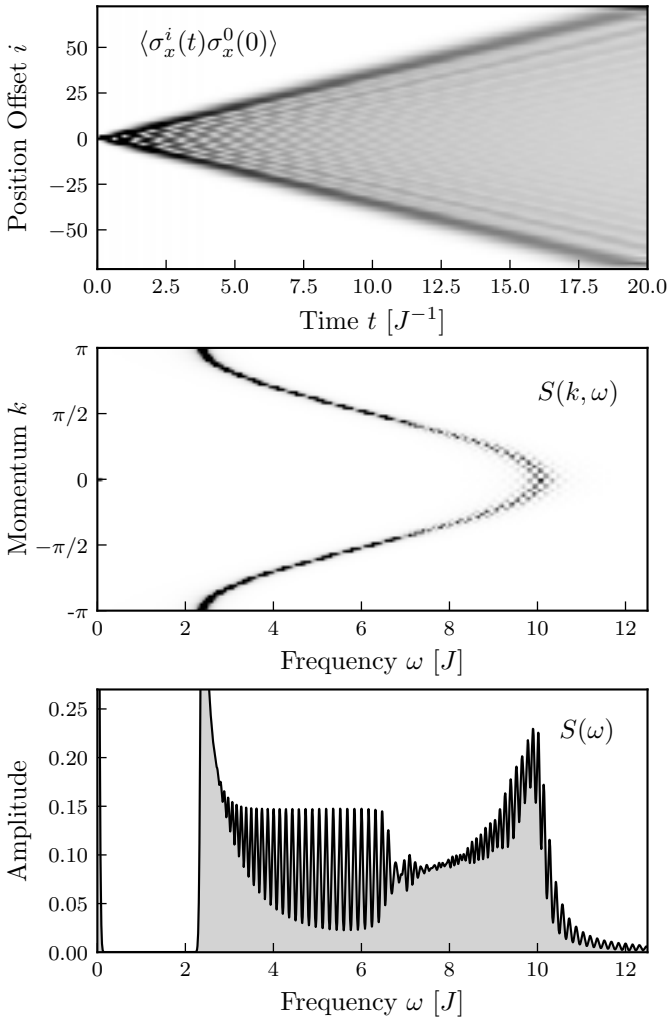

Figure 5·8: Offset time correlation function $\langle\sigma_x^i(t)\sigma_x^0(0)\rangle$ for a system of 144 spin sites and 10441 reduced degrees of freedom. The panels from top to bottom represent (i) the correlation function $\langle\sigma_x^i(t)\sigma_x^0(0)\rangle$, (ii) its spatial- and time-Fourier transform returning the dynamic structure factor $S(k,\omega)$, and (iii) the integrated frequency response $S(\omega)$. Quasi-particle excitations can be clearly observed in all the figures. At low energies, the response is that of a free particle; at larger energies the response widens, signaling finite particle lifetime. In the bottom panel a decoherence factor with width of $0.05J$ has again been applied to smoothen the function.

5.5 The mixed-field Ising model

As another example, suppose the following system, the mixed field Ising model

$$H = \sum_i^N J\sigma_z^i\sigma_z^{i+1} + h_x\sigma_x^i + h_z\sigma_z^i. \tag{5.62}$$

For $h_z = 0$ the model is integrable via a Jordan-Wigner transformation to free fermions (Sachdev, 2011; Calabrese et al., 2012a; Calabrese et al., 2012b) with a critical point at $h_x = 1$ and small h_z being an integrable E(8) field theory (Zamolodchikov, 1989). For $h_x = 0$ the model is a purely classical Ising model. For $h_x^2 + h_z^2 \to \infty$ the model is an exactly solvable collection of single spins with an onsite field. At $h_z = 2, h_x = 0$ there is a first-order multicritical point (Simon et al., 2011) and for small h_x, the low energy effective Hamiltonian is the PXP model (Bernien et al., 2017; Turner et al., 2018a). Elsewhere, the model has no apparent conservation laws or symmetries beyond geometric ones and is generally quantum chaotic (Kim et al., 2014; D'Alessio et al., 2016). However, this does not prevent approximate conservation laws or nonthermal states, as will indeed be seen.

The variational ansatz is chosen to be that of Jordan-Wigner strings, i.e. strings of Pauli operators which map to fermion bilinear operators, plus all operators local within a span of n sites

$$\begin{aligned}\{B\} = \{&\sigma_y^0, \quad \sigma_x^0\sigma_y^1, \ldots, \sigma_x^0\sigma_y^n, \ldots, \sigma_y^0\sigma_z^1\sigma_x^2, \ldots, \\ &\sigma_z^0\sigma_y^1, \quad \sigma_z^0\sigma_x^1\sigma_y^2, \quad \sigma_z^0\sigma_x^1\sigma_x^2\sigma_y^3, \quad \sigma_z^0\sigma_x^1\sigma_x^2\sigma_x^3\sigma_y^4\ldots\}.\end{aligned} \tag{5.63}$$

Additional symmetries and properties reduce the size of the ansatz: the AGP

has all of the symmetries of the full Hamiltonian[3]. By gauge choice the AGP can be completely imaginary for real Hamiltonians (Kolodrubetz et al., 2017b), constraining $\{B\}$ to only include terms with an odd number of σ_y. Because the Hamiltonian is translation and reflection invariant, the ansatz can be chosen to be as well. The inclusion of Jordan-Wigner strings is motivated by this ansatz being exact for the transverse Ising model (Kolodrubetz et al., 2017b), due to its extra symmetries and mapping to free fermions.

While a Hamiltonian of interest is given by particular choice of parameters h_x, h_z, there is relative freedom for choice of the path $h_x(\mu)$, $h_z(\mu)$ in the 2d parameter space $H(\mu)$, and especially choice of simple Hamiltonian $H(0)$. This is because there are many "simple" points in the (h_x, h_z) parameter space which might be considered "close" to the Hamiltonian of interest. The $(h_x, 0)$ line is the transverse Ising model; the $(0, h_z)$ line is the classical Ising model; and the $(h_x, h_z) \to \infty$ line are independent spins with onsite fields.

What starting points, and which path in parameter space, is optimal for computing approximate eigenstates, given ansatz $\{B\}$, Hamiltonian $H(1)$, and subspace P? This is a question of a *path-dependent Schrieffer Wolff transformation*, as the performance of computing approximate eigenstates, or equivalently block diagonalization, may depend on these choices. This work chooses from a limited set of parameterized Hamiltonians with particular starting and ending points.

[3]This can be seen by the definition of the regularized AGP in Eq. (5.19)

$$H_1(\mu) = \sum_i^N \sigma_z^i \sigma_z^{i+1} + \mu\big(h_x\sigma_x^i + h_z\sigma_z^i\big), \tag{5.64}$$

$$H_2(\mu) = \sum_i^N -\sigma_z^i \sigma_z^{i+1} + \mu\big(h_x\sigma_x^i + h_z\sigma_z^i\big), \tag{5.65}$$

$$H_3(\mu) = \begin{cases} \sum_i^N 2\mu h_x\sigma_x^i + h_z\sigma_z^i, & \mu \in [0, 0.5) \\ \sum_i^N (2\mu-1)\sigma_z^i\sigma_z^{i+1} + \big(h_x\sigma_x^i + h_z\sigma_z^i\big) & \mu \in [0.5, 1] \end{cases}. \tag{5.66}$$

The first and second parameterizations start from the $\sigma_z\sigma_z$ point, whose eigenstates are Z polarized spins. Depending on the sign, the ground state could be an antiferromagnetic (AFM) Neél (5.64) or a polarized ferromagnetic (FM) state (5.65). Low energy particle excitations are boundary walls of spin flips (see Fig. 5·9)[4].

The third parameterization (5.66) is split into two parts. The first leg is simply rotating the on-site field and thus the AGP is exact $A(\mu) \sim \sum_i \sigma_y$, and is an example of the Landau-Zener problem, rotating the spin in the XZ plane. The second leg has no such local exact representation. The ground state is a product state of spins pointing in Z. Low energy particle excitations are spin flips (see Fig. 5·9) to the opposite direction.

In all cases, $H_*(0)$ is degenerate, with a natural choice of projective subspace being fixed particle number on top of the ground state. Thus, P_1 is 0 and 2 boundary walls on top of an AFM ground state; P_2 is 0 and 2 boundary walls on top of a FM state; and P_3 is the 0, 1 and 2 particle spin flips on top of a polarized state.

[4]This work exclusively uses an even number of sites and periodic boundary conditions to avoid any AFM ground state degeneracy; particles always come in pairs.

$$P_1 = \left\{ |\uparrow\downarrow \ldots \uparrow\downarrow\rangle \quad , \quad \left(\sigma_x^i \sigma_x^{i+1} \ldots \sigma_x^{i+n}\right) |\uparrow\downarrow \ldots \uparrow\downarrow\rangle \right\},$$
$$P_2 = \left\{ |\uparrow\uparrow \ldots \uparrow\uparrow\rangle \quad , \quad \left(\sigma_x^i \sigma_x^{i+1} \ldots \sigma_x^{i+n}\right) |\uparrow\uparrow \ldots \uparrow\uparrow\rangle \right\},$$
$$P_3 = \left\{ |\downarrow\downarrow \ldots \downarrow\downarrow\rangle \quad , \quad \left(\sigma_x^i\right) |\downarrow\downarrow \ldots \downarrow\downarrow\rangle \quad , \quad \left(\sigma_x^i \sigma_x^j\right) |\downarrow\downarrow \ldots \downarrow\downarrow\rangle \right\}. \tag{5.67}$$

Because the system is translation invariant, the zero-momentum sector is chosen as a numerical simplification. Under these constraints, each subspace P has $N+1$ states each out of total Hilbert space dimension $\approx 2^N/N$.

These basis states are each dressed by the variational AGP to create dressed boundary wall states: the hard boundary is softened by the dressing procedure to better describe the interacting quasiparticle excitations.

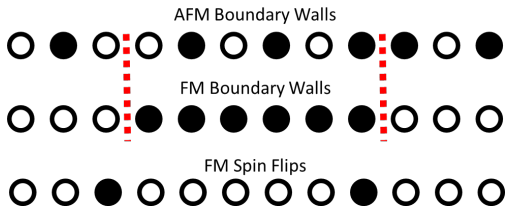

Figure 5·9: Example basis states of two particles separated by 6 sites. Top and middle are states with two boundary walls (red dashes), which are low energy eigenstates of $H_1(0)$ and $H_2(0)$, with excitation energy $4J$. Bottom is a state with two spin flip particles, which is a low-energy state of $H_3(0)$ with excitation energy $4h_z$.

Approximate eigenstates and spectrum

As an explicit example, let us choose the parameters $h_x = 0.4 = h_z$, and coupling $J = \pm 1$. These parameters are non-perturbative, in the sense 0.4 is $\mathcal{O}(1)$ away from any simple point. For $J = -1$, the ground state is ferromagnetic, and the h_z term acts as a constant attractive force between two boundary wall particles. This leads to "meson" bound states of the two boundary walls (Kormos et al., 2017). For $J = +1$, the h_z term does not change the AFM ground state energy

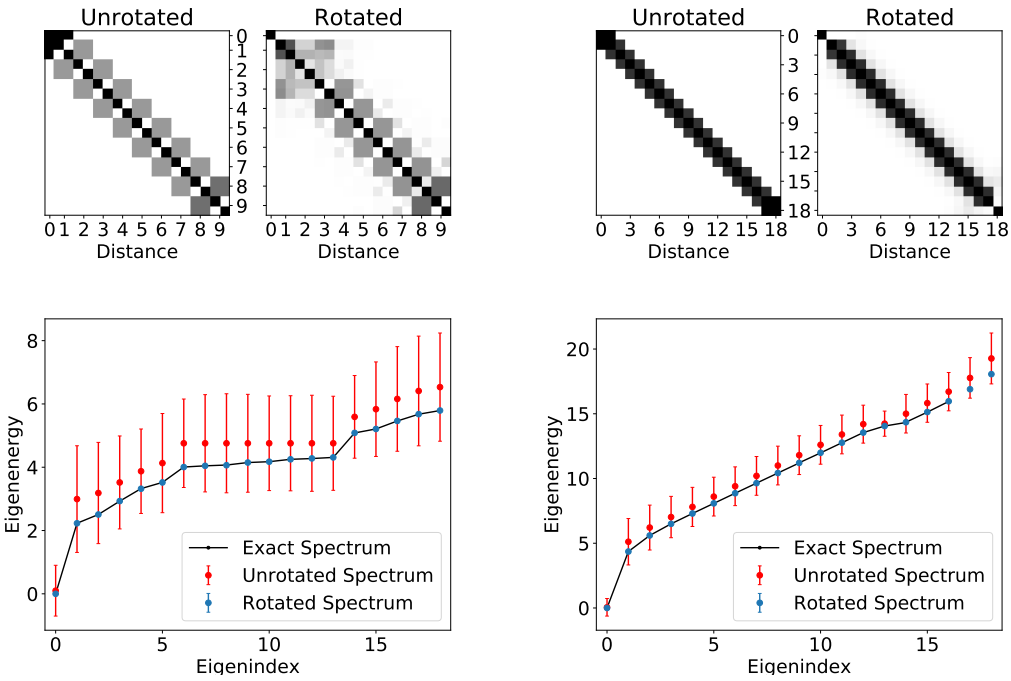

Figure 5·10: Eigenspectrum of the zero momentum mixed-field Ising model of Eq. (5.62)**.** Left is for 18-site AFM states ($J = +1$) while right is for 18-site FM states ($J = -1$). Top are matrix elements of the rotated and unrotated effective Hamiltonian indexed by boundary wall distance. Bottom is a comparison between the exact spectrum (computed numerically), the unrotated TSA spectrum (red), and the rotated spectrum (blue). Error bars are the energy variance of the approximate eigenstates.

(Ovchinnikov et al., 2003; Bonfim et al., 2019); however it will affect energies of spin flips on up/down Neél sublattices, which, from a band theory context, leads to two free particle species.

One can then go through the process of computing approximate eigenstates for these particular choices of subspaces. Here, Hamiltonians (5.64), (5.65) are chosen starting from the FM and AFM subspaces, with an ansatz of all operators local to 3 sites plus Jordan Wigner strings, with 18 total sites in the 0 momentum sector.

Results for these parameters are shown in Fig. 5·10. Top plots the effective unrotated and rotated Hamiltonian, or equivalently the Hamiltonian in the projective and rotated projective subspaces, for AFM (left) and FM (right) excitations. It can be clearly seen that the rotated effective Hamiltonian becomes slightly more nonlocal: a dressed boundary wall of width 3 may hop to become width 5, for example. These effects are especially pronounced when the two boundary walls are close together, which is an indicator of a 2-particle interaction. When the two particles are far apart the Hamiltonian becomes independent of distance.

The spectrum is shown on the bottom plots of Fig. 5·10. Clearly, there is remarkable improvement over naïve TSA (red) with the unrotated basis, and the rotated version (blue) is almost identical to the exactly computed eigenspectrum (black). The error bars are the energy variance of the approximate eigenstates, as computed from Eq. (5.29). Note that the exact eigenvectors are matched with approximate ones by choosing those which have maximum fidelity $|\langle E_n|E_m^{\text{exact}}\rangle|^2$; normally this value is > 0.9.

Importantly, the eigenstates are not necessarily all the lowest energy states. For example, two of the lowest-energy FM boundary walls (each with excitation

energy $4.4J$) has a higher energy then a single FM boundary wall of width 6 (with excitation energy $8.7J$). This means it is energetically possible for the width-6 boundary wall to decay into two width-1 boundary walls, for example. However, the small energy variance of these dressed states indicates that such a process is almost completely suppressed.

Because the dressing is local, it is possible to take a continuum or large system size limit. Numerically, this is done by duplicating the dressed Hamiltonians of Fig. 5·10 over thousands of sites: The 19×19 matrix is extended to a $N \times N$ matrix, where the middle elements are the duplicated middle elements of the smaller matrix. Then, the eigensystem of that Hamiltonian is computed. Results for the continuum dispersion relation of excitations on top of the AFM ground state are shown in Fig. 5·11. There are two particle species which have mass 1.11 and 2.56. Like the meson case, the states are not necessarily the lowest-energy states: for example, 2 heavy particles can have equal energy to 4 light particles, and may potentially decay as such. Note that two light particles could not decay into 1 heavy particle, as that is disallowed by the particles being domain walls.

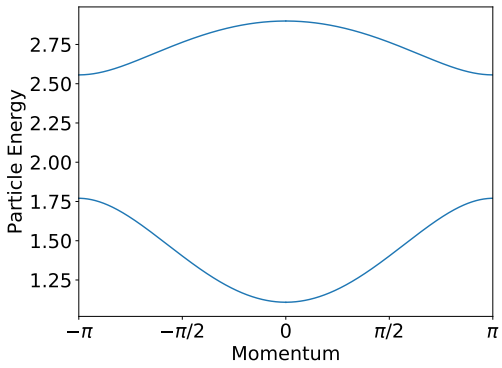

Figure 5·11: Dispersion relation of the two particle species on top of an AFM ground state. The 2-heavy particle energy lies above the 4-light particle continuum.

These approximate eigenstates can be compared with the general bulk eigenstates, as is shown in Fig. 5·12 Top. Here, all eigenstates in the 18-site FM model,

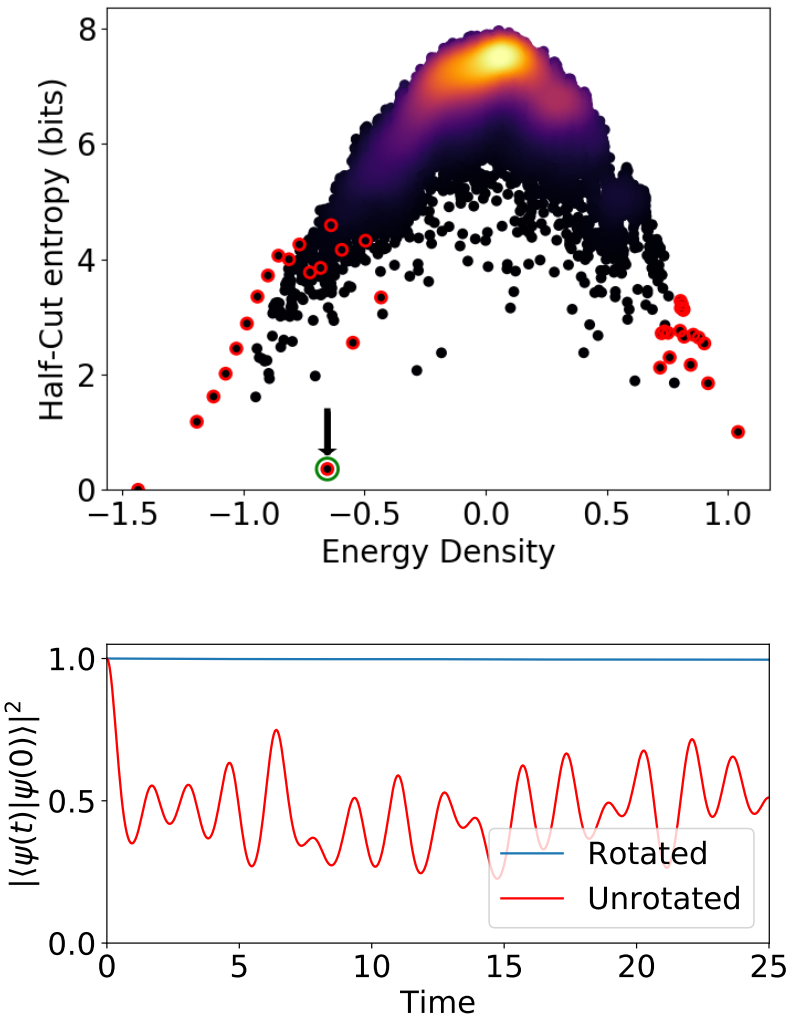

Figure 5·12: Top: Comparison of half-cut eigenstate entanglement entropy for the 18-site FM chain and 0 momentum. Red circles are the states with maximum overlap with the approximate eigenstates; left are dressed ferromagnetic states while right are dressed anti-ferromagnetic states. Note that high-energy states of the FM model are not the same as the low-energy states of the AFM model. Green circle and arrow indicates the dressed all-up state, which is a nonthermal state. **Bottom:** Fidelity of the dressed-all-up state with the initial state $|\langle E(t)|E(0)\rangle|^2$ which indicates the rotated all-up state is very close to an eigenstate, while the unrotated version is not, and is well preserved in time.

0-momentum sector (14,602 total) are computed exactly, and their half-cut entanglement entropy is found. Thermal states are extensively entangled states at finite energy density, while nonthermal states are weakly entangled and generally have zero or low energy density (Turner et al., 2018a). Red circles are the states which have maximal overlap with the approximate eigenstates: low energies are FM states while high energies are AFM states.

One particular approximate eigenstate merits more study: the dressed all-up eigenstate, indicated by the green circle and arrow in Fig. 5·12 Top. This is a ground state of $\sigma_z\sigma_z$, but the most excited state of σ_z; it has finite energy density given roughly by $2h_z$. But, in particular, it is an explicit example of a highly non-thermal state far from the edges of the spectrum (Abanin et al., 2019; Turner et al., 2018a; Lin and Motrunich, 2019; Choi et al., 2019). It is locally entangled with a half-chain entanglement entropy of ≈ 0.25 bits. It has very high fidelity of 0.995 with an exact eigenstate. Note that in the thermodynamic limit the dressed-all-up state is exponentially orthogonal to the original all-up state due to the finite local rotation.

Quasiparticle Lifetimes

The energy variance of these approximate eigenstates takes special meaning when they can be interpreted as dressed particles. In this case, the energy variance gives a lower bound on the quasiparticle lifetime. For an approximate particle eigenstate $|E_n\rangle$, the time-dependent state overlap under second order perturbation theory is

$$\left|\langle E_n|E_n(t)\rangle\right|^2 \approx 1 - \frac{t^2}{\tau^2} + \mathcal{O}(t^4), \tag{5.68}$$

where $\tau^{-2} = \Delta^2 = \langle H^2 \rangle - \langle H \rangle^2$ is the energy variance of the state. In other words, the characteristic time for an (eigen)state of some particles to decay into some other particle state is given by the energy variance. This timescale is very crude as it assumes all other states have the same energy: a more refined timescale can be computed using the Fermi golden rule (Sachdev, 2011) for the dressed states, but is not generally possible without a priori knowledge of the energy of the other states. As such, the energy variance serves as a lowest bound on (inverse) quasiparticle lifetime.

As an explicit example of these timescales, a dressed single flipped down spin on a FM ground state, which corresponds to the lowest energy meson excitation, has a characteristic lifetime of $\tau = 110$, far longer than any local timescale. Excitations on top of an AFM ground state have lifetimes in excess of $\tau > 60$. The dressed all-up state has a lifetime of $\tau = 53$. These lifetimes are longer when adding more parameters to the variational AGP. Explicit time dynamics of Eq. (5.68) for this dressed all-up state is shown in Fig. 5·12 Bottom. Clearly, it is much closer to an eigenstate than expected, as it is close to 1 at all times. This further indicates the genuineness of this nonthermal eigenstate, especially when compared to the undressed version of the same. Note that the undressed up state is exponentially orthogonal in system size from the dressed up state, due to the finite rotation.

One application of such a dressed all-up state is for information protection in quantum systems. For a classical Hamiltonian, the all-down [ground] state may be labeled as a logical 0, while the all-up state is labeled as a logical 1. An X-field will generally change these two states, destroying the encoded bit. If this bit is instead encoded in the dressed nonthermal states (the all down ground state, and the all up nonthermal state), they are much more stable, encoding the information for a much longer time by suppressing transitions.

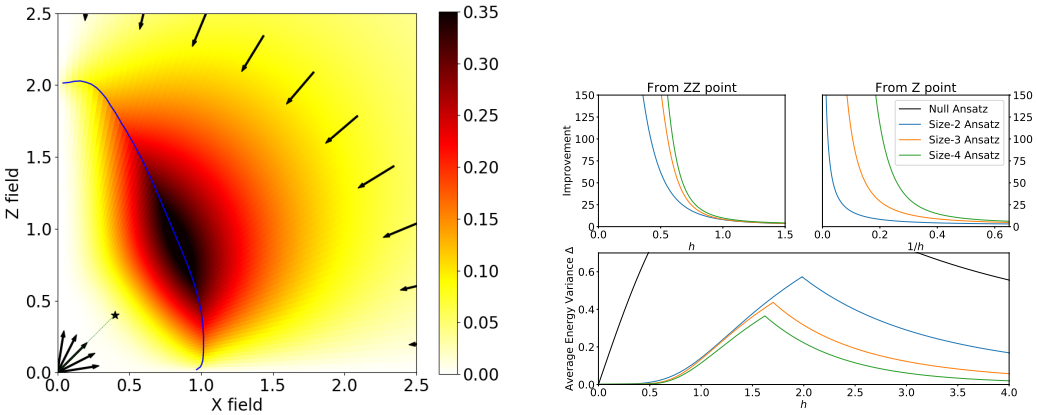

Figure 5·13: Results for a 3-site VGP ansatz for the 14-site mixed-field Ising model. Left: Average inverse 2-particle lifetime Γ or equivalently average energy variance. Blue line indicates transition between different directions. Star is the $(0.4, 0.4)$ point studied more in-depth. Arrows indicate direction of dressing. White and yellow indicate areas with a good quasiparticle description. **Right Bottom:** Average energy variance in the direction $\pi/4$ from vertical. Middle is improvement from the undressed subspace. Below $h \approx 0.6$, the error is vanishingly small. **Right Top:** Energy variance improvement compared to the Null ansatz Γ/Γ_0 along the $h_x = h_z$ line. As the ansatz size increases, so too does the improvement, as expected.

Quasiparticle parameter dependence

A general measure of the quasiparticle lifetime within a particular subspace is given by their normalized average inverse lifetime, or equivalently average energy variance or the block-off-diagonal weight of the rotated subspace $\tilde{P}$

$$\Gamma = \frac{1}{\sqrt{\mathcal{D}_p}\sqrt{1+h_x^2+h_z^2}}\sqrt{\sum_n \Delta_n^2}. \tag{5.69}$$

A small value indicates a good block-diagonalization procedure with well-

defined quasiparticles within the subspace. A large value indicates a failure to block diagonalize the Hamiltonian.

This error can be computed for various values of h_x and h_z by evolving with parameterized Hamiltonians (5.64) and (5.66), computing approximate eigenvalues, then computing their normalized average energy variance $\Gamma(h_x, h_z)$. Results are shown in Fig. 5·13, for a 3-site ansatz and 14 sites. States are dressed from one of two directions. One is $H_1(\mu)$, dressing 2-particle AFM boundary wall states out from the $\sigma_z\sigma_z$ only point, indicated by the radial arrows in the bottom left. The other is $H_3(\mu)$, dressing 1 and 2-particle spin-flip states from the $h_x\sigma_x + h_z\sigma_z$ only point(s), indicated by the arrows pointing radially inwards.

In the region where h_x, h_z is small, the error from dressing boundary walls is enormously low. With no dressing, the error grows linearly in $|h|$, while with dressing, the error grows sub-linearly, which indicates that the dressing is exact asymptotically. In fact, this dressing accumulates very small errors even for non-perturbative values of $|h|$, as shown in Fig. 5·13 Bottom, which is dressing along the $h_x = h_z$ line. This indicates that in the white areas, there is a good effective quasiparticle description of the low energies of this otherwise quantum chaotic model, described by dressed boundary wall particles.

Although it is not generally so, the error accumulates monotonically with increasing $|h|$. This means that at some critical value, the dressing going *outwards* from the $\sigma_z\sigma_z$ point will have a larger error then the dressing going *inwards* from the $(h_x, h_z) \to \infty$ point. At this boundary, the best description of quasiparticles changes from dressed pairs of *boundary walls*, to dressed *spin flips*. This does not mean that there is no effective description of certain states in terms of quasiparticles: there could be some other subspace (say, of doubly-flipped spins) and other path through parameter space which gives a better quasiparticle picture in that

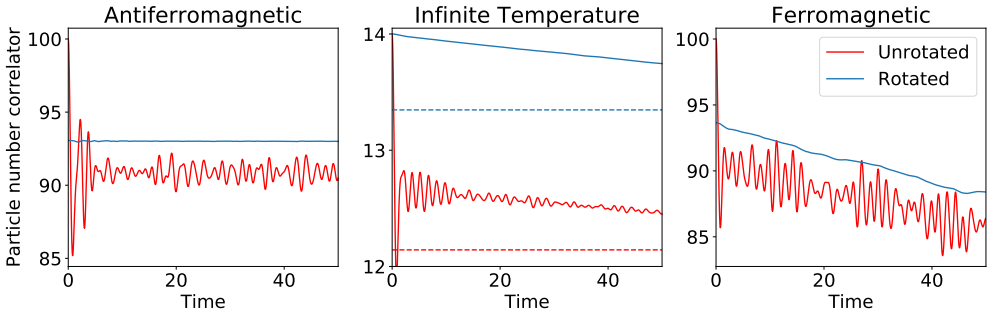

Figure 5·14: Symmetric time correlation function of dressed (blue) and undressed (red) particle number. This plots Eq. (5.82) and Eq. (5.81) for a 2 particle AFM subspace (left), 2 particle FM subspace (right) and all states (middle), and 14 sites. Dashed are the infinite temperature long-time values.

the energy variance is smaller.

This cross-over point may be an indicator of an interacting phase transition. Around $h_z = 0, h_x = 1$, which is the transverse Ising phase transition, it has been found that local variational adiabatic dressing begins to fail (Kolodrubetz et al., 2017b). This finding is now extended to the interacting case: the cross-over gives a rough region where the interacting critical point may occur, as a local AGP fails to reproduce the long-range entanglement of a critical ground state (Hastings, 2007). With increasing ansatz size, this point decreases in total error, and shifts in critical parameter (see Fig. 5·13 Bottom) which may eventually converge to some particular value, indicating the interacting critical point. This idea is backed up by the convergence in the non-interacting limit: For h_z small, the crossover is around the $h_x \approx 1$ transverse Ising critical point. Similarly, for h_x small, the crossover is around $h_z \approx 2$, which is the first-order phase transition in h_z to change the ground state from AFM to polarized (Simon et al., 2011).

Local almost-conserved operators

Given some set of approximate local eigenvectors $\{|E_n\rangle\}$ generated by this adiabatic dressing scheme, it is a relatively simple procedure to construct approximately conserved local operators. An operator is conserved if it commutes with the Hamiltonian, or equivalently if it is constructed from eigenstates of the Hamiltonian. Given approximate eigenstates, one should then be able to compute approximately conserved quantities. Conserved operators are defined as

$$\mathcal{O} = \sum_n O_n |E_n\rangle\langle E_n| \tag{5.70}$$

where O_n are the eigenstates of the operator, and$\{|E_n\rangle\}$ are exact eigenstates. An operator of this form has the property that the symmetric time correlation function is conserved (for all initial states)

$$\frac{\langle\{\mathcal{O}(t), \mathcal{O}(0)\}\rangle}{2} = \text{Constant}. \tag{5.71}$$

There are two ways to construct approximate versions of these operators. The first way is to explicitly use Eq. (5.70) using only the subspace of dressed eigenstates which were directly computed. In this case, the sum is of size $\mathcal{D}_P$, the subspace size, as opposed to $\mathcal{D}$, the total Hilbert space size. Due to the global projective structure of particle excitations on top of a ground state, the resulting operator is not necessary local. However, this may be implemented with some local operator plus post-selection of states.

In the case of such an operator directly constructed from approximate eigenstates, the symmetric correlation function is not conserved in time. Under perturbation theory, the characteristic timescale is given by a weighted-average energy variance. Suppose some set of $\mathcal{D}_P$ approximate eigenstates $|E_n\rangle$ diagonal-

ized within some subspace P, and operator $\mathcal{O} = \sum_n O_n |E_n\rangle\langle E_n|$ for Hamiltonian H. For simplicity, let us choose a subspace $[\rho, O] = 0$ or equivalently $\rho = \sum_n \rho_n |E_n\rangle\langle E_n|$. In this case, the symmetric correlation function may be equivalently written as

$$\frac{\mathrm{Tr}\big[\rho\{\mathcal{O}(t), \mathcal{O}(0)\}\big]}{2} = \mathrm{Tr}\big[\rho\mathcal{O}(t)\mathcal{O}\big]. \tag{5.72}$$

Next, expand the operator to second order in a BCH series

$$\mathcal{O}(t) \approx \mathcal{O} + it[H, \mathcal{O}] - \frac{t^2}{2}\big[H, [H, \mathcal{O}]\big] + \dots \tag{5.73}$$

and substitute back in. The first order term is zero via trace identities. What remains is

$$\frac{\mathrm{Tr}\big[\rho\{\mathcal{O}(t), \mathcal{O}(0)\}\big]}{2} \approx \langle \mathcal{O}^2 \rangle - \frac{t^2}{2}\mathrm{Tr}\big[\rho\big[H, [H, \mathcal{O}]\big]\mathcal{O}\big] + \dots . \tag{5.74}$$

Next, inspecting the second term and using the cyclicity of the trace and definition of $\mathcal{O}$, find

$$\mathrm{Tr}\big[\rho\big[H, [H, \mathcal{O}]\big]\mathcal{O}\big] \tag{5.75}$$

$$= \mathrm{Tr}\big[H^2\mathcal{O}^2\rho + H^2\mathcal{O}\rho\mathcal{O} - 2H\mathcal{O}H\mathcal{O}\rho\big]$$

$$= 2\rho_n O_n \Big(O_n \langle E_n|H^2|E_n\rangle - \langle E_n|H|E_m\rangle O_m \langle E_m|H|E_n\rangle \Big). \tag{5.76}$$

The $\mathcal{D}_P$ states $|E_m\rangle$ are constructed such that they are diagonal in H within rotated subspace P, by the TSA procedure. This means that that $\langle E_m|H|E_n\rangle = E_n\delta_{mn}$. However, the operator H^2 will generally be different, as it will include states outside of the subspace. Generally, H^2 may be computed efficiently ana-

lytically without needing to use a full Hilbert space. Thus this simplifies to

$$\mathrm{Tr}\big[\rho\big[H,[H,\mathcal{O}]\big]\mathcal{O}\big] = 2\rho_n O_n^2\bigg(\langle E_n|H^2|E_n\rangle - \big(\langle E_n|H|E_n\rangle\big)^2\bigg). \tag{5.77}$$

The term in parenthesis is the energy variance of eigenstate $|E_n\rangle$ as defined in Eq. (5.29), and so the decay timescale is related to the energy variance as

$$\frac{1}{\tau^2} \equiv \frac{\sum_n \rho_n O_n^2 \Delta_n^2}{\sum_n \rho_n O_n^2}. \tag{5.78}$$

For good eigenstates with low energy variance, the decay timescale can be very long.

The second way to construct approximately conserved operators is to dress conservation laws of the simple system $H(0)$ with the unitary. Conservation laws, such as particle number and particle current, are constructed from simple eigenstates in the form of Eq. (5.70), with particular choice of O_n, and are generally local (Calabrese et al., 2012a; Karbach and Muller, 1998). Then, the dressed operator is constructed from states better resembling eigenstates

$$\mathcal{O} = U\bigg(\sum_n O_n\big|E_n(0)\big\rangle\big\langle E_n(0)\big|\bigg)U^\dagger \tag{5.79}$$

$$\Updownarrow$$

$$\mathcal{O} = U\mathcal{O}_0U^\dagger. \tag{5.80}$$

Importantly, the eigenstates of operator $\mathcal{O}$ are not necessarily the same as the constructed approximate eigenstates, as it is missing the re-diagonalization step of Eq. (5.28). The resulting operator is quasi-local, and approximately conserved

(Serbyn et al., 2013; Serbyn et al., 2014). As the ansatz span is increased, the AGP approaches the exact one, resulting in better approximate eigenstates and a better-conserved operator, at the expense of it becoming more and more nonlocal.

One such conserved operator for the mixed-field Ising model is the dressed total particle number $N = U\big(\sum_i \sigma_z^i \sigma_z^{i+1}\big)U^\dagger$ which (up to a constant) counts the number of boundary walls in the system. For H_1 and H_2, this is also the initial Hamiltonian; thus one would expect that the dressed operator should also approximate dressed versions of particle number eigenstates.

For $h_x = h_z = 0.4$ and $J = +1$, the dressed particle number operator becomes

$$N_0 = \sum_i \sigma_z^i \sigma_z^{i+1} \tag{5.81}$$

$$\Downarrow$$

$$\begin{aligned} N = \sum_i 0.9530\hat{\sigma}_z^i\hat{\sigma}_z^{i+1} + \\ 0.2135\hat{\sigma}_x^i + 0.1927\hat{\sigma}_z^i\hat{\sigma}_x^{i+1}\hat{\sigma}_z^{i+2} + \\ 0.0616\hat{\sigma}_z^i\hat{\sigma}_x^{i+1}\hat{\sigma}_x^{i+2}\hat{\sigma}_z^{i+3} + \\ -0.0398(\hat{\sigma}_z^i\hat{\sigma}_x^{i+1} + \hat{\sigma}_x^i\hat{\sigma}_z^{i+1}) + \\ -0.0243\hat{\sigma}_y^i\hat{\sigma}_y^{i+1} + \\ 0.0211\hat{\sigma}_z^i\hat{\sigma}_x^{i+1}\hat{\sigma}_x^{i+2}\hat{\sigma}_x^{i+3}\hat{\sigma}_z^{i+4} + \\ -0.0164(\hat{\sigma}_x^i\hat{\sigma}_x^{i+1}\hat{\sigma}_z^{i+2} + \hat{\sigma}_z^i\hat{\sigma}_x^{i+1}\hat{\sigma}_x^{i+2}) + \\ 0.0098\hat{\sigma}_z^i + \\ + \ldots \end{aligned} \tag{5.82}$$

where ellipsis represent the more and more nonlocal terms of the operator. As can be seen, this operator is approximately local, with dominant terms coming from

1, 2, and 3-spin terms. One can then compute the symmetric correlation function in the initial undressed subspace of two particles to see its conservation

$$\mathrm{Tr}\big[\mathcal{P}_0\{N(t), N(0)\}\big] = C(t). \tag{5.83}$$

Results are shown in Fig. 5·14 for AFM and FM states, as well as infinite temperature typical states (Goldstein et al., 2006). For comparison, the undressed operator is also shown in red. The conserved operator for AFM states is almost stationary in time, while the undressed version is not. The infinite temperature timescale can be computed analytically as

$$\frac{\mathrm{Tr}\big[\big([N, H]\big)^2\big]}{2\mathrm{Tr}\big[N^2\big]} = \tau_N^{-2} = 50.93^{-2}, \tag{5.84}$$

$$\frac{\mathrm{Tr}\big[\big([N_0, H]\big)^2\big]}{2\mathrm{Tr}\big[N_0^2\big]} = (\tau_{N_0})^{-2} = 1.25^{-2}. \tag{5.85}$$

Even for an infinite temperature state, this quasilocal dressed operator gets a factor of 40 improvement in the characteristic decay timescale. This indicates that dressed quasiparticle excitations may persist in this interacting model *even at infinite temperature*, and that this model is "closer to integrable" then one might expect.

Chapter 6

Conclusions

6.1 Summary of the thesis

This thesis is a discussion of two broad methods: introduction of new ideas in cluster phase space methods and the cTWA, and the expansion of old ideas in the form of variational Schrieffer-Wolff dressing and adiabatic dressing. Both of these methods have a similar theme: dimensional reduction to allow efficient approximate nonequilibrium dynamics of quantum systems.

The first method, the cTWA, is a phase space method mapping a quantum system to a classical phase space in order to compute nonequilbrium dynamics and response functions. Chapters 2 and 3 discussed the method itself, and some example systems to which the method was applied. It was shown that it is possible to capture both short-scale quantum behavior as well as long-scale classical behavior. This was demonstrated in the mixed-field Ising model, which rapidly thermalized, as well as various models with global conservation, which demonstrated diffusive behavior. Particularly, the cTWA was applied to analyze infinite temperature non-equal time correlation functions in a XXZ chain with first and second nearest neighbor interactions. We obtained excellent agreement between the results of exact numerical simulations and cTWA predictions for small system sizes. For larger system sizes, where exact diagonalization is not available, we found that cTWA smoothly interpolates between short time quantum correlations and long

time hydrodyanmic correlations by systematic inclusions of more degrees of freedom. We showed that both the diffusion constant D and the dynamic structure factor converge with the cluster size. Moreover as our results suggest D is strongly renormalized by quantum fluctuations and can not be accurately extracted from either traditional semiclassical approaches (due to their long time failure) or exact diagonalization (due to limited system sizes).

Similarly, it is possible to get indicators of long-time quantum behavior through systematic expansions of the degrees of freedom, as was shown for a many body localized model. In general, these ideas demonstrate that it is possible to get an effective classical limit for otherwise highly quantum systems, by massively overdoing the inclusion of many "intelligently" picked classical degrees of freedom.

The second method, adiabatic dressing and variational Schrieffer Wolff, is a potentially nonperturbative way of computing effective low-energy dynamics and properties, and is covered in chapter 5. These Schrieffer-Wolff transformations are a tool for describing effective dynamics of the relevant (for example, low-energy) degrees of freedom of interacting systems. Following a unitary transformation decoupling a low-energy subspace from the rest of the Hilbert space, an effective Hamiltonian can be obtained by projecting this transformed Hamiltonian on the selected subspace.

Using recent ideas of computing approximate adiabatic gauge potentials (AGP), one can dress a sub-basis to better approximate a particular subset of eigenstates of some interacting model. Given a particular ansatz for the AGP, this is an agnostic (intuition-independent) way of computing effective low-energy dynamics and properties of quantum systems. Particularly, it can compute low energy quasiparticle states and upper bounds on decay timescales, as well as simulate

approximate response-function dynamics above a ground state. These approximate eigenstates are not necessarily limited to low energies and can also be used to potentially find nonthermal states and quantum scars.

First, the disordered Fermi-Hubbard model was considered. The variational generator was approximated using a commutator expansion, and the subspace was that of a fixed number of singly-occupied sites. Here, it was shown that the variational approximation allows for accurate results beyond the reach of standard (perturbative) Schrieffer-Wolff methods. Second, a non-integrable XY spin chain was considered, where the variational generator was constructed out of local operators with a given spatial support. After the initial transformation, the resulting Hamiltonian can be seen as a perturbed integrable one, and the projected subspace was chosen to consist of the eigenstates of this integrable Hamiltonian with a fixed number of particles. This was then shown to be able to return accurate time response functions for system sizes beyond the reach of traditional methods. Finally, the mixed-field Ising model was considered, where approximate eigenstates were computed using the adiabatic dressing and rotated TSA approach. This also allowed a dressing of free conservation laws to approximately conserved dressed counterparts, which have much longer error decay timescales.

The existence of good approximate dressings have some curious implications. Even if a model system is not necessarily integrable or exactly solvable, that does not mean that there are no local long-lived symmetries and conservation laws. Indeed, if such a model is close by to an integrable point, a conservation law of the integrable model can be "dressed" by a unitary generated by the approximate local adiabatic gauge potential to restore the symmetry approximately in a now quasi-local operator. Approximate eigenstates may be computed in a similar manner: simple particle excitations of the integrable point can be dressed by the

approximate AGP to construct long-lived quasiparticle excitations of the interacting point. These new dressed states need not be low energy states and in fact may be used to construct finite energy density low-entanglement nonthermal states, as demonstrated in the dressed-all-up state of the mixed-field Ising model.

Similar studies have been done to compute low energy phenomenology of the Meson case, most predominantly in recent work by (James et al., 2019; Robinson et al., 2019) using a truncated spectrum approach (TSA). These numerical diagonalization procedures are functionally equivalent except that here the projective subspace is first rotated by the variational AGP, leading to a subspace closer to the exact eigenstates. While this work uses discrete lattices, generalizations to continuous theories is an interesting future direction.

The restoration of approximate symmetries and construction of quasiparticle excitations in interacting models puts a new perspective on integrability breaking. Instead of reevaluating a Hamiltonian for every new point in parameter space, one can instead compute properties and approximate symmetries based on nearby Hamiltonians with a potentially simpler structure. This "closeness" is defined in the sense of being able to compute a good approximate AGP along some path between the simple Hamiltonian and interacting one, not in the sense of perturbative parameter changes. Certain perturbations away from integrability may rapidly destroy any local conservation laws, if there exists no good local approximate AGP. Other perturbations, while still breaking integrability, may still admit quasi-local conservation laws, nonthermal states, and quasiparticles, if there does exist a good local approximate AGP.

These unitary rotations restoring approximate integrability are similar in spirit to canonical transformations in KAM theory (Brandino et al., 2015): integrability may be approximately restored for particular subsets of initial conditions

of particular integrability-broken systems via the unitary rotation (eg canonical transformation) of conserved quantities. Whether this approach to stability of quantum integrable systems can be made more concrete remains to be seen but these variational local dressings may be a step towards a general theory in that direction.

6.2 Future work

This section is directly addressed to future graduate students interested in pursuing ideas of cluster phase space or adiabatic dressing, either with Anatoli or elsewhere. There are several interesting directions to go with these two methods, which I will outline here.

General cluster phase space methods

While most of this dissertation described a cluster phase space method, the idea is more general. As discussed in chapter 4, one of the requirements on basis operators is that they form a closed group. While "all operators local to a cluster" satisfy this rule, there are many other options. For example, Jordan-wigner strings representing fermion bilinear operators form another basis of operators. Similarly, as outlined in chapter 4, operators can be dressed by some unitary rotation to potentially be a better phase space basis. While the chapter only had a quick demo with CNOT gates and a curated Hamiltonian, there is much creative choice as to what to use for the unitary or its generator. I have had some fruitful (yet incomplete) results with using the adiabatic gauge potential as the generator of this rotation, especially for many body localized systems. An eventual goal, if I had enough time, would be to try to combine adiabatic dressing methods with phase space to see if I can find classical analogs of quantum scars and quasiparticle

states.

Similarly, while this dissertation mainly used spins 1/2, there is nothing restricting from other (finite sized) Hilbert spaces. Looking at larger spins and Hilbert spaces might have some interesting results, as well as other more funny systems such as restricted subspace system such as spin glasses, where the Hilbert space does not necessarily factorize, or in subspaces such as fixed particle number.

Longrange, higher-dimensional, and physical models

This dissertation was mainly concerned with *methods*: finding the limitations and restrictions of the cTWA. Because of this, most models were simple toy models, mainly the 1d disordered XXZ model and 1d mixed-field Ising model. However, it would be very interesting to connect to experiment and more physical systems, such as trapped ions and molecular dynamics. Especially would be higher-dimensional and/or longrange systems, which should have more reasonable classical limits.

Quantum computing with phase space

Quantum computing is a hot topic and yet hardly mentioned in this dissertation. With these phase space methods, one can capture both quantum and classical behavior within one framework. One might ask if a similar idea can be applied to quantum computing: the "hard nugget" of quantum behavior may be handled on a small quantum computer, while the "simpler" classical "thermal" behavior may be handled on a classical computer, with some hybrid quantum-classical algorithm which separates these two tasks. While it is not clear what separates the quantum and classical parts of an algorithm, phase space methods may motivate how to make this distinction. I will be researching these ideas along with Peter Love at Tufts university during a postdoc, and welcome others to join me.

Quantum scars and athermal systems

One interesting thing to come out of the recent paper (Wurtz and Polkovnikov, 2020) on approximate eigenstates and conservation laws was the discovery of a nonthermal state, signified by having low entanglement entropy and nonthermal local expectation values, even while existing at a finite energy density. It would be very interesting to see if nonthermal states (and by extension, scar states, which are small closed subspaces of states) can be robustly found using approximate adiabatic gauge potentials.

Geometry and the adiabatic gauge potential

One interesting direction is of finding optimal paths for adiabatic evolution in a multi-parameter parameter space. For example, in the mixed-field Ising model, one may change both the X and Z fields in different ways to move, say, the ground state from one region to another. There may exist better paths then others which avoid phase transitions and other gap closing points and thus admit an efficient evolution. There is currently work on this with (Sugiura et. al, unpublished) and Artem Rakcheev.

Approximate quasiparticle states

One of the interesting results of chapter 5 and paper (Wurtz and Polkovnikov, 2020) was finding approximate quasiparticle states with a long lifetime. It would be very interesting to further refine these quasiparticle states using methods like DMRG and other wavefunction ansatz, as well as compute more accurate quasiparticle lifetimes. Along with this, it would be very interesting to compute things like quasiparticle scattering and interactions with thermal backgrounds.

Adiabatic dressing and connections to integrability breaking

A final and very interesting future direction is that of integrability breaking and thermalization. Integrable systems are a particular class of Hamiltonians which normally have certain fine-tuned parameters or excluded terms, and support an extensive number of conserved quantities. This means that, unlike quantum thermal systems, an initial quench will not relax to equilibrium and will remain athermal for all time (in that the system "remembers" its initial conditions). The adiabatic gauge potential might be able to be used as a tool to probe the response of adding different integrability-breaking terms to the Hamiltonian: certain terms may admit a good adiabatic dressing of states and thus have certain states still have long-time athermality, while other terms may not admit such dressing and quickly break any integrable behavior a system may have.

6.3 Concluding remarks

Finally, I would like to make a few concluding remarks. The general goal and ideas of this thesis work have been to separate quantum behavior from classical behavior in generic quantum systems. There may, and should, exist reasonable large-scale classical behaviors even for extremely quantum systems, even though a'priori it is not necessarily clear what that may look like. Similarly, there may always be some essential quantum aspects which may still effect large-scale behavior, such as quasiparticle effects or many body localization.

In this regard, I have done this and future research with understanding in mind. To understand and harness the power of quantum mechanics, either in quantum computers or exotic materials. To understand and push the limitations of physical quantum mechanics, through mechanisms like thermalization, entanglement, and decoherence. To understand the boundaries of quantum mechanics, and poten-

tially get a glimpse of the physics which lies beyond our current understanding. But in all, I am participating in the great journey which is science.

Appendix A

Appendix

A.1 U(1) broken XY model is quantum chaotic

It is simple to check that we are not missing out on additional symmetries of the $U(1)$-symmetry-broken XY model and that it is quantum chaotic, in that the spectral statistics follow a Wigner-Dyson distribution in the middle of the spectrum (Guhr et al., 1998; D'Alessio et al., 2016). The only two symmetries are parity and translation, and so one can compute the statistics within a given symmetry sector. In Fig. A·1 is the level spacing statistics presented for the zero-momentum, parity +1 sector of Hamiltonian Eq. (5.4), with $J_{xx} = J_{yy} = 1$, $h = 3$, $\lambda = 1.25$, and 20 sites. These statistics and the correspondence to the Wigner-Dyson distribution indicate that this model is in fact quantum chaotic.

A.2 Solution of the diffusion equation on a discrete lattice

In this appendix we detail derivation of Eq. 3.7, as well as of the expressions representing the black dashed lines of figures 3·4, 3·5, and 3·7. The discrete classical diffusion equation reads:

$$\partial_t \rho_i = -D(2\rho_l - \rho_{l-1} - \rho_{l+1}). \tag{A.1}$$

Here ρ represents a conserved charge, which is given by the Z-magnetization in our case. This equation can be easily solved in the momentum space using the

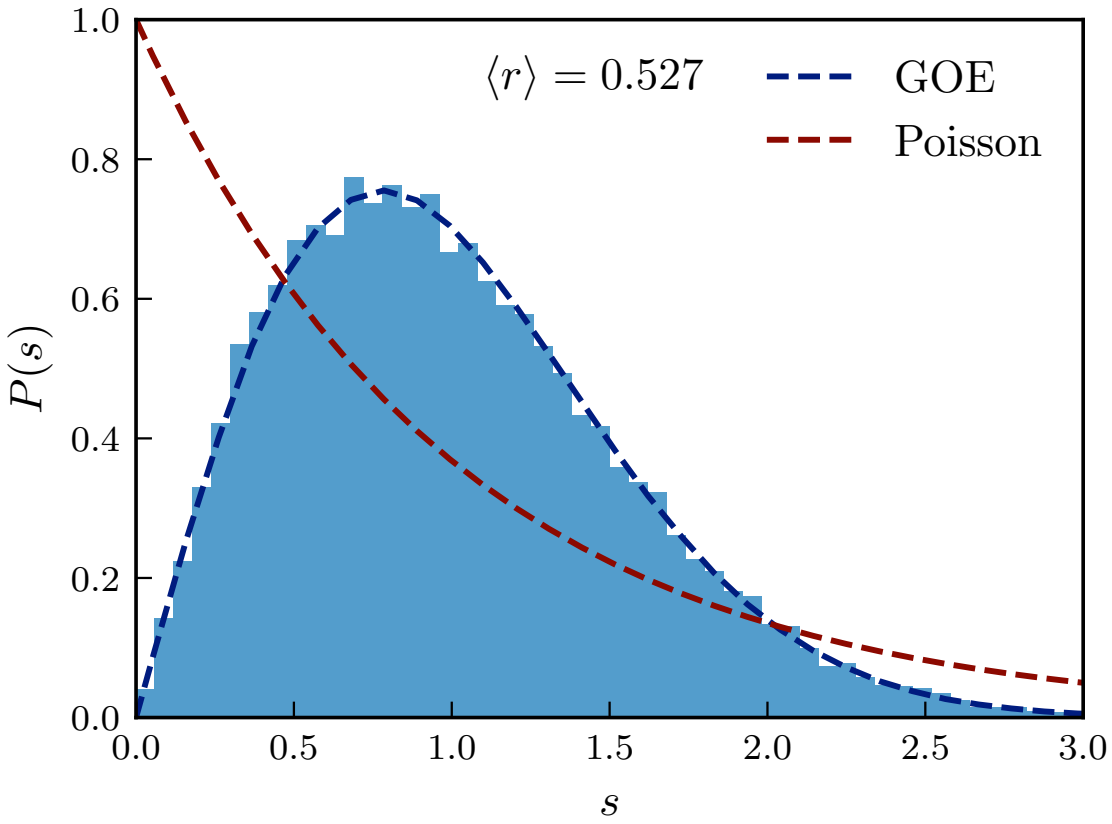

Figure A·1: Level spacing statistics $P(s)$ with $s_n = E_{n+1} - E_n$ for the zero-momentum sector of a 20-spin XY model in a longitudinal field. See section 5.4 for details. The blue dashed line represents the Wigner-Dyson statistics characteristic of chaotic models, whereas the red line represents the Poisson distribution characterizing integrability. The average value of $r_n = \min(s_n, s_{n+1})/\max(s_n, s_{n+1})$ also returns a value close to the expected Wigner-Dyson value of $\langle r \rangle = 0.536$ (Guhr et al., 1998).

Fourier transform of ρ:

$$\eta_k = \sum_l e^{ikl}\rho_l, \quad k = 0, 2\pi/N, \ldots 2\pi(N-1)/N.$$

Then the diffusion equation for each Fourier component η_k reduces to a simple first order differential equations, which is easy to solve

$$\partial_t \eta_k = -2D\rho_k(1-\cos(k)) \quad \Rightarrow \quad \eta_k(t) = \eta_k(0)e^{-2Dt(1-\cos(k))}. \tag{A.2}$$

Using this solution one can easily find the conformal diffusion width shown in the main text (Eq. 3.6):

$$\begin{aligned} R^2(t) = \sum_l \frac{N^2}{\pi^2}\sin^2\left(\frac{\pi j}{N}\right)\rho_j(t) \\ = \sum_{kl} \frac{N^2}{\pi^2}\sin^2\left(\frac{\pi l}{N}\right)e^{-ikl}\eta_k(t) \\ = \frac{N}{2\pi^2}\left(\eta_0 - \frac{1}{2}\eta_{2\pi/N} - \frac{1}{2}\eta_{-2\pi/N}\right). \end{aligned}$$

Inserting the explicit solution for form of $\eta_k(t)$ with the initial condition $\eta_k(0) = 1$ and expanding $\cos(2\pi/N) \approx 1 - (2\pi/N)^2/2$ at large N we derive Eq. 3.7 from the main text. Similarly, one can find the diffusive structure factor $S(k,\omega)$

$$S(k,\omega) = \int_{-\infty}^{\infty} dt e^{i\omega t}\eta_k(t) = \frac{4D(1-\cos(k))}{\omega^2 + 4D^2(1-\cos(k))^2}. \tag{A.3}$$

Journal Abbreviations

Adv. Phys.	Advances in Physics
Ann. Phys.	Annals of Physics
Annu. Rev. Condens. Matter	Annual Review of Condensed Matter Physics,
Phys. Commun. Math. Phys.	Communications in Mathematical Physics
Int J Mod Phys A	International Journal of Modern Physics A
J. High Energy Phys.	Journal of High Energy Physics
J. Phys. C	Journal of Physics C: Solid State Physics
J. Stat. Mech. Theory Exp.	Journal of Statistical Mechanics: Theory and Experiment
Nat. Phys.	Nature Physics
New J. Phys.	New Journal of Physics
Phys. Rep.	Physics Reports
Phys. Rev.	Physical Review
Phys. Rev. A	Physical Review A
Phys. Rev. B	Physical Review B
Phys. Rev. D	Physical Review D
Phys. Rev. E	Physical Review E
Phys. Rev. Lett	Physical Review Letters
Phys. Rev. X	Physical Review X
Proc. Natl. Acad. Sci. U.S.A.	Proceedings of the National Academy of Sciences
Rep. Prog. Phys.	Reports on Progress in Physics
Rev. Mod. Phys.	Reviews of Modern Phyics
Zh. Eksp. Teor. Fiz.	Journal of Experimental and Theoretical Physics

References

Abanin, D. A., Altman, E., Bloch, I., and Serbyn, M. (2019). Colloquium: Many-body localization, thermalization, and entanglement. *Rev. Mod. Phys.*, 91:021001.

Abanin, D. A., De Roeck, W., Ho, W. W., and Huveneers, F. (2017). Effective hamiltonians, prethermalization, and slow energy absorption in periodically driven many-body systems. *Phys. Rev. B*, 95:014112.

Abanin, D. A., De Roeck, W., and Huveneers, F. m. c. (2015). Exponentially slow heating in periodically driven many-body systems. *Phys. Rev. Lett.*, 115:256803.

Acevedo, O. L., Safavi-Naini, A., Schachenmayer, J., Wall, M. L., Nandkishore, R., and Rey, A. M. (2017). Exploring many-body localization and thermalization using semiclassical methods. *Phys. Rev. A*, 96:033604.

Agarwal, K., Gopalakrishnan, S., Knap, M., Müller, M., and Demler, E. (2015). Anomalous diffusion and griffiths effects near the many-body localization transition. *Phys. Rev. Lett.*, 114:160401.

Anderson, P. W. (1967). Infrared catastrophe in fermi gases with local scattering potentials. *Phys. Rev. Lett.*, 18:1049–1051.

Bachmann, S., De Roeck, W., and Fraas, M. (2017). Adiabatic theorem for quantum spin systems. *Phys. Rev. Lett.*, 119:060201.

Bar Lev, Y., Cohen, G., and Reichman, D. R. (2015). Absence of diffusion in an interacting system of spinless fermions on a one-dimensional disordered lattice. *Phys. Rev. Lett.*, 114:100601.

Bernien, H., Schwartz, S., Keesling, A., Levine, H., Omran, A., Pichler, H., Choi, S., Zibrov, A. S., Endres, M., Greiner, M., Vuletic, V., and Lukin, M. D. (2017). Probing many-body dynamics on a 51-atom quantum simulator. *Nature*, 551(7682):579–584.

Bertini, B., Essler, F. H. L., Groha, S., and Robinson, N. J. (2016). Thermalization and light cones in a model with weak integrability breaking. *Phys. Rev. B*, 94:245117.

Blakie, P., Bradley, A., Davis, M., Ballagh, R., and Gardiner, C. (2008). Dynamics and statistical mechanics of ultra-cold bose gases using c-field techniques. *Adv. Phys.*, 57(5):363–455.

Blanes, S., Casas, F., Oteo, J., and Ros, J. (2009). The magnus expansion and some of its applications. *Phys. Rep.*, 470(5):151 – 238.

Bloch, I., Dalibard, J., and Nascimbène, S. (2012). Quantum simulations with ultracold quantum gases. *Nat. Phys.*, 8(4):267–276.

Blundell, S. (2001). *Magnetism in Condensed Matter*. Oxford University Press.

Bonfim, O. F. d. A., Boechat, B., and Florencio, J. (2019). Ground-state properties of the one-dimensional transverse ising model in a longitudinal magnetic field. *Phys. Rev. E*, 99:012122.

Bordia, P., Lüschen, H. P., Hodgman, S. S., Schreiber, M., Bloch, I., and Schneider, U. (2016). Coupling identical one-dimensional many-body localized sys-

tems. *Phys. Rev. Lett.*, 116:140401.

Borgonovi, F., Izrailev, F., Santos, L., and Zelevinsky, V. (2016). Quantum chaos and thermalization in isolated systems of interacting particles. *Phys. Rep.*, 626:1 – 58.

Brandino, G. P., Caux, J.-S., and Konik, R. M. (2015). Glimmers of a quantum kam theorem: Insights from quantum quenches in one-dimensional bose gases. *Phys. Rev. X*, 5:041043.

Bravyi, S., DiVincenzo, D. P., and Loss, D. (2011). Schrieffer-Wolff transformation for quantum many-body systems. *Ann. Phys.*, 326(10):2793–2826.

Bukov, M., Kolodrubetz, M., and Polkovnikov, A. (2016). Schrieffer-Wolff Transformation for Periodically Driven Systems: Strongly Correlated Systems with Artificial Gauge Fields. *Phys. Rev. Lett.*, 116(12):1–6.

Bukov, M., Sels, D., and Polkovnikov, A. (2019). Geometric speed limit of accessible many-body state preparation. *Phys. Rev. X*, 9:011034.

Calabrese, P., Essler, F. H. L., and Fagotti, M. (2012a). Quantum quench in the transverse field ising chain: I. time evolution of order parameter correlators. *J. Stat. Mech. Theory Exp.*, 2012(07):P07016.

Calabrese, P., Essler, F. H. L., and Fagotti, M. (2012b). Quantum quenches in the transverse field ising chain: II. stationary state properties. *J. Stat. Mech. Theory Exp.*, 2012(07):P07022.

Chen, X., Gu, Z.-C., and Wen, X.-G. (2010). Local unitary transformation, long-range quantum entanglement, wave function renormalization, and topological order. *Phys. Rev. B*, 82:155138.

Choi, S., Turner, C. J., Pichler, H., Ho, W. W., Michailidis, A. A., Papic, Z., Serbyn, M., Lukin, M. D., and Abanin, D. A. (2019). Emergent su(2) dynamics and perfect quantum many-body scars. *Phys. Rev. Lett.*, 122:220603.

Claeys, P. W., Pandey, M., Sels, D., and Polkovnikov, A. (2019). Floquet-engineering counterdiabatic protocols in quantum many-body systems. *Phys. Rev. Lett.*, 123:090602.

Cohen-Tannoudji, C., Dupont-Roc, J., and Grynberg, G. (1998). *Atom-Photon Interactions*. Wiley.

D'Alessio, L., Kafri, Y., Polkovnikov, A., and Rigol, M. (2016). From quantum chaos and eigenstate thermalization to statistical mechanics and thermodynamics. *Adv. Phys.*, 65(3):239–362.

Das, A., Chakrabarty, S., Dhar, A., Kundu, A., Huse, D. A., Moessner, R., Ray, S. S., and Bhattacharjee, S. (2018). Light-cone spreading of perturbations and the butterfly effect in a classical spin chain. *Phys. Rev. Lett.*, 121:024101.

Davidson, S. M. and Polkovnikov, A. (2015). Su (3) semiclassical representation of quantum dynamics of interacting spins. *Phys. Rev. Lett*, 114.

Davidson, S. M., Sels, D., and Polkovnikov, A. (2017). Semiclassical approach to dynamics of interacting fermions. *Ann. Phys.*, 384(Supplement C):128 – 141.

De Nardis, J., Bernard, D., and Doyon, B. (2018). Hydrodynamic diffusion in integrable systems. *Phys. Rev. Lett.*, 121:160603.

De Nardis, J., Bernard, D., and Doyon, B. (2019). Diffusion in generalized hydrodynamics and quasiparticle scattering. *SciPost Physics*, 6(4).

Edwards, J. T. and Thouless, D. J. (1972). Numerical studies of localization in disordered systems. *J. Phys. C*, 5(8):807.

Faddeev, L. D. (1996). How algebraic bethe ansatz works for integrable model.

Gaudin, M. (2014). *The Bethe Wavefunction*. Cambridge University Press.

Gibbons, K. S., Hoffman, M. J., and Wootters, W. K. (2004). Discrete phase space based on finite fields. *Phys. Rev. A*, 70:062101.

Gogolin, C. and Eisert, J. (2016). Equilibration, thermalisation, and the emergence of statistical mechanics in closed quantum systems. *Rep. Prog. Phys.*, 79(5):056001.

Goldstein, S., Lebowitz, J. L., Tumulka, R., and Zanghì, N. (2006). Canonical typicality. *Phys. Rev. Lett.*, 96:050403.

Gopalakrishnan, S., Müller, M., Khemani, V., Knap, M., Demler, E., and Huse, D. A. (2015). Low-frequency conductivity in many-body localized systems. *Phys. Rev. B*, 92:104202.

Gopalakrishnan, S. and Vasseur, R. (2019). Kinetic theory of spin diffusion and superdiffusion in XXZ spin chains. *Phys. Rev. Lett.*, 122:127202.

Gopalakrishnan, S., Vasseur, R., and Ware, B. (2019). Anomalous relaxation and the high-temperature structure factor of XXZ spin chains. *Proc. Natl. Acad. Sci. U.S.A.*, 116(33):16250–16255.

Gottesman, D. (1998). The heisenberg representation of quantum computers.

Griffiths, D. (2005). *Introduction to Quantum Mechanics*. Pearson, 2 edition.

Grusdt, F., Kánasz-Nagy, M., Bohrdt, A., Chiu, C. S., Ji, G., Greiner, M., Greif, D., and Demler, E. (2018). Parton theory of magnetic polarons: Mesonic resonances and signatures in dynamics. *Phys. Rev. X*, 8:011046.

Guhr, T., Muller−Groeling, A., and Weidenmuller, H. A. (1998). Random-matrix theories in quantum physics: common concepts. *Phys. Rep.*, 299(4):189 – 425.

Haegeman, J., Cirac, J. I., Osborne, T. J., Pižorn, I., Verschelde, H., and Verstraete, F. (2011). Time-dependent variational principle for quantum lattices. *Phys. Rev. Lett.*, 107:070601.

Haldar, A., Moessner, R., and Das, A. (2018). Onset of floquet thermalization. *Phys. Rev. B*, 97:245122.

Haldar, A., Sen, D., Moessner, R., and Das, A. (2019). Scars in strongly driven floquet matter: resonance vs emergent conservation laws.

Hastings, M. B. (2007). An area law for one-dimensional quantum systems. *J. Stat. Mech. Theory Exp.*, 2007(08):P08024–P08024.

Hastings, M. B. and Wen, X.-G. (2005). Quasiadiabatic continuation of quantum states: The stability of topological ground-state degeneracy and emergent gauge invariance. *Phys. Rev. B*, 72:045141.

Hillery, M., O'Connell, R. F., Scully, M. O., and Wigner, E. P. (1984). Distribution functions in physics: Fundamentals. *Phys. Rep.*, 106(3):121–167.

Ho, W. W., Protopopov, I., and Abanin, D. A. (2018). Bounds on energy absorption and prethermalization in quantum systems with long-range interactions. *Phys. Rev. Lett.*, 120:200601.

Hubbard, J. (1963). Electron Correlations in Narrow Energy Bands. *Royal Society*, 276(1365):238–257.

Imbrie, J. Z. (2016). Diagonalization and many-body localization for a disordered quantum spin chain. *Phys. Rev. Lett.*, 117:027201.

Jacquod, P. and Petitjean, C. (2009). Decoherence, entanglement and irreversibility in quantum dynamical systems with few degrees of freedom. *Adv. Phys.*, 58(2):67–196.

James, A. J. A., Konik, R. M., Lecheminant, P., Robinson, N. J., and Tsvelik, A. M. (2017). Non-perturbative methodologies for low-dimensional strongly-correlated systems: From non-abelian bosonization to truncated spectrum methods. *Rep. Prog. Phys.*, 81:046002.

James, A. J. A., Konik, R. M., and Robinson, N. J. (2019). Nonthermal states arising from confinement in one and two dimensions. *Phys. Rev. Lett.*, 122:130603.

Karbach, M. and Muller, G. (1998). Introduction to the bethe ansatz i.

Karrasch, C., Moore, J. E., and Heidrich-Meisner, F. (2014). Real-time and real-space spin and energy dynamics in one-dimensional spin-$\frac{1}{2}$ systems induced by local quantum quenches at finite temperatures. *Phys. Rev. B*, 89:075139.

Kaufman, A. M., Tai, M. E., Lukin, A., Rispoli, M., Schittko, R., Preiss, P. M., and Greiner, M. (2016). Quantum thermalization through entanglement in an isolated many-body system. *Science*, 353(6301):794–800.

Kehrein, S. (2006). *The Flow Equation Approach to Many-Particle Systems*. Springer.

Khemani, V., Huse, D. A., and Nahum, A. (2018). Velocity-dependent lyapunov exponents in many-body quantum, semiclassical, and classical chaos. *Phys. Rev. B*, 98:144304.

Kim, H., Ikeda, T. N., and Huse, D. A. (2014). Testing whether all eigenstates obey the eigenstate thermalization hypothesis. *Phys. Rev. E*, 90:052105.

Koepsell, J., Vijayan, J., Sompet, P., Grusdt, F., Hilker, T. A., Demler, E., Salomon, G., Bloch, I., and Gross, C. (2019). Imaging magnetic polarons in the doped fermi-hubbard model. *Nature*, 572(7769):358–362.

Kolodrubetz, M., Sels, D., Mehta, P., and Polkovnikov, A. (2017a). Geometry and non-adiabatic response in quantum and classical systems. *Phys. Rep.*, 697:1–87.

Kolodrubetz, M., Sels, D., Mehta, P., and Polkovnikov, A. (2017b). Geometry and non-adiabatic response in quantum and classical systems. *Phys. Rep.*, 697:1 – 87.

Kormos, M., Collura, M., Takács, G., and Calabrese, P. (2017). Real-time confinement following a quantum quench to a non-integrable model. *Nat. Phys.*, 13(3):246–249.

Krause, U., Pellegrin, T., Brouwer, P. W., Abanin, D. A., and Filippone, M. (2019). Nucleation of ergodicity by a single doublon in supercooled insulators.

Kulshreshtha, A. K., Pal, A., Wahl, T. B., and Simon, S. H. (2018). Behavior of l-bits near the many-body localization transition. *Phys. Rev. B*, 98:184201.

Kuwahara, T., Mori, T., and Saito, K. (2016). Floquet–magnus theory and generic transient dynamics in periodically driven many-body quantum systems.

Ann. Phys., 367:96 – 124.

Landau, L. and Lifshitz, E. (2013). *Statistical Physics*. Number v. 5. Elsevier Science.

Langen, T., Gasenzer, T., and Schmiedmayer, J. (2016). Prethermalization and universal dynamics in near-integrable quantum systems. *J. Stat. Mech. Theory Exp.*, 2016(6):064009.

Larkin and Ovchinnikov (1969). Quasiclassical method in the theory of superconductivity. *Zh. Eksp. Teor. Fiz.*, 28(6):2262–2272.

Leviatan, E., Pollmann, F., Bardarson, J. H., Huse, D. A., and Altman, E. (2017). Quantum thermalization dynamics with matrix-product states.

Lin, C.-J. and Motrunich, O. I. (2019). Exact quantum many-body scar states in the rydberg-blockaded atom chain. *Phys. Rev. Lett.*, 122:173401.

Ljubotina, M., Znidaric, M., and Prosen, T. (2017). Spin diffusion from an inhomogeneous quench in an integrable system. *Nature Communications*, 8(1):16117.

Luitz, D. J. and Bar Lev, Y. (2016). Anomalous thermalization in ergodic systems. *Phys. Rev. Lett.*, 117:170404.

Luitz, D. J., Laflorencie, N., and Alet, F. (2015). Many-body localization edge in the random-field Heisenberg chain. *Phys. Rev. B*, 91(8):1–5.

Luitz, D. J. and Lev, Y. B. (2017). The ergodic side of the many-body localization transition. *Ann. Phys.*, 529(7):1600350.

Luitz, D. J., Moessner, R., Sondhi, S. L., and Khemani, V. (2019). Prethermalization without temperature.

Lux, J., Müller, J., Mitra, A., and Rosch, A. (2014). Hydrodynamic long-time tails after a quantum quench. *Phys. Rev. A*, 89:053608.

Mari, A. and Eisert, J. (2012). Positive wigner functions render classical simulation of quantum computation efficient. *Phys. Rev. Lett.*, 109:230503.

Michailidis, A. A., Žnidarič, M., Medvedyeva, M., Abanin, D. A., Prosen, T. c. v., and Papić, Z. (2018). Slow dynamics in translation-invariant quantum lattice models. *Phys. Rev. B*, 97:104307.

Moeckel, M. and Kehrein, S. (2008). Interaction quench in the hubbard model. *Phys. Rev. Lett.*, 100:175702.

Mukerjee, S., Oganesyan, V., and Huse, D. (2006). Statistical theory of transport by strongly interacting lattice fermions. *Phys. Rev. B*, 73:035113.

Nachtergaele, B. and Sims, R. (2006). Lieb-robinson bounds and the exponential clustering theorem. *Commun. Math. Phys.*, 265(1):119–130.

Nahum, A., Vijay, S., and Haah, J. (2018). Operator spreading in random unitary circuits. *Phys. Rev. X*, 8:021014.

Nandkishore, R. and Huse, D. A. (2015). Many-body localization and thermalization in quantum statistical mechanics. *Annu. Rev. Condens. Matter Phys.*, 6(1):15–38.

Neill, C., Roushan, P., Fang, M., Chen, Y., Kolodrubetz, M., Chen, Z., Megrant, A., Barends, R., Campbell, B., Chiaro, B., Dunsworth, A., Jeffrey, E., Kelly, J., Mutus, J., O'Malley, P. J., Quintana, C., Sank, D., Vainsencher, A., Wenner, J., White, T. C., Polkovnikov, A., and Martinis, J. M. (2016). Ergodic dynamics

and thermalization in an isolated quantum system. *Nat. Phys.*, 12(11):1037–1041.

Nielsen, M. A. and Chuang, I. L. (2011). *Quantum Computation and Quantum Information: 10th Anniversary Edition*. Cambridge University Press, USA, 10th edition.

Oganesyan, V., Pal, A., and Huse, D. A. (2009). Energy transport in disordered classical spin chains. *Phys. Rev. B*, 80:115104.

Onsager, L. (1931). Reciprocal relations in irreversible processes. i. *Phys. Rev.*, 37:405–426.

Ovchinnikov, A. A., Dmitriev, D. V., Krivnov, V. Y., and Cheranovskii, V. O. (2003). Antiferromagnetic ising chain in a mixed transverse and longitudinal magnetic field. *Phys. Rev. B*, 68:214406.

Pirvu, B., Murg, V., Cirac, J. I., and Verstraete, F. (2010). Matrix product operator representations. *New J. Phys.*, 12(2):025012.

Polkovnikov, A. (2010). Phase space representation of quantum dynamics. *Ann. Phys.*, 325(8):1790–1852.

Polkovnikov, A., Sengupta, K., Silva, A., and Vengalattore, M. (2011). Colloquium: Nonequilibrium dynamics of closed interacting quantum systems. *Rev. Mod. Phys.*, 83:863–883.

Prosen, T. (2011a). Exact nonequilibrium steady state of a strongly driven open XXZ chain. *Phys. Rev. Lett.*, 107:137201.

Prosen, T. (2011b). Open XXZ spin chain: Nonequilibrium steady state and a strict bound on ballistic transport. *Phys. Rev. Lett.*, 106:217206.

Richter, J., Jin, F., De Raedt, H., Michielsen, K., Gemmer, J., and Steinigeweg, R. (2018). Real-time dynamics of typical and untypical states in nonintegrable systems. *Phys. Rev. B*, 97:174430.

Rigol, M., Dunjko, V., and Olshanii, M. (2008). Thermalization and its mechanism for generic isolated quantum systems. *Nature*, 452(7189):854–858.

Robinson, N. J., James, A. J. A., and Konik, R. M. (2019). Signatures of rare states and thermalization in a theory with confinement. *Phys. Rev. B*, 99:195108.

Sachdev, S. (2011). *Quantum Phase Transitions*. Cambridge University Press, 2 edition.

Sakurai, J. J. and Napolitano, J. (2017). *Modern Quantum Mechanics*. Cambridge University Press, 2 edition.

Santos, L. F. and Rigol, M. (2010). Onset of quantum chaos in one-dimensional bosonic and fermionic systems and its relation to thermalization. *Phys. Rev. E*, 81:036206.

Schmitt, M., Sels, D., Kehrein, S., and Polkovnikov, A. (2019). Semiclassical echo dynamics in the Sachdev-Ye-Kitaev model. *Phys. Rev. B*, 99:134301.

Schrieffer, J. R. and Wolff, P. A. (1966). Relation between the Anderson and Kondo Hamiltonians. *Phys. Rev.*, 149(2).

Sekino, Y. and Susskind, L. (2008). Fast scramblers. *J. High Energy Phys.*, 2008(10):065–065.

Sels, D. and Polkovnikov, A. (2017). Minimizing irreversible losses in quantum systems by local counterdiabatic driving. *Proc. Natl. Acad. Sci. U.S.A.*, 114(20):E3909–E3916.

Serbyn, M., Papic, Z., and Abanin, D. A. (2013). Local conservation laws and the structure of the many-body localized states. *Phys. Rev. Lett.*, 111:127201.

Serbyn, M., Papic, Z., and Abanin, D. A. (2014). Quantum quenches in the many-body localized phase. *Phys. Rev. B*, 90:174302.

Shankar, R. (1994). Renormalization-group approach to interacting fermions. *Rev. Mod. Phys.*, 66:129–192.

Shastry, B. S. (1986a). Exact Integrability of the One-Dimensional Hubbard Model. *Phys. Rev. Lett.*, 56(23):2453–2455.

Shastry, B. S. (1986b). Infinite conservation laws in the one-dimensional hubbard model. *Phys. Rev. Lett.*, 56(15):1529–1531.

Shraiman, B. I. and Siggia, E. D. (1988). Mobile vacancies in a quantum heisenberg antiferromagnet. *Phys. Rev. Lett.*, 61:467–470.

Simon, J., Bakr, W. S., Ma, R., Tai, M. E., Preiss, P. M., and Greiner, M. (2011). Quantum simulation of antiferromagnetic spin chains in an optical lattice. *Nature*, 472(7343):307–312.

Srednicki, M. (1994). Chaos and quantum thermalization. *Phys. Rev. E*, 50:888–901.

Steinigeweg, R. and Brenig, W. (2011). Spin transport in the XXZ chain at finite temperature and momentum. *Phys. Rev. Lett.*, 107:250602.

Steinigeweg, R., Heidrich-Meisner, F., Gemmer, J., Michielsen, K., and De Raedt, H. (2014). Scaling of diffusion constants in the spin-$\frac{1}{2}$ xx ladder. *Phys. Rev. B*, 90:094417.

Suntajs, J., Bonča, J., Prosen, T., and Vidmar, L. (2019). Quantum chaos challenges many-body localization.

Szpigel, S. and Perry, R. J. (2000). The similarity renormalization group.

Tang, Y., Kao, W., Li, K.-Y., Seo, S., Mallayya, K., Rigol, M., Gopalakrishnan, S., and Lev, B. L. (2018). Thermalization near integrability in a dipolar quantum newton's cradle. *Phys. Rev. X*, 8:021030.

Turner, C. J., Michailidis, A. A., Abanin, D. A., Serbyn, M., and Papic, Z. (2018a). Quantum scarred eigenstates in a rydberg atom chain: Entanglement, breakdown of thermalization, and stability to perturbations. *Phys. Rev. B*, 98:155134.

Turner, C. J., Michailidis, A. A., Abanin, D. A., Serbyn, M., and Papic, Z. (2018b). Weak ergodicity breaking from quantum many-body scars. *Nat. Phys.*, 14(7):745–749.

Viswanath, V. and Müller, G. (2008). *The Recursion Method*. Springer US.

Vogl, M., Laurell, P., Barr, A. D., and Fiete, G. A. (2019). Flow equation approach to periodically driven quantum systems. *Phys. Rev. X*, 9:021037.

Wegner, F. (1990). Flow-equation for Hamiltonians. *Ann. Phys.*, 506(2):77–91.

Wootters, W. K. (1987). A wigner-function formulation of finite-state quantum mechanics. *Ann. Phys.*, 176(1):1–21.

Wurtz, J., Claeys, P. W., and Polkovnikov, A. (2020). Variational schrieffer-wolff transformations for quantum many-body dynamics. *Phys. Rev. B*, 101:014302.

Wurtz, J. and Polkovnikov, A. (2018). Quantum hydrodynamics in spin chains with phase space methods.

Wurtz, J. and Polkovnikov, A. (2020). Emergent conservation laws and nonthermal states in the mixed-field ising model.

Wurtz, J., Polkovnikov, A., and Sels, D. (2018). Cluster truncated Wigner approximation in strongly interacting systems. *Ann. Phys.*, 395:341 – 365.

Zamolodchikov, A. B. (1989). INTEGRALS OF MOTION AND s-MATRIX OF THE (SCALED) t = tc ISING MODEL WITH MAGNETIC FIELD. *Int J Mod Phys A*, 04(16):4235–4248.

CURRICULUM VITAE